DISSERTATION

A STUDY OF MAGNETOSTRUCTURAL PARAMETERS RELATED TO

SPIN CROSSOVER AND SINGLE-MOLECULE MAGNETISM

Submitted by

Stephanie R. Fiedler

Department of Chemistry

In partial fulfillment of the requirements

For the Degree of Doctor of Philosophy

Colorado State University

Fort Collins, Colorado

Fall 2013

Doctoral Committee:

Advisor: Matthew P. Shores

Alan J. Kennan
Oren P. Anderson
Debbie C. Crans
Carl E. Patton

ABSTRACT

A STUDY OF MAGNETOSTRUCTURAL PARAMETERS RELATED TO

SPIN CROSSOVER AND SINGLE-MOLECULE MAGNETISM

Herein are described studies of transition metal complexes that were designed via specific synthetic modifications to effect changes in the structural, magnetic and anion-binding properties. In Chapter 1, a brief introduction is presented to introduce the broader goal of our research: controlling spin on the synthetic level and how that affects the structural, magnetic and anion-binding properties. The introduction provides background regarding spin crossover and single molecule magnetism as well as some previous research to put our projects in context relative to endeavors by other researchers.

In Chapter 2, heteroleptic complexes of the form $[Fe(H_2bip)_2(pizR)]Br_2$ and $[Fe(H_2bip)_2(pizR)](BPh_4)_2$ are described, which have the opportunity to chelate an anion via hydrogen bonding to the H_2bip ligand. The third ligand, pizR, is varied between two ligands that we predict will have similar ligand field strengths: pizH and pizMe. Because pizH has an additional hydrogen-bonding site, while pizMe does not, we selected these ligands in order to understand the effect of hydrogen bonding on the anion-binding/spin-state switching event *independent* from ligand field strength. From these studies, the pizH–anion hydrogen bond is observed in crystallographic studies, but does not affect the anion-binding or spin-state switching properties in solution.

In Chapter 3, we further investigate the geometry of the pizR ligand in Fe(II) complexes. What began as attempts to study hydrogen bonding in solution revealed unexpected structural distortions of the ligand that are correlated to the spin state of the complexes. The R-substituted

nitrogen atom on the imidazoline moiety of the pizR ligand switches between a planar geometry, which is observed for high-spin species, and a pyramidalized geometry, which is observed for low-spin species. We reason that this occurs as a result of the weak-field, non-pizR ligands that influence the ligand field in the high-spin species.

Chapters 4 and 5 delve deeper into understanding the relationship between structural parameters and magnetic properties in complexes with non-covalent interactions. In Chapter 4, a series of complexes with metallophilic Pt–Pt interactions show antiferromagnetic magnetic coupling of non-bonded transition metals through a Pt–Pt bond. By comparing complexes *with* Pt–Pt interactions to those *without* Pt–Pt interactions, we are able to determine that the Pt–Pt bond is a unique superexchange pathway for the transition metal coupling. Off-set complexes, exhibiting two Pt–S interactions instead of one Pt–Pt interaction, do not show evidence of magnetic coupling between transition metals. Furthermore, by comparing magnetic properties of complexes where the apical ligand varies, we determine that the presence or absence of intermolecular interactions is largely independent from the strength of coupling through the Pt–Pt bond.

In Chapter 5, an asymmetric trinuclear manganese complex with unique magnetic exchange properties and two high-spin square-planar complexes of iron and cobalt, are investigated. The trinuclear manganese complex consists of a central octahedral Mn(II) ion that is coupled antiferromagnetically to another octahedral Mn(II) ion and ferromagnetically to a terminal tetrahedral Mn(II) ion. The different coupling is rationalized as a result of the change in geometry, which affects the orbital overlap that is predicted for each pair of ions. The high-spin square-planar Fe(II) and Co(II) complexes illustrate an unusual pairing of spin-state with square-planar geometry. Moreover, the Fe(II) complex exhibits signs of easy-axis molecular anisotropy and slow-relaxation of magnetization, albeit in the presence of a magnetic field.

Lastly, in Chapter 6, we investigate a trinuclear Fe(III) complex bridged by a triethynylmesitylene ligand. The magnetic properties of the complex are compared to a previous Fe(III) complex bridged by a triethynylbenzene ligand. Steric interactions between the aromatic core of the ethynylmesitylene ligand and the auxiliary dimethylphosphinoethane ligands on Fe(III) are predicted to engender a ligand conformation to promote strong orbital overlap. Magnetic susceptibility data for the two complexes both exhibit ferromagnetic coupling between metal centers as expected. Further studies are necessary to confirm the observed behavior, but the new triethynylmesitylene complex appears to have slightly stronger coupling than the previous triethynylbenzene complex.

ACKNOWLEDGMENTS

AUTOBIOGRAPHY

Stephanie was born in Yankton, SD on July 9, 1985 and lived there with her parents Don and Mary Fiedler, and siblings Benjamin, Elizabeth and Katherine until graduating from Yankton High School in 2003. From there she attended Macalester College in St. Paul, MN with a month-long study abroad in Ecuador and a semester study abroad in Ireland. After graduation from Macalester College in 2007, she began a PhD program at Colorado State University in Fort Collins, CO. In the fall of 2013, Stephanie completed her PhD. In 2004, Stephanie began dating her future husband, Jeremy Gleich, and the two were married on September 25, 2010. On August 19, 2012, their first child, Izach Gleich was born. Stephanie enjoys traveling, seeing and doing new things in her spare time and her future plans are to share her love of chemistry through teaching at the college level.

DEDICATION

I dedicate this work to my husband, Jeremy Gleich. Without his encouragement and continued support, I certainly never would have seen this completed dissertation. I hope he truly considers it part his accomplishment as well as mine.

TABLE OF CONTENTS

LIST OF TABLES

LIST OF FIGURES

CHAPTER 1: ATTEMPTS TO CONTROL SPIN AND RELATED MAGNETIC PROPERTIES SYNTHETICALLY

1.1 Introduction

Advancements in controlling spin at the synthetic level could lead to applications in data storage, alternative options for molecular sensing, a better understanding of quantum chemistry effects, and ultimately, a development of more rational inorganic syntheses. Our primary interests for controlling spin lie in the areas of magnetic bistability and anion dependent spin state switching in solution. Compounds have been developed that exhibit magnetic bistability and hysteresis (vide infra), however, those properties have only been observed at very low temperatures (<5 K).[1] Moreover, these compounds are primarily discovered serendipitously.[2] Similar limitations exist in the realm of anion-dependent spin-state switching: several reports demonstrate this phenomenon in the solid state, but few in solution. By learning to control magnetic properties of spin and electronic communication through synthetic modifications, one could envision tuning a complex to exhibit specific magnetic properties at a particular temperature or in response to a particular event. Synthetic control at this level is essential en route to the development of practical applications.

This chapter covers a brief introduction into both magnetic bistability and anion-dependent spin-state switching. First, an introduction to spin state switching in solution is described. Examples with both solid state and solution properties are included. Secondly, the background of magnetic bistability with regards to single molecule magnets is described. Theoretical parameters that give rise to magnetic bistability as well as some literature attempts to design molecules with

magnetic bistability are presented. At the end of each section there is a brief introduction into the complexes presented later in this dissertation.

1.2 Spin-State Switching and Anion Sensing

Octahedral transition metal complexes with d^4, d^5, d^6, or d^7 electron counts have the potential for either high spin (maximum S) or low spin (minimum S) configurations (See Figure 1.1). In the appropriate ligand field, a balance between the electron pairing energy (Π) and octahedral splitting energy (Δo) allows for switching between the high spin (HS) and low spin (LS) configurations. It is well-known that changes in magnetism, bond lengths, polarizability and color that accompany spin-state changes in certain transition metal complexes can be triggered by changes in temperature, pressure and light.[3-11] Many applications of these coordination complex-based compounds have been explored: in particular, compounds that exhibit property changes based on external stimuli show potential for sensor applications.[12-13] Relaxation kinetics studies of SC complexes indicate HS-LS transition barriers of the range 2200 cm^{-1}–2900 cm^{-1} (6.3–8.3 kcal/mol),[14] which are similar to the predicted strength of common non-covalent interactions, for example hydrogen bonding (10.1–13.8 kcal/mol) and anion–π interactions (7.2–8.2 kcal/mol).[15] This prompts our interest in employing these complexes as colorimetric sensors for anions in solution via hydrogen bonds.

Spin crossover is observed in both the solid state and in solution. With respect to sensing properties, there are many examples of solid-state complexes that show properties that are dependent on co-crystallized counter ions, solvent molecules, or small gas molecules. While solution measurements, in theory, make use of sufficiently dilute samples that the molecules are isolated, in reality, counter ions and solvent still influence the properties, suggesting that solution-

based molecular sensors are possible. Unfortunately, examples of spin crossover in solution are significantly fewer in number and occur over broader temperature ranges than the solid state. In order to employ intermolecular interactions for spin-state switching sensors, a better understanding of how to control the interactions, including minimizing undesired interactions, is required. Some examples of research toward this end are summarized in the next section.
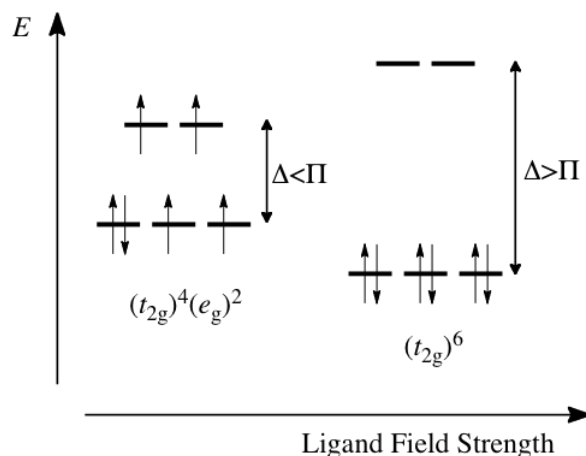
Figure 1.1. left: a high spin configuration of a d^6 ion, with $S = 2$; right: a low spin configuration of a d^6 ion, with $S = 0$.

In the solid state, the spin crossover of the bulk sample can be described in terms of completeness, crossover temperature, and cooperativity. Completeness is related to the percent of the sample that coverts from HS at high temperature to LS at low temperature (or in response to other stimuli). If the sample converts abruptly from HS to LS, it is said to have good cooperativity. The spin-transition temperature, $T\frac{1}{2}$, is the temperature at which the susceptibility corresponds to a sample that is halfway between the HS and LS values. This temperature is often dependent on the ligand field environment for each complex. In several examples, the ligand field can be anion or solvent dependent, making this an important factor when considering these complexes as sensors (*vide infra*). Lastly, cooperativity can be directly influenced by intermolecular interactions:

strong 'communication' can create a chain reaction that enables the entire sample to change spin suddenly. In some cases, however, intermolecular interactions can prevent cooperativity by trapping individual molecules in one spin state. Plots of susceptibility vs. temperature allow for visual comparisons of the completeness, the cooperativity and the crossover temperature for complexes.

1.3 Examples of Spin-State Switching Research

One early study of anion effects on spin state of an Fe^{II} complex was by Kennedy et al. on [Fe(salen)(imidazole)]Y complexes (salen = N,N'-ethylenebis(salicylaldimine), Y = BPh_4^-, ClO_4^-, BF_4^- or PF_6^-).[16] This is one of few studies that does not have co-crystallized solvent in the samples and can hope to isolate the spin-state switching features to anions alone. The variations of $\chi_M T$ vs. T for each salt are shown in Figure 1.2. Solid-state interactions were studied in the room temperature crystal structures of perchlorate (ClO_4^-), tetrafluoroborate (BF_4^-), and hexafluorophosphate (PF_6^-) salts. The salen ligand geometry varies depending on anion: in the PF_6^- salt, the ligand is mostly planar, while the ClO_4^- and BF_4^- salts show "envelope" orientations. The authors attribute the lack of spin transition for the PF_6^- salt to the planar ligand preventing structural changes that are concomitant with the spin transition. In addition, PF_6^- and BPh_4^- anions are larger than ClO_4^- or BF_4^-, which may lead to three-dimensional ordering that favors the planar salen ligand and subsequently induces the lack of spin transition. Meanwhile, BF_4^- and ClO_4^- are similarly sized, but produce different $\chi_M T$ properties, which suggest other factors (perhaps number and/or strength of intermolecular interactions) also play a part.
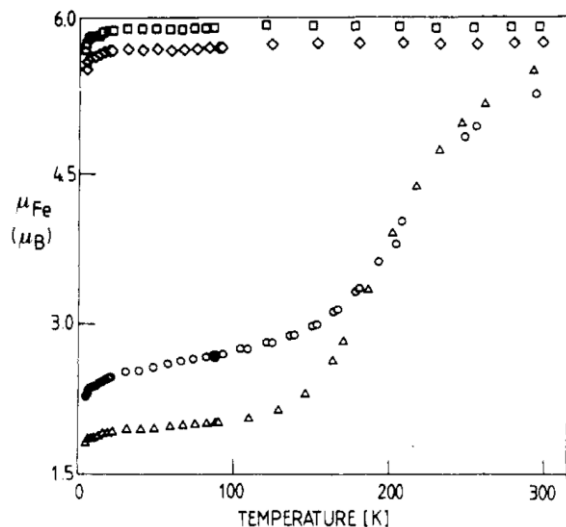
Figure 1.2. Magnetic moments vs temperature for [Fe(salen)(imidazole)$_2$]X complexes: X = BPh$_4^-$ (diamonds), ClO$_4^-$ (triangles), BF$_4^-$ (circles) or PF$_6^-$ (squares). Reproduced from reference 16.

Another example where spin-state switching properties are correlated to anion size in solid state studies is the series of compounds [Fe(HL^{Me})$_3$]X$_2$ (X = PF$_6^-$, ClO$_4^-$ or BF$_4^-$, HL^{Me} = 1-(((2-methylimidazol-4-yl)methylidene)amino)-2-pyrid-2-ylethane).[17] The complexes present a one-dimensional chain of cations formed by intermolecular hydrogen bonds. Anions hydrogen-bond to ligands not involved in chain formation, and appear to affect the cooperativity of the spin transition. The authors propose that a smaller anion allows for more interchain cooperativity, which could explain why the steepness of the spin transition (X = PF$_6^-$ < X = ClO$_4^-$ < X = BF$_4^-$) correlates inversely with the size of the anion: BF$_4^-$ < ClO$_4^-$ < PF$_6^-$.

While many solid state studies of hydrogen bonding are in the literature, we are most interested in anion-dependent spin switching complexes that are air- and water-*stable* in solution. One reason this is difficult is that many spin crossover complexes use Fe(II) complexes, which are air- and water-*sensitive*. As a first step toward that goal, we have investigated spin transition properties and modes of interaction in dichloromethane solutions.

An initial study in our lab showed distinct SC properties in the solid state for the complexes [Fe(H$_2$bip)$_3$]X$_2$ (H$_2$bip = 2,2'-bi-1,4,5,6-tetrahydropyrimidine and X = Br$^-$, BPh$_4^-$, I$^-$, ClO$_4^-$, Cl$^-$ or NO$_3^-$)[18] and solution measurements (Evan's method)[19] show that at 223 K, [Fe(H$_2$bip)$_3$](BPh$_4$)$_2$ and [Fe(H$_2$bip)$_3$]Br$_2$ are essentially in the HS and LS states respectively. Moreover, due to shifts in the position of the N-H peak in the NMR, it is likely that N-H⋯Br$^-$ hydrogen-bonds are taking place in the Br$^-$ salt that are not taking place in the BPh$_4^-$ salt.
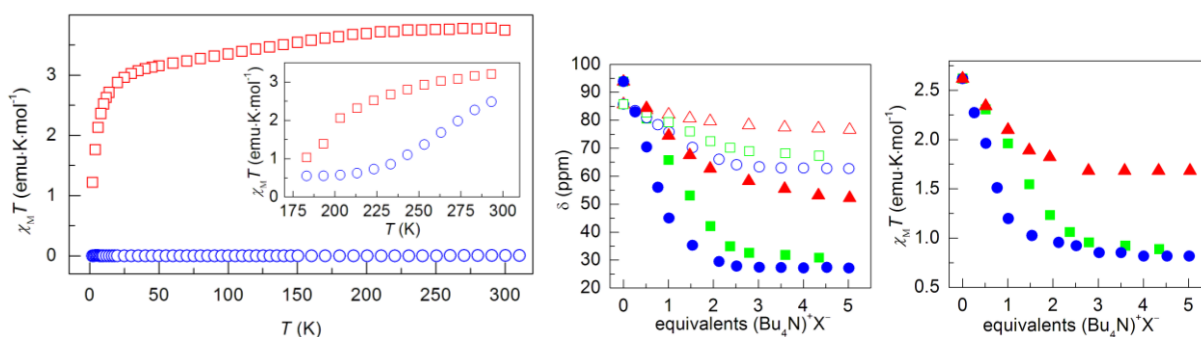
Figure 1.3. Left: $\chi_M T$ vs. T for [Fe(H$_2$bip)$_3$](BPh$_4$)$_2$ (□) and [Fe(H$_2$bip)$_3$]Br$_2$ (○). Center: N–H NMR shifts during titration of [Fe(H$_2$bip)$_3$](BPh$_4$)$_2$ with Br$^-$ at 293 K (open data) and 233 K (closed data). Right: $\chi_M T$ vs. T at 233 K during titration of [Fe(H$_2$bip)$_3$](BPh$_4$)$_2$ with Br$^-$. Reproduced from reference 18.

Focusing on the strong Br$^-$ interactions, we set out to tune the ligand field of the metal center. Retaining two H$_2$bip ligands provides opportunity for hydrogen bonding, while substitution of the third ligand position allows for inclusion of weaker or stronger field ligands. Our attempts to tune the ligand field result in heteroleptic complexes with highly labile ligands and poor stability in solution. Others in our group are working on the preparation of symmetric and asymmetric hexadentate complexes with greater stability in solution that maintain options for tunability.[20] Meanwhile, in order to successfully employ cation–anion hydrogen bonding for sensors, we strive to *first* understand the effect of hydrogen bonding on the ligand field relative to a ligand substituent. This work is presented in Chapters 2 and 3.

1.4 Magnetic Bistability and Single-Molecule Magnets

Magnetic compounds exhibit slow relaxation of magnetic bistability such that an induced field will persist even in the absence of an external magnetic field. One class of such compounds is often referred to as single molecule magnets (SMMs). Magnetic bistability in these complexes is observed as a magnetic hysteresis curve (see Figure 1.4). The details of the curve are as follows: initially, there is no applied field and no magnetization. Subsequently, a magnetic compound will demonstrate field-dependent magnetization until saturated magnetization is achieved. At this point, although the field may increase or decrease, the remanant magnetization will persist until a sufficient negative field (coercive field) is applied to cause a reversed magnetization. When the reversed magnetization is saturated, remanent magnetization will again persist until a positive field is applied to restore the original saturated magnetization.[21]
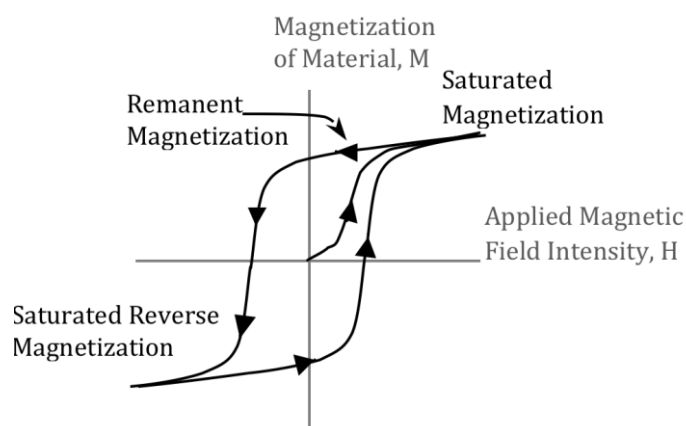
Figure 1.4. A generic hysteresis loop resulting from magnetization of a compound.

The presence of a hysteresis below a specific temperature makes SMMs appear more like bulk magnets than paramagnetic compounds. However, bulk magnets can be thought of as collections of superparamagnetic sub-domains, while a SMM *is* a superparamagnet. In a bulk magnet, each region experiences magnetization due to unpaired electrons, but above the ordering temperature it can fluctuate rapidly. Below the ordering temperature, the magnetizaion does not

fluctuate as much: in an extended substance, this leads to an overall magnetism that is much larger than the external field. Conversely, magnetization in an isolated superparamagnet depends only on the spin of each molecule and a lack of long-range ordering will eliminate the remanant magnetization. The SMM will only exhibit hysteresis at a given temperature if there is a large barrier to spin reorientation.[22]

The barrier to spin reorientation, U, depends on three factors to determine whether a compound will exhibit magnetic bistability. First, a multinuclear compound should exhibit a large electron exchange coupling, $|J|$, which allows for an isolated ground state. A second factor is the magnetic anisotropy, D, is required to partially remove spin state degeneracy. Lastly, total spin of the system, S, which is determined by the number of unpaired electrons can be an important contributor.[23]
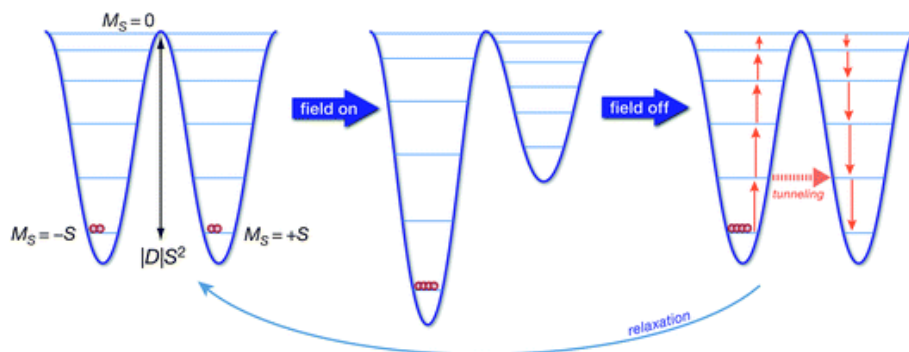
Figure 1.5. A schematic of the spin reorientation barrier, U, in the absence of an applied field (left) resulting in equal population of m_s states, in the presence of an applied magnetic field (center), and again in the absence of an applied magnetic field (right) with magnetic relaxation returning the potential energy to the initial state. Reproduced from reference 24.

Two types of anisotropy pertain to molecular magnets: easy-axis anisotropy and easy-plane anisotropy. The former occurs when the most stable magnetic moment orientation is parallel to a single direction. When D is negative, easy-axis anisotropy is observed: $+m_s$ and $-m_s$ states are degenerate with the $\pm m_s$ states lower in energy than the $m_s = 0$ state. As a result the double well

shown in Figure 1.5 is observed.[21] Contrarily, easy-plane anisotropy occurs when the stable magnetic moment orientation is not parallel to one single direction. This situation is associated with a positive D and the $m_s = 0$ state being lowest in energy, which gives a single well.[21,23] With a single well, the opportunity for magnetic bistability is removed.

In a compound exhibiting easy-axis anisotropy, the double well potential exists in the absence of an external magnetic field. This partial non-degeneracy is called zero-field splitting. At equilibrium, the wells will be equally populated, but when a magnetic field is applied, the states in one well will decrease in energy and the others will increase in energy (Figure 1.5). As the lower energy states increase in population, the compound exhibits a magnetization, which will persist until the field is removed and equilibrium is returned. This trait is comparable to paramagnetic compounds, however a SMM will exhibit a larger response to the external field and a slower reorientation time and therefore is considered a superparamagnet.[21]

The size of the spin reorientation barrier, U, is given by $U = S^2 |D|$ and $U = (S^2 - \frac{1}{4}) |D|$ for integer and half-integer values of S, respectively. From this, it is suggested that both S and the magnitude of D need to be large because they directly influence the magnitude of the barrier, which influences the likelihood of magnetic bistability of the compound.[23]

While SMMs display a hysteresis of the magnetization, measurement of the magnetic susceptibility can also provide information about the magnetic properties. Magnetic susceptibility is the ratio of the magnetism induced in a substance to the field inducing the magnetization. If the susceptibility is positive, the substance is paramagnetic and attracted to the field and if negative, the diamagnetic substance is repelled by the field. There are two ways to measure susceptibility: direct current (DC) measurements or alternating current (AC) measurements. DC susceptibility induces a magnetic moment from a constant applied magnetic field and thus provides the

equilibrium magnetization. AC susceptibility introduces a time-dependency: at higher frequencies, slow relaxation may cause a delay in the magnetization with respect to the field, which leads to an in-phase, or real, susceptibility and an out-of-phase, or imaginary, susceptibility. Out-of-phase susceptibility will show a maximum at the blocking temperature, which is the temperature below which the molecule behaves as a single domain magnet. Moreover, the maximum will be field-dependent if the intermolecular interactions are minimized.[25]

Through fitting susceptibility and magnetization data to exchange Hamiltonians, estimates of coupling parameters and anisotropy can be determined. In the following chapters, the relevant Hamiltonian is described and rationale for the parameters used is provided.

1.5 Examples of Single-Molecule Magnet Research

One of the most well-known SMMs is $[Mn_{12}O_{12}(CH_3COO)_{16}(H_2O)_4]$, Figure 1.6, commonly known as $Mn_{12}ac$ or Mn_{12}. The crystal structure and magnetic moment of this compound were reported by Lis in 1980,[26] but it was not until 1991 that the $S = 10$ spin state was experimentally determined.[27] The crystal structure for this complex shows tetragonal elongation for the outer eight manganese atoms, while the central Mn-O bond lengths are more consistent. Because Jahn-Teller distortions are predicted for Mn^{III} atoms but not Mn^{IV} atoms, the central manganese atoms are thought to be Mn^{IV} and the outer atoms are Mn^{III}. If these atoms were ferromagnetically coupled, the overall spin state would be $S = (8)(4*(½)) + 4(3*(½)) = 22$. Instead, the $S = 10$ state indicates antiferromagnetically coupled spin states ($S = 8(4*(½)) - 4(3*(½)) = 10$).
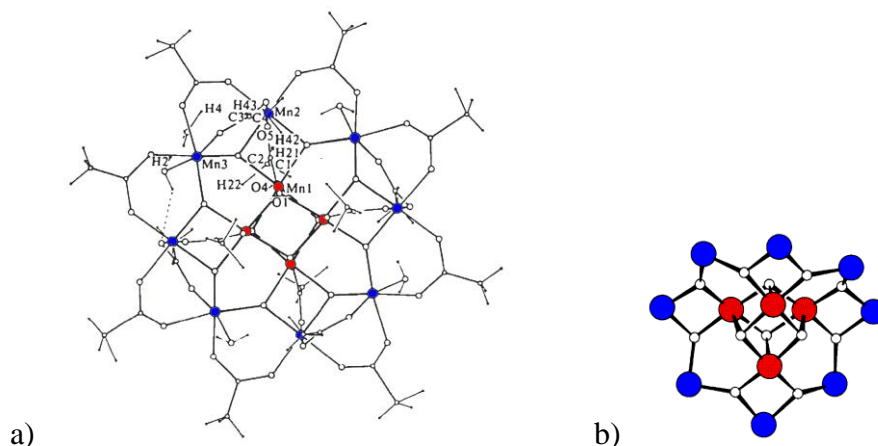
Figure 1.6. a) The crystal structure of $[Mn_{12}O_{12}(CH_3COO)_{16}(H_2O)_4]$ **b)** A schematic of the manganese and oxygen atoms to clarify the arrangement. Reproduced from references 26 and 28, respectively. The Mn^{III} atoms are blue and the Mn^{IV} atoms are red.

Finally, a magnetic hysteresis was observed in 1993: Sessolli et al. deduced that at 2.2 K a 1 T magnetic field was sufficient to reach saturation in the hysteresis.[28] This magnetization was maintained until a negative 1 T field was applied, which resulted in a reverse magnetization. An increase in magnetic field completed the hysteresis by returning the magnetization to the saturation state. For this complex, the barrier to reorientation is $U = 42$ cm^{-1}. Though influential, the magnetic bistability observed here only occurs at temperature accessible using liquid helium. In order to observe these properties at higher temperatures, the barrier must be increased. Synthetically, this should be possible by 1) increasing the spin, S, 2) increasing the magnetic anisotropy, D, or 3) increasing both S and D.

Increasing spin is the easier method to attempt to tune the molecules. Two examples are $\{Mn_9[W(CN)_8]_6 \cdot 24C_2H_5OH\} \cdot 12C_2H_5OH$ with $S = {}^{39}/_2$ and $[Mn^{II}\{Mn^{II}(CH_3OH)_3\}_8(\mu\text{-CN})_{30}\text{-}\{Mo^{V}(CN)_3\}_6] \cdot 5CH_3OH \cdot 2H_2O$ with $S = {}^{51}/_2$.[29-30] While increasing the nuclearity allows for easy synthesis of high-spin compounds, it does not ensure SMM properties. Neither the Mn_9W_6 complex nor the Mn_9Mo_6 complex show magnetic susceptibility properties characteristic of

SMMs. Furthermore, recent theoretical and experimental work propose that this outcome is not unexpected: synthesis of multinuclear complexes may actually *decrease* the anisotropy of the overall system relative to the individual ions.[24] Therefore, efforts to tune D should be more useful when successful.

Unfortunately, the second method of increasing the spin barrier by tuning D is quite difficult to achieve synthetically. Two routes are attempted in the literature: increasing D through geometrical constraints and increasing D through metal ion selection. The latter has been studied by using heavy *5d* transition metal ions such as tungsten[31] or *4f* lanthanides such as dysprosium[32] or terbium[33]. In fact, the current record holder for the highest observed barrier, 74 K, is reported for a mixed *3d-4f* complex consisting of an $Mn_{21}Dy$.[34] Others in our group have investigated tuning single ion anisotropy using uranium complexes.[35]

Structural modifications to improve the anisotropy are more varied in origin. To facilitate magnetic interactions, bridging ligands are frequently utilized. It is important to note that direct metal-metal orbital overlap is not required. Diamagnetic ligands are commonly used to couple the metal centers.[23] In addition, to emphasize the desired intramolecular interactions, it is necessary to minimize intermolecular interactions, which can be accomplished by using steric interactions of bulky ligands.[23] One notable example is a compound developed by Brechin and co-workers. The blocking temperature is modest: ~4.5 K,[1] however, the new compound was derived from systematic alterations of a known compound, as described in more detail below.

Specifically, structural distortion of $Mn^{III}_6O_2(sao)_6(O_2CPh)_2(EtOH)_4$ (sao = 2-hydroxy-benzaldehyde oxime) based on the use of sterically bulky ligands was analyzed. Substitution of sao with 2-hydroxyphenylpropanone oxime (Et-sao) led to $Mn^{III}_6O_2(Et\text{-}sao)_6(O_2CPh)_2(EtOH)_4$ (Figure 1.7a) and an increase from $S = 4$ to $S = 12$.[36] In the original complex, a set of three

antiferromagnetically coupled Mn^{III} atoms give rise to $S = (4*(½)) - (4*(½)) + (4*(½)) = 2$. Two of these sets are ferromagnetically coupled to give $S = 2 + 2 = 4$. In the new complex, all six atoms are ferromagnetically coupled to give $S = (6)(4*(½)) = 12$. However, the observed barrier $U = 36.9$ cm^{-1} is smaller than the theoretical barrier $U = 61.5$ cm^{-1}. This is thought to be due to populated low-lying energy states leading to increased tunneling events.[36] Further substitution of the benzoate ligand with 3,5-dimethylbenzoate led to $Mn^{III}_6O_2(Et-sao)_6(O_2CPh(Me)_2)_2(EtOH)_4$ (Figure 1.7b).[1] The magnetic data indicates that ferromagnetic coupling leads to an $S = 12$ state for this compound as well, but the new energy barrier, $U = 60.1$ cm^{-1}, is larger due to stronger exchange coupling.[1]
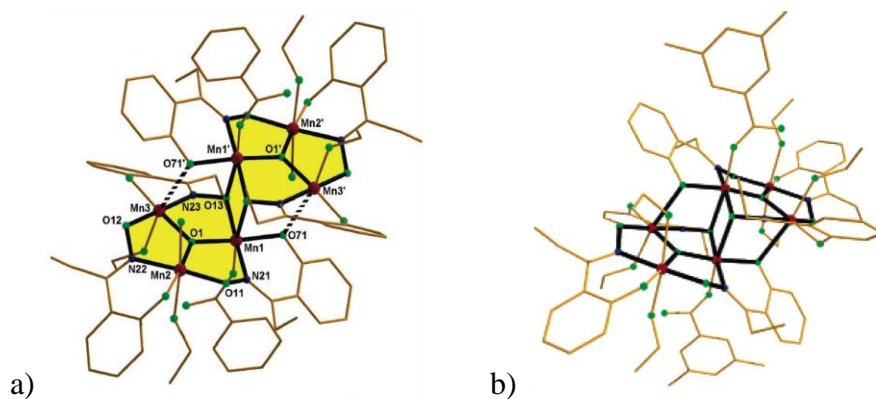
Figure 1.7. a) Crystal structure of $Mn^{III}_6O_2(Et-sao)_6(O_2CPh)_2(EtOH)_4$, one of the compounds systematically synthesized to increase magnetic properties. Reproduced from reference 36. **b)** Crystal structure of $Mn^{III}_6O_2(Et-sao)_6(O_2CPh(Me)_2)_2(EtOH)_4$, the current record holder for highest magnetic stability temperature. Reproduced from reference 1.

In chapters 4 and 5, our studies are presented that systematically probe the magnetic properties of complexes synthesized by others[37-42] in order to learn how slight structural variations affect magnetic anisotropy and slow relaxation.

Although oxygen-bridged compounds often produce very strong magnetic coupling, cyanide can also yield advantageous coupling. The use of cyanide enables direct alteration of S

and *D* through facile metal center substitution and symmetry modification.[29,43] Acetylide bridged

compounds can also engender strong magnetic coupling. Our previous work in this area focused

on trinuclear metal complexes bridged by triethynyl benzene (TEB) ligands.[44] The TEB ligand has

the opportunity to perform step-wise additions that can lead to sequentially larger molecules.

Moreover, predictions by Oshio, et al[45] suggest that arranging unpaired spins with non-axial

anisotropy at angles of 120° to one another should lead to axial anisotropy in the overall molecule.

To test this concept, Hoffert, et al synthesized and characterized the $[Fe(dmpe)_2Cl]_3TEB(OTf)_3$

complex (Figure 1.8).[44] The coupling and magnetic anisotropy in this complex is promising, but

illustrates the importance of ancillary ligand geometry on the orbitals that give rise to coupling.

Our predictions suggested that restricting movement of the dmpe ligands by using triethynyl

mesitylene instead of triethynyl benzene should allow for alignment of the molecular orbitals in

order to optimize coupling. The synthesis of new triethynyl mesitylene-based complexes and the

resulting magnetic experiments are explained in Chapter 6.
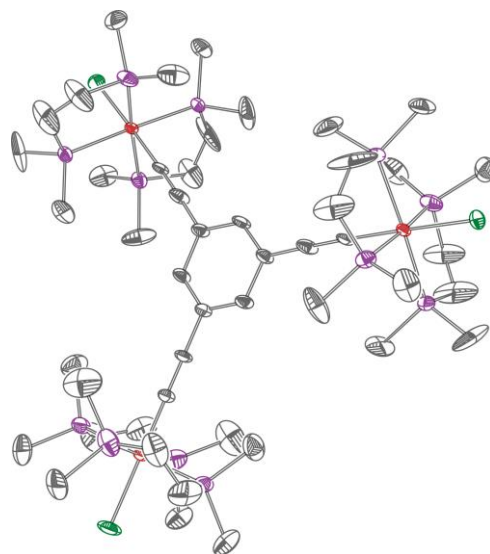
Figure 1.8. The $[Fe(dmpe)_2Cl]_3TEB$ complex. Reproduced from reference 44.

Through the magnetic studies presented herein, we will gain an understanding of the structural parameters that are available to tune the magnetic properties of transition metal complexes. With this information, we will be able to design complexes with useful properties that could be used in anion-sensing or molecular magnetism applications *without* the synthetic trial and error that is common for developments in these areas.

CHAPTER 1 REFERENCES

1. Milios, C. J.; Vinslava, A.; Wernsdorfer, W.; Moggach, S.; Parsons, S.; Perlepes, S. P.; Christou, G.; Brechin, E. K., *J. Am. Chem. Soc.* **2007**, *129*, 2754-2755.
2. Roubeau, O.; Clérac, R., *Eur. J. Inorg. Chem.* **2008**, *2008*, 4325-4342.
3. Krivokapic, I.; Zerara, M.; Daku, M. L.; Vargas, A.; Enachescu, C.; Ambrus, C.; Tregenna-Piggott, P.; Amstutz, N.; Krausz, E.; Hauser, A., *Coord. Chem. Rev.* **2007**, *251*, 364-378.
4. Bleuzen, A.; Marvaud, V.; Mathoniere, C.; Sieklucka, B.; Verdaguer, M., *Inorg. Chem.* **2009**, *48*, 3453-3466.
5. Brooker, S.; Kitchen, J. A., *Dalton Trans.* **2009**, 7331-7340.
6. Funck, K. E.; Hilfiger, M. G.; Berlinguette, C. P.; Shatruk, M.; Wernsdorfer, W.; Dunbar, K. R., *Inorg. Chem.* **2009**, *48*, 3438-3452.
7. Halcrow, M. A., *Coord. Chem. Rev.* **2009**, *253*, 2493-2514.
8. Real, J. A.; Gaspar, A. B.; Munoz, M. C., *Dalton Trans.* **2005**, 2062-2079.
9. Sato, O.; Cui, A.; Matsuda, R.; Tao, J.; Hayami, S., *Acc. Chem. Res.* **2007**, *40*, 361-369.
10. Sato, O.; Tao, J.; Zhang, Y.-Z., *Angew. Chem. Int. Ed.* **2007**, *46*, 2152-2187.
11. Weber, B., *Coord. Chem. Rev.* **2009**, *253*, 2432-2449.
12. Clemente-Leon, M.; Coronado, E.; Gimenez-Lopez, M. C.; Romero, F. M., *Inorg. Chem.* **2007**, *46*, 11266-11276.
13. Galet, A.; Gaspar, A. B.; Muñoz, M. C.; Bukin, G. V.; Levchenko, G.; Real, J. A., *Adv. Mater.* **2005**, *17*, 2949-2953.
14. König, E., *Structure & Bonding* **1991**, *76*, 51-152.
15. Alberto, M. E.; Mazzone, G.; Russo, N.; Sicilia, E., *Chem. Commun.* **2010**, *46*, 5894-5896.
16. Kennedy, B. J.; McGrath, A. C.; Murray, K. S.; Skelton, B. W.; White, A. H., *Inorg. Chem.* **1987**, *26*, 483-495.
17. Nishi, K.; Arata, S.; Matsumoto, N.; Iijima, S.; Sunatsuki, Y.; Ishida, H.; Kojima, M., *Inorg. Chem.* **2010**, *49*, 1517-1523.
18. Ni, Z.; Shores, M. P., *J. Am. Chem. Soc.* **2009**, *131*, 32-33.
19. Evans, D. F., *J. Chem. Soc.* **1959**, 2003-2005.
20. Klug, C. M., *In Preparation*.
21. Gatteschi, D.; Sessoli, R.; Villain, J., *Mesoscopic Physics and Nanotechnology* **2006**, 395.
22. Drago, R. S., *Physical Methods for Chemists*. 2nd ed.; Surfside Scientific Publishers: Gainesville, FL, 1992; p 750.
23. Gatteschi, D.; Sessoli, R.; Cornia, A., *Comp. Coord. Chem. II* **2004**, *7*, 779-813.
24. Neese, F.; Pantazis, D. A., *Faraday Discuss.* **2011**, *148*, 229-238.
25. Martien, D., Introdcution to AC Susceptibility: AC Magnetic Measurements. Quantum Design: San Diego.
26. Lis, T., *Acta Crystallogr., Sect. B: Struct. Sci* **1980**, *36*, 2042-2046.
27. Caneschi, A.; Gatteschi, D.; Sessoli, R.; Barra, A. L.; Brunel, L. C.; Guillot, M., *J. Am. Chem. Soc.* **1991**, *113*, 5873-5874.
28. Sessoli, R.; Gatteschi, D.; Caneschi, A.; Novak, M. A., *Nature* **1993**, *365*, 141-143.
29. Zhong, Z. J.; Seino, H.; Mizobe, Y.; Hidai, M.; Fujishima, A.; Ohkoshi, S.; Hashimoto, K., *J. Am. Chem. Soc.* **2000**, *122*, 2952-2953.
30. Larionova, J.; Gross, M.; Pilkington, M.; Andres, H.; Stoeckli-Evans, H.; Gudel, H. U.; Decurtins, S., *Angew. Chem. Int. Ed.* **2000**, *39*, 1605-1609.
31. Gogoi, N.; Thlijeni, M.; Duhayon, C.; Sutter, J.-P., *Inorg. Chem.* **2013**, *52*, 2283-2285.

32. Klokishner, S.; Reu, O., *Chem. Phys. Lett.* **2012**, *552*, 130-135.
33. Reu, O.; Palii, A.; Ostrovsky, S.; Wallace, W.; Zaharko, O.; Chandrasekhar, V.; Clerac, R.; Klokishner, S., *J. Phys. Chem. C* **2013**, *117*, 6880-6888.
34. Papatriantafyllopoulou, C.; Wernsdorfer, W.; Abboud, K. A.; Christou, G., *Inorg. Chem.* **2011**, *50*, 421-423.
35. Newell, B. S.; Schwaab, T. C.; Shores, M. P., *Inorg. Chem.* **2011**, *50*, 12108-12115.
36. Milios, C. J.; Vinslava, A.; Wood, P. A.; Parsons, S.; Wernsdorfer, W.; Christou, G.; Perlepes, S. P.; Brechin, E. K., *J. Am. Chem. Soc.* **2007**, *129*, 8-9.
37. Baddour, F. G. PhD Thesis. Boston University, Boston, 2013.
38. Baddour, F. G.; Fiedler, S. R.; Shores, M. P.; Golen, J. A.; Rheingold, A. L.; Bacon, J. W.; Doerrer, L. H., *Submitted* **2013**.
39. Baddour, F. G.; Fiedler, S. R.; Shores, M. P.; Golen, J. A.; Rheingold, A. L.; Doerrer, L. H., *Inorg. Chem.* **2013**, *52*, 4926-4933.
40. Dahl, E. W.; Baddour, F. G.; Fiedler, S. R.; Hoffert, W. A.; Shores, M. P.; Yee, G. T.; Djukic, J. P.; Bacon, J. W.; Rheingold, A. L.; Doerrer, L. H., *Chem. Sci.* **2012**, *3*, 602-609.
41. Coates, C. M.; Fiedler, S. R.; McCullough, T. L.; Albrecht-Schmitt, T. E.; Shores, M. P.; Goldsmith, C. R., *Inorg. Chem.* **2010**, *49*, 1481-1486.
42. Cantalupo, S. A.; Fiedler, S. R.; Shores, M. P.; Rheingold, A. L.; Doerrer, L. H., *Angew. Chem. Int. Ed.* **2012**, *51*, 1000-1005.
43. Sokol, J. J.; Hee, A. G.; Long, J. R., *J. Am. Chem. Soc.* **2002**, *124*, 7656-7657.
44. Hoffert, W. A.; Rappe, A. K.; Shores, M. P., *J. Am. Chem. Soc.* **2011**, *133*, 20823-20836.
45. Oshio, H.; Nakano, M., *Chem. Eur. J.* **2005**, *11*, 5178-5185.

CHAPTER 2: ANCILLARY-LIGAND HYDROGEN-BONDING EFFECTS ON ANION-DEPENDENT SPIN-STATE SWITCHING IN HETEROLEPTIC FE(II) COMPLEXES

2.1 Introduction

Compounds that exhibit spin crossover (SC) have been studied extensively since their discovery in 1931,[1] and those that change properties (e.g. color or magnetism) based on an external stimulus such as light, pressure or chemical interactions could be used as reporters in chemical sensing schemes. Several studies explore the effect of external stimuli,[2-3] covalent interactions,[4-5] and non-covalent solvent interactions[6-8] on SC compounds; non-covalent anion interactions, however, remain an under-examined field.

Anion sensing is a natural choice for spin-switching sensors due to the cationic nature of most Fe(II) SC complexes and the biological importance of anions as environmental pollutants. Indeed, cationic transition metal complexes that can non-covalently bind anions and effect a spin-state change could have potential in anion-sensing applications and devices. We have seen that anion binding can lead to spin-state changes in iron(II) complexes[9] and that ancillary ligand substitutions in heteroleptic species can lead to important changes in spin-switching properties.[5,10] As we strive to understand in more detail the non-covalent interactions that contribute to spin-state changes, we hypothesize that hydrogen-bonding interactions in the ancillary ligand can lead to predictable effects on anion-dependent spin-state switching.

We strive to study these effects in a controlled way by systematic variation of the ancillary ligand and comparison of resulting anion-binding properties. In previous cases, the identity of the ancillary ligand can be changed in order to vary the ligand field of the complex, though not always in the manner expected. In particular, we observed a more gradual spin state switching event for

[Fe(H$_2$bip)$_2$(6-Mebpy)]$^{2+}$ when cooling in solution relative to [Fe(H$_2$bip)$_3$]$^{2+}$ which we tentatively attributed to loss of a hydrogen-bonding site on the ancillary ligand.[11] However, a complex with *two* hydrogen-bonding sites on the ancillary ligand, [Fe(H$_2$bip)$_2$(pic)]$^{2+}$ shows a similarly gradual spin state transition.[10] A direct comparison of hydrogen bonding between these two ancillary ligands is complicated by factors such as ligand field strength and structural differences. Even with the related ligands pic, picMe and picMe$_2$ it is difficult to isolate hydrogen bonding effects from ligand field strength effects due to the dramatic changes in *Dq* values reported in the literature: pic, 1163 cm^{-1};[10] picMe, 1081 cm^{-1};[12] and picMe$_2$, 1180 cm^{-1}.[13]

The 2-imidazolines pizH and pizMe have similar structures and ligand field strengths (Figure 2.1 and Chapter 3), making them ideal for studies on the effect of hydrogen bonding in anion-binding studies. To this end, we report herein the preparations and anion-dependent spin-state properties of a structurally-related series of [Fe(H$_2$bip)$_2$(pizR)]$^{2+}$ complexes (Figure 2.1). We have also investigated crystal structures of related salts (Chapter 3) in attempts to elucidate the relevant structural parameters and intermolecular interactions in the solid state.
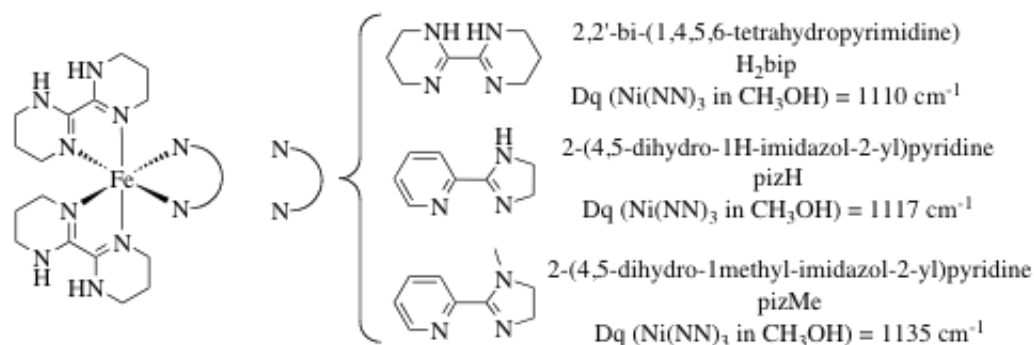
Figure 2.1. The ligands in use for anion-binding studies.

We report the synthesis and characterization of a structurally-related series of [Fe(H$_2$bip)$_2$(pizR)]X$_2$ complex salts (R = H (**2.1·X**) or Me (**2.2·X**), H$_2$bip = 2,2′-bi-1,4,5,6-

tetrahydropyrimidine, pizH = 2-(2'-pyridinyl)-4,5-dihydroimidazole, pizMe = 2-(2'-pyridinyl)-4,5-dihydro-1-methylimidazole, X = Br$^-$ or BPh$_4$$^-$). An investigation of solid-state interactions reveals that H$_2$bip ligands take part in primary anion–cation interactions while pizR ligands only take part in auxiliary interactions. Structural analyses of **2.1·Br** and **2.1·BPh₄** differentiate primary (H$_2$bip) and auxiliary (pizH) ligand-anion interactions. According to structural characterization of **2.2·Br** and **2.2·BPh₄**, the pizMe ligand does not take part in significant intermolecular interactions in the solid state. While both **2.1·BPh₄** and **2.2·BPh₄** demonstrate anion-dependent spin-state switching in solution, we find that not only the *presence* but also the *strength* of anion–cation interactions affects the anion-dependent spin-state switching. Some related Fe(II) pyridine-imidazole-(pimR)-containing complexes are also reported for comparison, though these complexes show poor solution stability properties.

2.2 Division of Labor

Synthesis of pimR-containing compounds and determination of the pimR ligand field strength was performed by Dr. Zhaoping Ni. Anion binding studies of **2.1·BPh₄** and the crystal structure of **2.1·Br** presented herein were also performed by Dr. Zhaoping Ni. Synthesis and characterization of **2.2·Br** and **2.2·BPh₄**, the crystal structure of **2.1·BPh₄** presented here, and all anion-binding studies of **2·BPh₄** were performed by Stephanie R. Fiedler.

2.3 Experimental Section

Preparation of Compounds. Compounds utilizing the pimR ligands, synthesized by Zhaoping Ni can be found in Appendix 1. The ligands 2,2′-bi-1,4,5,6-tetrahydropyrimidine (H$_2$bip),[14] 2-(2'-pyridinyl)-4,5-dihydroimidazole (pizH),[15] 2-(2′-pyridinyl)imidazole (pimH)[16] and

compound [Fe(H$_2$bip)$_2$Br$_2$][17] were synthesized according to the literature. The synthesis of 2-(2'-pyridinyl)-4,5-dihydro-1-methylimidazole (pizMe) was adapted from the literature.[15] All manipulations of iron complexes were performed inside a dinitrogen-filled glovebox (MBRAUN Labmaster 130). All non-deuterated solvents were sparged with dinitrogen, passed over alumina, and subjected to three freeze-pump-thaw cycles. All other compounds and reagents were obtained commercially and used as received.

2-(2'-pyridinyl)-4,5-dihydro-1-methylimidazole (pizMe). To a solution of pyridine carboxaldehyde (1.00 g, 9.3 mmol) in *tert*-butyl alcohol (50 mL) was added *N*-methyl-ethylenediamine (0.90 mL, 10.3 mmol); the resulting pale yellow solution was stirred at room temperature under dinitrogen for 30 minutes. Potassium bicarbonate (3.87 g, 28.0 mmol) and I$_2$ (2.96 g, 11.7 mmol) were added and the brown mixture was stirred for 3 h at 70 °C. Next, saturated aqueous Na$_2$SO$_3$ was added until the color faded to yellow. After separation, the aqueous layer was extracted with chloroform (2 × 50 mL) and the combined organic layers were washed with saturated aqueous NaHCO$_3$ (1 × 50 mL) and saturated aqueous NaCl (1 × 50 mL) and dried with Na$_2$SO$_4$. The solvent was removed by rotary evaporation to yield the product as a yellow oil in 71% yield (1.06 g). IR (KBr): $\nu_{C=N}$ 1666, 1589, 1563. MS: 162.1030 (pizMe+H)$^+$. ^{1}H NMR (300 MHz, CDCl$_3$) d = 3.037 (s, 3H), 3.50 (t, *J* = 10.1 Hz, 2H), 3.89 (t, *J* = 10.1 Hz, 2H), 7.33 (dd, *J* = 7.5 and 4.8 Hz, 1H), 7.75 (td, *J* = 7.7 and 1.6 Hz, 1H), 7.84 (m, 1H), 8.62 (d, *J* = 4.8 Hz, 1H) ppm. ^{13}C NMR (300 MHz, CDCl$_3$) δ = 36.15, 53.16, 54.57, 124.34, 124.5, 136.75, 148.72, 150.77, 165.87 ppm.

General procedure for synthesizing [Fe(H$_2$bip)$_2$(pizR)]Br$_2$. To a solution of [Fe(H$_2$bip)$_2$Br$_2$] (1 eq) in methanol (0.05 M) was added a solution of the pizR ligand (1 eq) in methanol (0.1 M), resulting in immediate color changes. The solution was stirred for an additional

15 min at room temperature. The solvent was removed in vacuo and the product was extracted into dichloromethane to separate it from trace unreacted [Fe(H$_2$bip)$_2$Br$_2$]. The mixture was filtered, and the filtrate was evaporated to obtain the [Fe(H$_2$bip)$_2$(pizR)]Br$_2$ complex salt as a free-flowing powder. This solid was washed with ca. 15 mL of diethyl ether and dried under vacuum at room temperature for 6 h to remove all trace solvent.

General procedure for synthesizing [Fe(H$_2$bip)$_2$(pizR)](BPh$_4$)$_2$. A solution of [Fe(H$_2$bip)$_2$(pizR)]Br$_2$ (1 eq) in methanol (0.05 M) was gradually added to a solution of excess NaBPh$_4$ (4 eq) in methanol (0.1 M), resulting in the formation of a colored precipitate. The mixture was stirred for an additional 15–60 min at room temperature. The solid was collected by filtration, washed with methanol (20 mL) and diethyl ether (10 mL), and dried to obtain [Fe(H$_2$bip)$_2$(pizR)](BPh$_4$)$_2$ as a powdered product.

[Fe(H$_2$bip)$_2$(pizH)]Br$_2$ (2.1·Br). 50 mg of pizH (0.34 mmol) was combined with 186 mg of [Fe(H$_2$bip)$_2$Br$_2$], affording 126.5 mg of product (54%). IR (KBr): $\nu_{\text{N–H}}$ 3227, 3121 cm^{-1}, $\nu_{\text{C=N}}$ 1608 cm^{-1}. ^{1}H NMR (CD$_2$Cl$_2$) 60.6, 43.3, 25.7, 24.1, 18.1, 10.8, 7.4, –10.5 ppm. Absorption spectrum (CH$_2$Cl$_2$): λ_{max} (ε_{M}) 484 (3936), 650(s), 691 (2744) nm (L·mol^{-1}·cm^{-1}). μ_{eff} (300 K): 3.42 μ_{B}. Anal. Calcd for C$_{24}$H$_{37}$Br$_2$FeN$_{11}$: C, 41.46; H, 5.36; N, 22.16. Found: C, 41.19; H, 5.28; N, 21.91. Crystals suitable for X-ray analysis were grown by slow diffusion of diethyl ether into a methanolic solution of **2.1·Br**.

[Fe(H$_2$bip)$_2$(pizH)](BPh$_4$)$_2$ (2.1·BPh$_4$). 100 mg of **2.1·Br** (0.145 mmol) was combined with 198 mg of NaBPh$_4$, affording 60 mg of product (35%). IR (KBr): $\nu_{\text{N–H}}$ 3397 cm^{-1}, $\nu_{\text{C=N}}$ 1615 cm^{-1}. ^{1}H NMR (CD$_2$Cl$_2$) 105.6, 95.3, 73.6, 62.9, 51.3, 47.8, 46.4, 40.0, 34.9, 29.6, 24.6, 20.5, 19.4, 13.8, 13.1, –15.3 ppm. Absorption spectrum (CH$_2$Cl$_2$): λ_{max} (ε_{M}) 458 (2317), 590 (2101) nm (L·mol^{-1}·cm^{-1}). μ_{eff} (300 K): 4.66 μ_{B}. Anal. Calcd for C$_{72}$H$_{77}$B$_2$FeN$_{11}$: C, 73.67; H, 6.61; N, 13.13.

Found: C, 73.57; H, 6.70; N, 13.28. Crystals suitable for X-ray analysis were grown by slow diffusion of diethyl ether into a dichloromethane solution of **2.1·BPh4**.

[Fe(H2bip)2(pizMe)]Br2 (2.2·Br). 55 mg of pizMe (0.34 mmol) was combined with 186 mg of [Fe(H2bip)2Br2], affording 113 mg of solid product. IR (KBr): ν_{N-H} 3237, 3126 cm^{-1}, $\nu_{C=N}$ 1608 cm^{-1}. ^{1}H NMR (CD2Cl2) 79.3, 63.6, 60.9, 57.1, 50.4, 49.5, 46.7, 41.1, 31.8, 27.2, 24.2, 17.4, 16.9, 15.6, 12.9, 9.2 ppm. Absorption spectrum (CH2Cl2): λ_{max} 482, 650(s), 695 nm. Elemental analysis is not consistent with the expected complex, vide infra. Crystals suitable for X-ray analysis were grown by slow diffusion of diethyl ether into a methanol solution of **2.2·Br**. The powdered impure compound was used as-is for the anion exchange, which provided pure product (*vide infra*).

[Fe(H2bip)2(pizMe)](BPh4)2 (2.2·BPh4). 102 mg of **2.2·Br** (0.145 mmol) was combined with 198 mg of NaBPh4, affording 22 mg of product (13%). IR (KBr): ν_{N-H} 3391, 3330 cm^{-1}, $\nu_{C=N}$ 1616 cm^{-1}. ^{1}H NMR (CD2Cl2) 85.3, 49.7, 30.9, 30.4, 23.7, 22.5, 19.5, 18.2, 17.4, 12.8 ppm. Absorption spectrum (CH2Cl2): λ_{max} (ε_M) 450 (2740), 545 (2820), 625 (2830) nm (L·mol^{-1}·cm^{-1}). μ_{eff} (300 K): 3.62 μ_B. Anal. Calcd for C73H79B2FeN11: C, 73.81; H, 6.70; N, 12.97. Found for crude powder: C, 73.64; H, 6.67; N, 12.89. Crystals suitable for x-ray analysis were grown by slow diffusion of diethyl ether into an ethanol solution of **2.2·BPh4**. Anal. Calcd for crystals with formula [Fe(H2bip)1.8(pizMe)1.2](BPh4)2·EtOH: C, 73.26; H, 6.90; N, 12.27. Found for crystals: C, 73.92, H, 6.59, N, 11.77.

X-Ray Structure Determinations. Structures were determined for the compounds listed in Table 1. All single crystals were coated in Paratone oil prior to removal from the glovebox. The crystals were supported on Cryoloops before being mounted on a Bruker Kappa Apex 2 CCD diffractometer under a stream of dinitrogen. Data were collected with Mo Kα radiation and a

graphite monochromator. Initial lattice parameters were determined from a minimum of 162 reflections harvested from 36 frames, and data sets were collected targeting complete coverage and 4-fold redundancy. Data were integrated and corrected for absorption effects with the Apex 2 software package.[18] Structures were solved by direct methods and refined with the SHELXTL software package.[19] Unless otherwise noted, thermal parameters for all fully occupied, non-hydrogen atoms were refined anisotropically. Hydrogen atoms were added at the ideal positions and were refined using a riding model where the thermal parameters were set at 1.2 times those of the attached carbon atom (1.5 times that for methyl protons).

The crystal structure of **2.1·Br** shows evidence of disordered solvent molecules. Analysis with SQUEEZE indicates a 523.5 Å^3 void space with 103 electrons/cell (~130 Å^3 void space and ~26 electrons per formula unit). This corresponds to one methanol and one water molecule in each unit cell; the locations of which can be approximately located by investigating the electron density map. Therefore, the refined structure contains these molecules, however, no hydrogen atoms are calculated due to the disorder. Presence of this disordered solvent is reflected, in part, by the higher than expected residual values. Based on our structural analyses of pizR ligands in Chapter 3 (*vide infra*), we are interested in the geometry of the N–H portion of the imidazole ring. Unfortunately, efforts to locate the hydrogen atom based on comparison of the electron density difference plots were unsuccessful. Any residual electron density assigned to hydrogen refined to unreasonable positions. Therefore, hydrogen atoms bound to all atoms, including nitrogen, are calculated based on ideal positions.

Initial refinement of **2.1·BPh4** gave a complex cation that appeared to be the homoleptic complex $[Fe(H_2bip)_3]^{2+}$, albeit with Fe–N bond distances consistent with a mixed-spin-state complex. From previous studies, it is known that $[Fe(H_2bip)_3](BPh_4)_2$ is high-spin at both 296 K

and 100 K.[9] Further refinement showed unaccounted spin density on two of the H_2bip ligands that resembled pizH. Refinement of free variables indicates ~0.98 pizH ligand and ~1.02 H_2bip ligand disordered approximately equally (site occupancy factors, s.o.f. of pizH = 0.47780 and 0.49880) over two ligand sites. The EADP constraint is used to make thermal parameters of disordered atoms equal. Further refinement details, including treatment of ligand conformational disorder, are presented in the cif file for **2.1·BPh₄**.

The crystal structure of **2.2·Br** initially refined to show the expected asymmetric unit with a 2:1 H_2bip:pizMe ratio. The crystal resolution was relatively poor and though the structure confirms the general structure of the desired complex, the residual values are high (See Table 1). Though the data is not publication quality, comparisons of the bond lengths (though with higher estimated standard deviations) with other complexes can be useful and so it is presented here for comparison. Some residual electron density suggests potential H_2bip/pizMe occupational disorder. However, attempts to refine the disorder are unsuccessful, resulting in atoms with non-positive definite (NPD) thermal parameters and low occupancy from the refined free variable. Even without disorder in the model, several atoms refined with NPD thermal parameters when refined anisotropically. Therefore, all carbon, nitrogen and hydrogen atoms are refined isotropically.

The crystal structure of **2.2·BPh₄** refined with two Fe(II) centers in the asymmetric unit. Each molecule contains ligand occupational disorder such that one H_2bip is permanent and the other two positions are partially occupied by both H_2bip and pizMe. For Fe1, the final pizMe:H_2bip ratio is 1.06:0.94 (pizMe s.o.f. = 0.54800 and 0.51133), while for Fe2, the final pizMe:H_2bip ratio is 1.32:0.68 (pizMe s.o.f. = 0.74247 and 0.57262). Therefore, Fe1 is best represented by $Fe(H_2bip)_{1.9}(pizMe)_{1.1}Br_2$ and Fe2 is best represented by $Fe(H_2bip)_{1.7}(pizMe)_{1.3}Br_2$. Some unaccounted electron density suggests further disorder of one H_2bip ligand, but attempts to model

it with partial pizMe occupancy result in NPD thermal parameters on atoms with low occupancy. Disordered atoms are refined with EADP constraints to make thermal parameters equal.

Magnetic Susceptibility Measurements. All samples were prepared under a dinitrogen atmosphere. Magnetic susceptibilities in CD_2Cl_2 solution were determined by Evans' method NMR using tetramethylsilane as an internal reference.[20] ^{1}H NMR spectra were recorded using Varian INOVA instruments operating at 300 or 400 MHz. Corrections for the change in solvent density with temperature were carried out according to the data provided for CH_2Cl_2 multiplied by an additional factor ($1.027 = 1.362/1.325$) accounting for the difference between the densities of CD_2Cl_2 and CH_2Cl_2 ($\rho = 1.362$ g/mL and 1.325 g/mL, respectively, at 298.16 K).[21]

Anion Binding Studies. Titrations of $^nBu_4NBr$ into dichloromethane solutions of **2.1·BPh₄** and **2.2·BPh₄** were monitored by electronic absorption and NMR spectroscopy according to procedures reported previously.[9-10,17] Job plots were prepared from data collected using a titration technique.[22-23] Solutions for electronic absorption-monitored titrations were prepared with concentrations ranging between 0.2–0.3 mM, while ^{1}H NMR solutions were prepared with concentrations in the range 4.0–6.2 mM.

Other Physical Measurements. Infrared spectra were measured with a Nicolet 380 FT–IR using KBr pellets. Elemental analyses were performed by Robertson Microlit Laboratories Inc. in Madison, NJ.

Table 2.1. Crystallographic data[a] for compounds [Fe(H₂bip)₂(pizH)]Br₂ (**2.1·Br**), [Fe(H₂bip)₂(pizH)](BPh₄)₂ (**2.1·BPh₄**), [Fe(H₂bip)₂(pizMe)]Br₂ (**2.2·Br**), and [Fe(H₂bip)₂(pizMe)](BPh₄)₂ (**2.2·BPh₄**).

	2.1·Br	**2.1·BPh₄**	**2.2·Br**	**2.2·BPh₄**
formula	$C_{25}H_{37}Br_2FeN_{11}O_2$	$C_{72}H_{77}B_2FeN_{11}$	$C_{25}H_{39}Br_2FeN_{11}$	$C_{73}H_{79}B_2FeN_{11}$
fw	739.33	1174.18	709.34	1187.94
color, habit	red rods	blue plates	brown prisms	purple prisms
T, K	120(2)	120(2)	120(2)	120(2)
space group	$P2_1/c$	Cc	$P2_1/c$	$P\bar{1}$
Z	4.0	4.0	4.0	4.0
a, Å	19.2151(5)	24.8754(12)	9.5437(6)	12.4221(19)
b, Å	9.3823(3)	10.9795(5)	30.6582(19)	14.505(2)
c, Å	19.3786(5)	24.3380(12)	12.2049(8)	34.681(6)
α, deg	90.000	90.000	90.000	89.779(9)
β, deg	107.513(2)	113.043(2)	109.291(4)	79.855(9)
γ, deg	90.000	90.000	90.000	89.951(10)
V, Å³	3331.68(16)	6116.8(5)	3370.6(4)	6151.2(17)
d_{calc}, g/cm³	1.474	1.275	1.398	1.283
GooF	1.061	1.032	3.645	1.520
$R_1(wR_2)^b$, %	5.21 (12.87)	3.72 (8.54)	17.35 (47.69)	7.91 (22.58)

[a] Obtained with graphite-monochromated Mo Kα (λ = 0.71073 Å) radiation.
[b] $R_1 = \Sigma||F_o| - |F_c||/\Sigma|F_o|$, $wR_2 = \{\Sigma[w(F_o^2 - F_c^2)^2]/\Sigma[w(F_o^2)^2]\}^{1/2}$ for $F_o > 4\sigma(F_o)$.

2.4 Results

Synthesis

Seeking ambient temperature anion-dependent spin-state switching properties and the ability to test hydrogen bonding effects for the ancillary ligand, we focused on the combination of Fe(II), H₂bip for anion binding, and 2-imidazoline ligands pizR (R = H, Me) for adjusting operating temperature and ancillary interactions. Electronic absorption spectra of homoleptic nickel complexes of each ligand[24] give Dq(pizH) = 1117 cm⁻¹, Dq(pizMe) = 1135 cm⁻¹ and Dq(H₂bip) = 1110 cm⁻¹, respectively. Weighted averages of the ligands give the expected ligand

fields for the heteroleptic complexes: $[Fe(H_2bip)_2(pizH)]^{2+}$ has a predicted $Dq = 1112$ cm^{-1} while $[Fe(H_2bip)_2(pizMe)]^{2+}$ has a predicted $Dq = 1118$ cm^{-1}. These are slightly smaller than the 1120–1240 cm^{-1} range of $Dq(Ni^{2+})$ values that Goodwin identified as the regime where spin-crossover in analogous Fe(II) complexes should be observed.[25-26] Dq values are highly solvent-dependent and the ligand field strength in non-polar solvents could differ significantly from what is observed here in methanol. Nevertheless, the similarity of the values suggests that spin-state differences observed via anion titrations could be correlated to intermolecular interactions rather than ligand field strength variations.

Syntheses of the heteroleptic complex salts proceed straightforwardly as illustrated in Figure 2.2. The stoichiometric combination of $[Fe(H_2bip_2)Br_2]$ and pizH in methanol gives an immediate color change from red to brown, indicating formation of the heteroleptic complex **2.1·Br**. The salt can be isolated as-is, or anion exchange can be performed by addition of excess NaBPh$_4$ affording **2.1·BPh₄** as a purple precipitate. In the case of the pizMe analogue, isolation of the navy blue **2.2·BPh₄** product from anion exchange is performed as a purification step: purple-brown powders of **2.2·Br** cannot be isolated with reproducible purity. Both **2.1·BPh₄** and **2.2·BPh₄** exhibit modest solubility in methanol: duplicate washes to remove **2.1·Br** and **2.2·Br** yield pure BPh$_4^-$-containing product, although in low yield. The **2.1·Br** and **2.2·Br** salts yield single crystals suitable for diffraction by ether diffusion into methanol, while crystals of the **2.1·BPh₄** and **2.2·BPh₄** salts are obtained by ether diffusion into dichloromethane (**2.1·BPh₄**) or ethanol (**2.2·BPh₄**). Compound **2.2·BPh4** is isolated in two forms: a crude powder with EA data that supports 2:1 ligand ratio of H$_2$bip:pizMe and a crystalline form where the structure and EA support a 1.8:1.2 ligand ratio of H$_2$bip:pizMe.
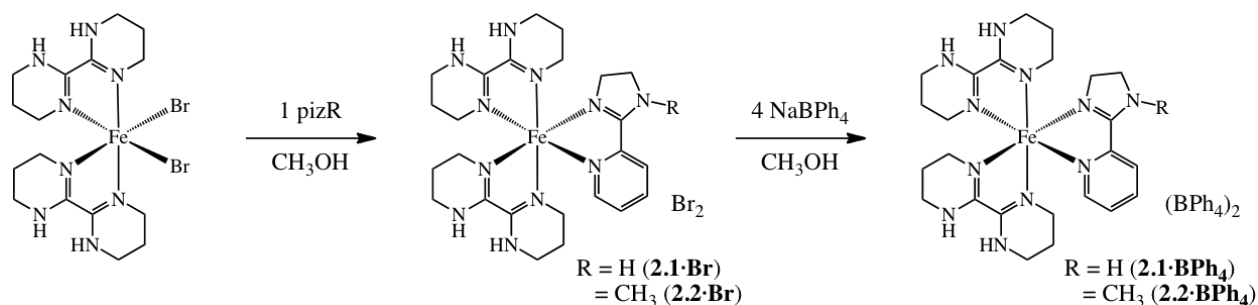
Figure 2.2. Syntheses of the complexes **2.1·X** and **2.2·X**.

We also considered the more-precedented 2-(2′-pyridinyl)imidazole (pimH) and 2-(2'-pyridinyl)-1-methylimidazole (pimMe) ligands in hopes of comparing them to the pizR-containing **2.1·X** and **2.2·X**. While several crystal structures featuring pimH are known,[27-29] the only reported structure containing pimMe as a ligand comes from a poorly diffracting crystal where the data was not deposited in the CCDC.[16] Meanwhile, our own efforts to study [Fe(H$_2$bip)$_2$(pimH)]X$_2$ were met with difficulty: [Fe(H$_2$bip)$_2$(pimH)]Br$_2$ shows solution instability evinced by significant changes in NMR spectra over 150 minutes, while titrations of [Fe(H$_2$bip)$_2$(pimH)](BPh$_4$)$_2$ with Br$^-$ are marred by complex precipitation which artificially lowers the observed $\chi_M T$ measurements. We suspect that these complications are due to ligand scrambling, such as we have observed from crystallization attempts over several days (See Appendix 1 for NMR stability studies, synthesis and characterization of [Fe(H$_2$bip)$_2$(pimH)]X$_2$ complexes).

Structural Comparisons and Cation–Anion Interactions

Although intermolecular interactions can be quite different in the solid-state versus solution, we have probed the solid-state structures of these complexes in hopes of identifying *possible* routes for solution anion–cation interactions. Literature precedent for these ligands is

exiguous, especially in crystal structures: the $CCDC^7$ contains only one report of $pizH^{30}$ in a coordination complex and no reports of pizMe.

All four complexes demonstrate distorted octahedral Fe^{2+} environments comprising three bidentate ligands (Figure 2.3). Due to disorder and low crystal quality, comparisons to previous heteroleptic complexes are difficult,[5,17] however, bond lengths and distortion parameters Σ and Θ are similar, indicating a similar overall coordination environment. H_2bip bond lengths, pizH bond lengths, Σ and Θ observed are similar to those observed for heteroleptic halide salts previously reported.[10] The average Fe–N bond lengths in all four complexes (Table 2.2) are suggestive of low spin complexes at 120 K.[31] Similarly, Σ and Θ are representative of a low-spin species with distortion from the small ligand bite angle.[32] The Fe–N_{pizH} bond lengths observed for **2.1·X** are slightly shorter than observed for pizH in a Ru^{2+} complex (2.027(8) Å), consistent with a similar bonding environment around a smaller metal atom.[30]

Table 2.2. Average Fe–N bond distances (Å) and distortion parameters Σ and Θ (°).[a]

	avg. Fe–N_{H2bip}	avg. Fe–N_{pizR}	avg. Fe–N [b]	Σ	Θ
2.1·Br	1.990(8)	1.981(6)	1.99(1)	66.3(7)	151
2.1·BPh4	2.09(4)	1.96(4)	2.01(5)	67(2)	165
2.2·Br	1.98(4)	1.95(3)	1.97(5)	65(3)	143
2.2·BPh4	1.99(5)	1.93(3)	1.97(8)	70(2)	156

[a] For determinations of Σ and Θ, see reference 32.
[b] Average value for all Fe–N distances in the structure.
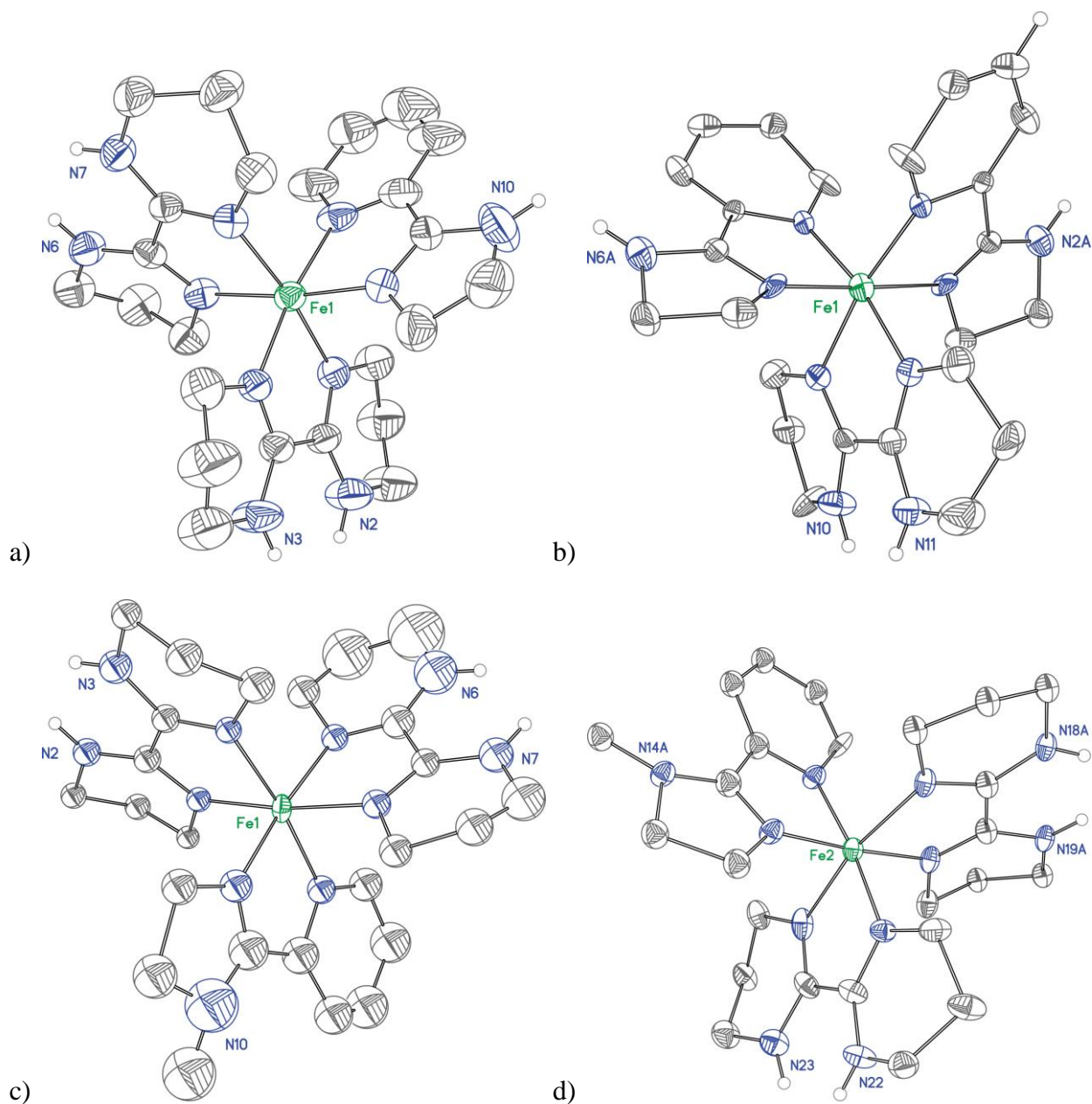
Figure 2.3. a) The cation in [Fe(H₂bip)₂(pizH)]Br₂ (**2.1·Br**) and b) one component of the disordered complex cation in [Fe(H₂bip)₂(pizH)](BPh₄)₂ (**2.1·BPh₄**). c) The cation in [Fe(H₂bip)₂(pizMe)]Br₂ (**2.2·Br**) and d) one component of the disordered complex cation in [Fe(H₂bip)₂(pizMe)](BPh₄)₂ (**2.2·BPh₄**). Calculated hydrogen atoms, except those bonded to nitrogen atoms, have been omitted for clarity. Atoms rendered at the 40% probability level.

Individual ligands show anion-dependent physical structure parameters. While Fe–N_{pizR} bond lengths are similar in **2.1·X** and **2.2·X**, mirroring our hypothesis that the ligand field strengths imparted by pizH and pizMe should be similar, the Fe–N_{H2bip} bond lengths show statistically significant increases from 1.99 Å in **2.1·Br** to 2.06 Å in **2.1·BPh₄**. It is also noteworthy that Fe–N_{pizH} and Fe–N_{H2bip} bond lengths are the same in **2.1·Br**, but Fe–N_{H2bip} bond lengths are longer than Fe–N_{pizH} in **2.1·BPh₄**. These trends indicate an H_2bip ligand field that is responsive to the change in anion, even though pizH is largely unaffected. Meanwhile, for **2.2·Br** and **2.2·BPh₄** the bond lengths are the same regardless of anion, suggesting that at 120 K, the complex is low spin and shows no correlation between anion and physical properties.

There are several hydrogen-bonding interactions for **2.1·Br** (Figure 2.4). Primary hydrogen bonding occurs between each Br⁻ anion and two N–H on each H_2bip ligand similarly to those observed previously in $[Fe(H_2bip)_3]^{2+}$ complexes.[9] Additional auxiliary hydrogen bonding occurs between a Br⁻ and the N–H of pizH, but at a single hydrogen-bonding site rather than two-fold hydrogen-bonding site as with H_2bip. As expected for **2.1·BPh₄**, there are no traditional hydrogen bonds between the cation and anion. Instead, N–H⋯π interactions (Figure 2.5 and Table 2.3) observed between H_2bip ligands and phenyl rings of the anion are within the range observed for similar interactions in the literature.[33-34] In all cases these are intermediate between an end-on and a side-on interaction. In the structure of **2.2·Br**, only primary hydrogen bonds between H_2bip ligands and Br⁻ are observed; the CH_3 moiety on pizMe does not take part in intermolecular interactions.
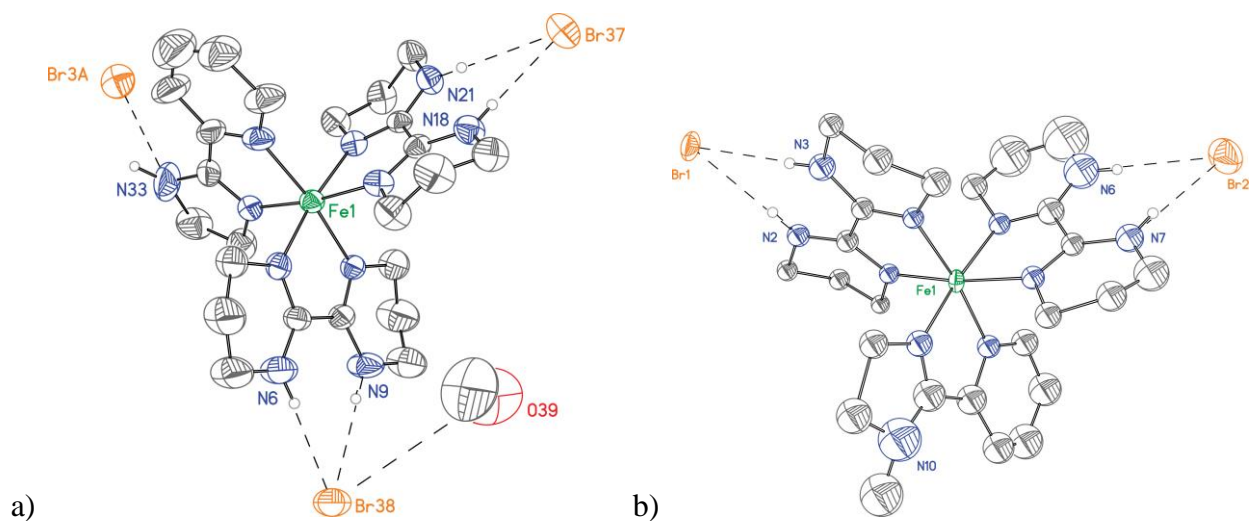
Figure 2.4. a) Cation–anion interactions for **2.1·Br**. Br3A is a symmetry generated equivalent of Br37. **b)** Cation–anion interactions for **2.2·Br**. 40% probability ellipsoids are shown for both structures.
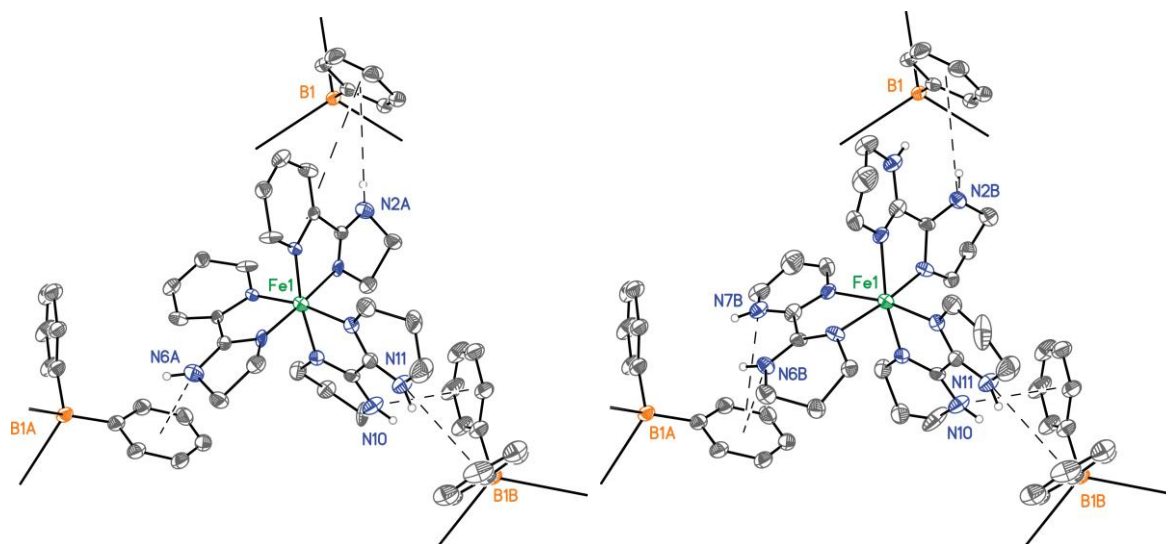
Figure 2.5. Cation–anion interactions for each disordered part of **2.1·BPh₄**. The BPh₄⁻ anions are abbreviated with only one or two phenyl rings shown; other phenyl rings are illustrated by bonds between boron and the centroid of the ring. Atom B1A and bound atoms are symmetry-generated equivalents of B1 and bound atoms as are atom B1B and bound atoms.

Table 2.3. Selected cation–anion interactions for compounds **2.1·Br**, **2.1·BPh4** and **2.2·Br**.

		2.1·Br		
N2···Br2A	3.452(5) Å	N2–H···Br2A	173.4(3)°
N3···Br2A	3.391(5) Å	N3–H···Br2A	167.8(3)°
N6···Br1	3.461(5) Å	N6–H···Br1	121.4(4)°
N7···Br1	3.432(9) Å	N7–H···Br1	174.5(4)°
N10···Br1A	3.379(8) Å	N10–H···Br1A	171.6(4)°

		2.1·BPh4		
N2a···C_6H_5	4.12 Å	N2a–H2a···C_6H_5	173.8°
N10···C_6H_5	3.226 Å	N10–H10···C_6H_5	160.6°
N11··· C_6H_5	3.654 Å	N11–H11···C_6H_5	168.8°
N6a···C_6H_5	3.542 Å	N6a–H6a···C_6H_5	161.6°
N2b···C_6H_5	3.877 Å	N2b–H2b···C_6H_5	176.9°
N6b···C_6H_5	4.348 Å	N6b–H6b···C_6H_5	170.3°

		2.2·Br		
N6···Br2	3.40(3) Å	N6–H···Br2	171(2)°
N7···Br2	3.49(2) Å	N7–H···Br2	178(2)°
N3···Br1	3.31(2) Å	N2–H···Br1	170(1)°
N2···Br1	3.32(2) Å	N3–H···Br1	171(1)°

Solution Spin-State Properties.

In general, HS Fe(II) complexes are labile in aqueous solution, the LS state less so.[35] This may be important for the complexes studied here, where ligand dissociation and rearrangement could give misleading information on guest-dependent spin-state switching. Indeed, ligand scrambling is observed when dichloromethane solutions of **2.1·BPh4** are allowed to stand for more than two weeks, as determined from a crystal structure that contains only [Fe(H$_2$bip)$_3$](BPh$_4$)$_2$ (See Appendix 1 for more information). To reduce the possibility of such deleterious rearrangements, all spectroscopic characterizations were carried out on fresh solutions of the complexes in the less polar dichloromethane solvent with rigorous exclusion of oxygen and moisture. Stability checks

were performed: the solution susceptibilities for **2.1·BPh₄** and **2.2·BPh₄** increase by no more than

0.02 emu·K·mol^{-1} after 150 min, which represents the amount of time needed to perform a titration

experiment. Given the relatively large errors encountered in Evans' method determinations of

solution susceptibilities,[36] the observed changes over time are virtually inconsequential.

Solution susceptibility data (Figure 2.6) show anion and temperature influences on the spin

states for **2.1·Br**, **2.1·BPh₄** and **2.2·BPh₄**. Compound **2.1·BPh₄** is mostly high spin at room

temperature ($\chi_M T = 2.72$ emu·K·mol^{-1}; 3.00 emu·K·mol^{-1} predicted for $S = 2$), but undergoes spin-

crossover as the temperature is decreased to 183 K (0.49 emu·K·mol^{-1}). Compounds **2.1·Br** and

2.2·BPh₄ also show temperature-dependent spin states, with $\chi_M T$ values of 1.46 and 1.64

emu·K·mol^{-1}, respectively, at 293 K, which decrease to 0.11 and 0.21 emu·K·mol^{-1}, respectively,

at 183 K.
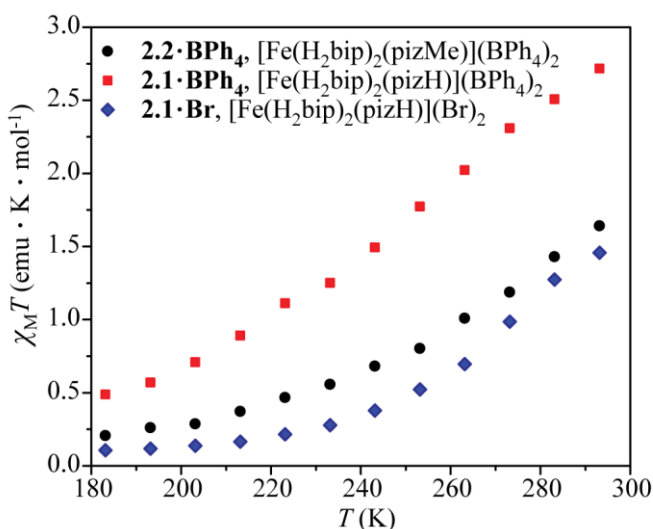
Figure 2.6. Plots of $\chi_M T$ vs. T for **2.1·Br** (blue diamonds), **2.1·BPh₄** (black circles) and **2.2·BPh₄**
(red squares) in solutions of CD₂Cl₂ upon cooling from 293 K to 183 K.

At 293 K, $\chi_M T$ of **2.1·BPh₄** decreases steadily from 2.64 emu·K·mol^{-1} to 1.91 emu·K·mol^{-}

^{1} as two equivalents of ^{n}Bu₄NBr are added while $\chi_M T$ of **2.2·BPh₄** decreases steadily from 1.75

emu·K·mol^{-1} to 0.87 emu·K·mol^{-1} as two equivalents of ^{n}Bu₄NBr are added (Figure 2.7).

Subsequent addition of ^{n}Bu$_4$NBr results in slight increases in $\chi_M T$, which we attribute to solution instability. The difference in estimated Dq between **2.1** (1112 cm^{-1}) and **2.2** (1118 cm^{-1}) manifests as a difference in $\chi_M T$ at each data point; the change in $\chi_M T$ as ^{n}Bu$_4$NBr is added is quite similar for **2.1** and **2.2**.

Variations in $\chi_M T$ during addition of ^{n}Bu$_4$NBr were compared for a crude powder of **2.2·BPh$_4$** as well as a crystalline sample to illustrate differences in composition between the two forms (Figure 2.7). A weighted average of the ligand fields associated with the crystalline form, Fe(H$_2$bip)$_{1.8}$(pizMe)$_{1.2}$ (1120 cm^{-1}), compared to the crude form, Fe(H$_2$bip)$_2$(pizMe) (1118 cm^{-1}), shows only a modest increase in Dq, however, the crystalline form shows a significantly lower $\chi_M T$ at 1.96 emu·K·mol^{-1} than the powder form at 2.31 emu·K·mol^{-1}.
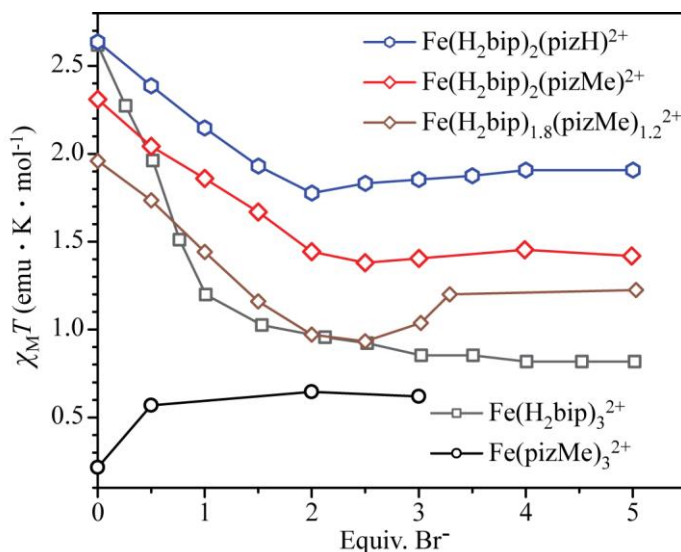
Figure 2.7. Variations in $\chi_M T$ for **2.1·BPh$_4$** (blue hexagons) and **2.2·BPh$_4$** (red diamonds) as Br$^-$ is added to solutions in CD$_2$Cl$_2$. For comparison, titrations of the crystalline form of **2.2·BPh$_4$** (brown diamonds), Fe(H$_2$bip)$_3$ (reference 9; grey squares) and Fe(pizMe)$_3$ (black circles) are also shown; see text for explanations. Lines shown are guides to the eye.

Plots of $\chi_M T$ during addition of ^{n}Bu$_4$NBr to [Fe(H$_2$bip)$_3$](BPh$_4$)$_2$ show a more dramatic decrease from 2.62 emu·K·mol^{-1} to 0.82 emu·K·mol^{-1} over two equivalents[9] while

[Fe(pizMe)$_3$](BPh$_4$)$_2$ (other details of this complex are described in Chapter 3) shows no change due to addition of ^{n}Bu$_4$NBr. These trends support our conclusion that H$_2$bip is interacting strongly with the anion to effect a spin state change while the auxiliary ligand pizMe does not affect the spins state through anion interactions.

By comparison with ^{1}H NMR spectra of [Fe(H$_2$bip)$_3$](BPh$_4$)$_2$ and [Fe(H$_2$bip)$_3$]Br$_2$, ^{1}H NMR spectra of [Fe(H$_2$bip)$_2$(pizR)](BPh$_4$)$_2$ were assigned and peak shifts during titration with Br$^-$ were monitored. In both **2.1·BPh$_4$** and **2.2·BPh$_4$**, chemical shifts (δ) of the ligand protons shift upfield as zero to 2.5 equivalents of Br$^-$ are titrated. From 2.5 to five equivalents bromide added, the δ values remain nearly constant (Figure 2.8). Peaks belonging to H$_2$bip shift only slightly in **2.1·BPh$_4$** and **2.2·BPh$_4$**, while δ values for pizMe and pizH tend to have larger shifts.
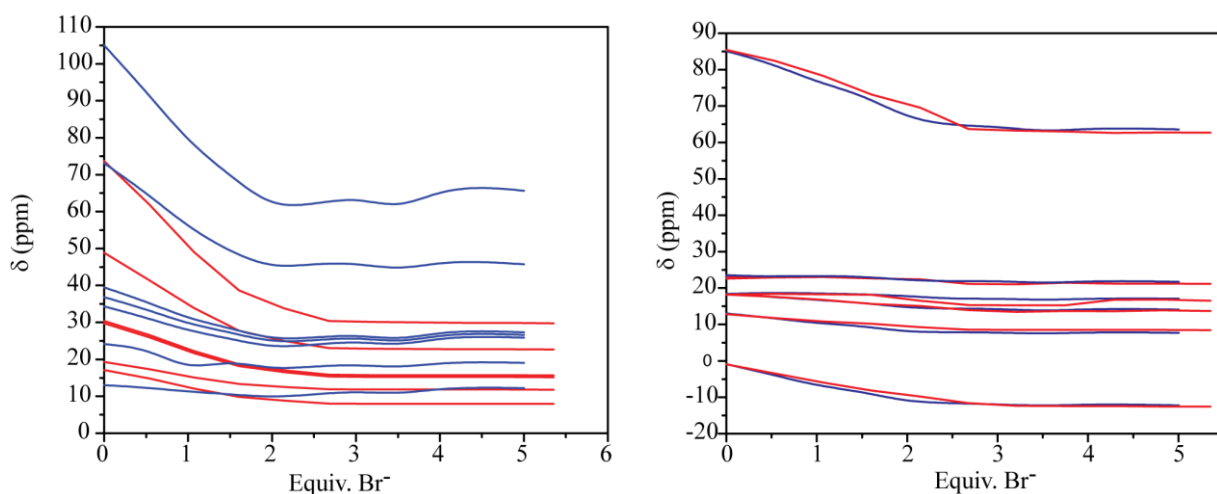
Figure 2.8. Variations in NMR peak positions as Br$^-$ is added to solutions in CD$_2$Cl$_2$. Left: NMR peaks corresponding to pizH in **2.1·BPh$_4$** (blue) and pizMe in **2.2·BPh$_4$** (red); Right: NMR peaks corresponding to H$_2$bip in **2.1·BPh$_4$** (blue) and in **2.2·BPh$_4$** (red).

Solution UV–visible spectroscopic titrations of **2.1·BPh$_4$** and **2.2·BPh$_4$** performed at 293 K show similar properties for each cation. Absorbance values for **2.1·BPh$_4$** and **2.2·BPh$_4$** decrease, while signals for **2.1·Br** and **2.2·Br** increase as two equivalents of Br$^-$ are added. For both

2.1·BPh4 and **2.2·BPh4**, the absorbance values decrease slightly after two equivalents of bromide are added, suggesting further chemical changes in solution as we observed for other heteroleptic complexes.[10] Complex **2.1** demonstrates slightly lower solution stability as the absorption peaks continue to shift away from **2.1·Br** while those in **2.2** do not: this is illustrated by the more flat slope observed for **2.2** in Figure 2.7 after two equivalents. The Job plot for addition of Br⁻ in CH_2Cl_2 shows a maximum at 0.67 mole ratio bromide for **2.1·BPh4** and 0.65 mole ratio bromide for **2.2·BPh4** (Figure 2.9), indicating a 1:2 ratio of Fe:Br.
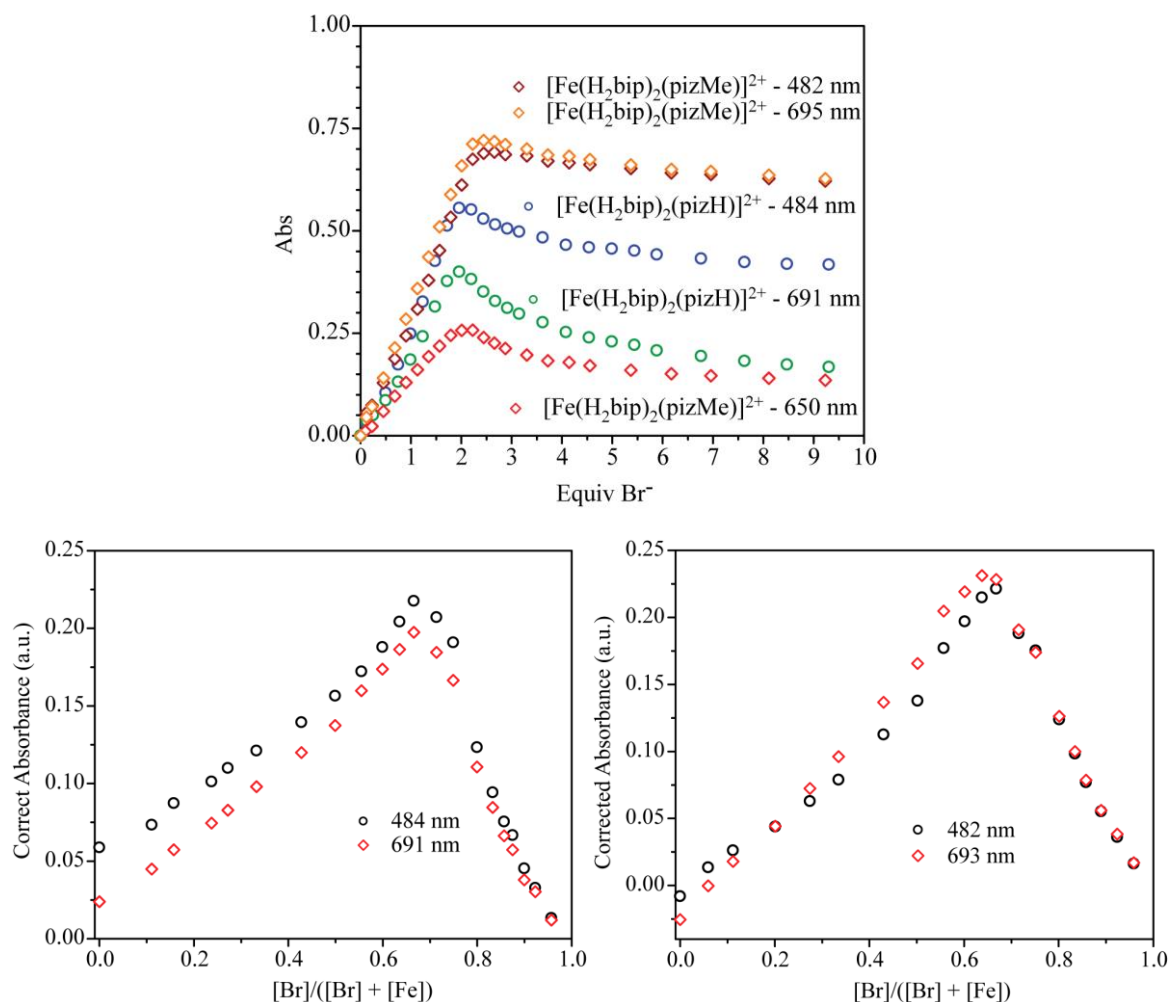
Figure 2.9. Top: variations in ΔAbs for **2.1·BPh4** and **2.2·BPh4** as Br⁻ is added to solutions in CH_2Cl_2. Bottom: Job plots for Br⁻ addition to **2.1·BPh4** (left) and **2.2·BPh4** (right).

2.5 Discussion

While all hydrogen bonds in **2.1·Br** are similar lengths as those observed in the literature,[28,37] the Br^- anion is chelated by H_2bip so we hypothesize the interaction is more significant ("concentrated") than that between Br^- and pizH, which is not chelated. The H_2bip–Br interaction likely dominates the anion-dependent spin-state switching properties. Although the observed N–H···π contacts in **2.1·BPh₄** may have some impact on the magnetic state, we expect that the more diffuse electron density as compared to Br^- results in a smaller effect on the spin state. Moreover, we expect that the interactions are further weakened due to the ligand disorder.

As opposed to N–H···Br interactions in **2.1·Br**, N–H···π interactions in **2.1·BPh₄** do not show a strong preference for one ligand over the other. Therefore, the anion-dependence observed for Fe–N_{H2bip} bond lengths is likely due to the hydrogen bonding that is occurring between H_2bip and Br^-. Meanwhile, the similar Fe–N_{pizH} bond lengths in both **2.1·Br** and **2.1·BPh₄** illustrate the relatively weak nature of anion interactions with pizH regardless of anion identity. Meanwhile, **2.2·Br** shows chelated N–H···Br interactions, but **2.2·BPh₄** shows not intermolecular contacts in the solid state. These two species show anion-*independent* structural parameters; the stronger ligand field of pizMe likely results in low spin species that do not illustrate anion effects.

The room-temperature susceptibility data (Figures 2.4 and 2.5) are indicative of mixed spin states, while the lower temperatures show nearly complete conversion to low-spin species. This is somewhat unexpected based on the low *Dq* values observed in methanol, but using a non-polar solvent (dichloromethane, for example) could reduce solvent-ligand interactions and enhance the ligand field strength relative to the values observed in methanol.

The observed susceptibility changes during NMR titrations indicate that the anion-binding event causes at least partial spin-state switching from HS to LS. Subsequent addition of $^nBu_4NBr$

after two equivalents does not significantly affect the value of $\chi_M T$. For both complexes the effect of Br^- on $\chi_M T$ is similar. If pizH hydrogen bonding were operative similarly to H$_2$bip, the effect should be clear: $\chi_M T$ would decrease over 3 equivalents instead of 2 equivalents.[9] This supports the assignment of *primary* Br^- binding to the available site on H$_2$bip and *auxiliary* Br^- binding to the pizR ligands. Moreover, the $\chi_M T$ of **2.1·BPh$_4$** during titration does not decrease to 1.5 emu·K·mol^{-1}, as observed for the room temperature $\chi_M T$ of **2.1·Br** (Figure 2.5). This could be due to other "dilution" of the hydrogen bonding, perhaps by other ions in solution or due to a change in ion pairing strenth.

Chemical shift changes observed for H$_2$bip peaks are likely a direct result of hydrogen bonding, which is predicted to be similar in **2.1·BPh$_4$** and **2.2·BPh$_4$**. Typically, hydrogen bonding is predicted to deshield hydrogen atoms and result in downfield shifts in diamagnetic species. The upfield shifts here mirror the effect of spin-state change, indicating that the hydrogen bonding is inducing a spin-state change. Meanwhile, shifts observed for pizR peaks are larger in **2.1** and **2.2** despite the similar change in $\chi_M T$. Perhaps the auxiliary interactions observed in the solid state are also operative in solution anion binding and thus are factoring in to the pizH ^{1}H NMR shifts. Although this hydrogen bonding may not induce a spin-state change it could still be affecting the ^{1}H NMR shifts of the protons on the pizH ligand.

Job plots of **2.1** and **2.2** suggest that maximum stability is associated with a 1:2 Fe:Br complexation ratio. This is notably different from the 1:3 Fe:Br ratio previously observed for Fe(H$_2$bip)$_3$(BPh$_4$), also suggestive of the minimal effect of auxiliary hydrogen bonding to pizH on the spin state. The slope of the Job plot is slightly steeper after two equivalents than before. This is reflective of the slight decrease in absorbance observed after two equivalents in the anion titration (vide supra).

2.6 Conclusions

The new cations $[Fe(H_2bip)_2(pizR)]^{2+}$ show another example of anion-dependent spin-state properties that can be altered by systematic variation of the ligand field. In solution, Evans' method NMR titrations show anion-dependent $\chi_M T$, while crystal structures show Fe–N bond lengths that depend on anion interactions. Fe–N bond lengths in pizH-containing complexes are shorter for H_2bip ligands taking part in primary hydrogen bonding to Br^- and are longer for H_2bip ligands taking part in N–H$\cdots\pi$ interactions with BPh_4^-.

Interestingly, Fe–N bond lengths at 120 K are similar for pizH and pizMe regardless of the intermolecular interactions taking place. Based on the differences in $\chi_M T$ in solution at room temperature, it is possible that room temperature structures would reflect the difference in ligand field strength. Moreover, integration of pizH and H_2bip in heteroleptic complexes shows little dependence on pizH–anion auxiliary hydrogen bonding or N–H$\cdots\pi$ interactions on the solution spin state. The pizMe complex, **2.2·BPh₄**, shows a similar decrease as **2.1·BPh₄** in $\chi_M T$ during anion titrations (0.88 emu·K·mol^{-1} for **2.2·BPh₄** vs 0.73 emu·K·mol^{-1} for **2.1·BPh₄**; similar when considering the $\pm10\%$ error in Evans' method measurements). Likewise, UV-vis titrations indicate anion-dependent spin state, but with similar effects regardless of auxiliary ligand identity.

2.7 Acknowledgments

CHAPTER 2 REFERENCES

1. Cambi, L.; Szego, L., *Ber. Dtsch. Chem. Ges.* **1931**, *64*, 2591-2598.
2. Bleuzen, A.; Marvaud, V.; Mathoniere, C.; Sieklucka, B.; Verdaguer, M., *Inorg. Chem.* **2009**, *48*, 3453-3466.
3. Real, J. A.; Gaspar, A. B.; Munoz, M. C., *Dalton Trans.* **2005**, 2062-2079.
4. Brooker, S.; Kitchen, J. A., *Dalton Trans.* **2009**, 7331-7340.
5. Venkataramani, S.; Jana, U.; Dommaschk, M.; Sönnichsen, F. D.; Tuczek, F.; Herges, R., *Science* **2011**, *331*, 445-448.
6. Amoore, J. J. M.; Neville, S. M.; Moubaraki, B.; Iremonger, S. S.; Murray, K. S.; Létard, J.-F.; Kepert, C. J., *Chem. Eur. J.* **2010**, *16*, 1973-1982.
7. Chernyshov, D.; Vangdal, B.; Tornroos, K. W.; Burgi, H.-B., *New J. Chem.* **2009**, *33*, 1277-1282.
8. Hostettler, M.; Toernroos, K. W.; Chernyshov, D.; Vangdal, B.; Buergi, H.-B., *Angew. Chem. Int. Ed.* **2004**, *43*, 4589-4594.
9. Ni, Z.; Shores, M. P., *J. Am. Chem. Soc.* **2009**, *131*, 32-33.
10. Ni, Z.; Shores, M. P., *Inorg. Chem.* **2010**, *49*, 10727-10735.
11. Ni, Z.; Fiedler, S. R.; Shores, M. P., *Dalton Trans.* **2011**, *40*, 944-950.
12. Uhlig, E.; Krahmer, R.; Wolf, H., *Z. Anorg. Allg. Chem.* **1968**, *361*, 157-&.
13. Nicholson, A. R.; Sutton, G. J., *Aust. J. Chem.* **1969**, *22*, 59-&.
14. Burnett, M. G.; McKee, V.; Nelson, S. M., *J. Chem. Soc., Dalton Trans.* **1981**, 1492-1497.
15. Ishihara, M.; Togo, H., *Tetrahedron* **2007**, *63*, 1474-1480.
16. Gerber, T. I. A.; Hosten, E.; Mayer, P.; Tshentu, Z. R., *J. Coord. Chem.* **2006**, *59*, 243-253.
17. Ni, Z.; McDaniel, A. M.; Shores, M. P., *Chem. Sci.* **2010**, *1*, 615-621.
18. *APEX 2*. Bruker Analytical X-Ray Systems, Inc: Madison, WI, 2008.
19. Sheldrick, G. M. *SHELXTL*, Version 6.14; Bruker Analytical X-Ray Systems, Inc.: Madison, WI, 1999.
20. Evans, D. F., *J. Chem. Soc.* **1959**, 2003-2005.
21. Yaws, C. L., *Thermodynamic and Physical Property Data*. Gulf Publishing Co.: Houston, 1992; p 6.
22. Hill, Z. D.; Maccarthy, P., *J. Chem. Educ.* **1986**, *63*, 162-167.
23. Maccarthy, P., *Anal. Chem.* **1978**, *50*, 2165-2165.
24. Fiedler, S. R. PhD Thesis: A Study of Magnetostructural Parameters Related to Spin Crossover and Single Molecule Magnetism. Colorado State University, Fort Collins, 2013.
25. Goodwin, H. A., *Top. Curr. Chem.* **2004**, *233*, 59-90.
26. Busch, D. H.; Bailar, J. C., *J. Am. Chem. Soc.* **1956**, *78*, 1137-1142.
27. Matouzenko, G. S.; Molnar, G.; Bréfuel, N.; Perrin, M.; Bousseksou, A.; Borshch, S. A., *Chem. Mat.* **2002**, *15*, 550-556.
28. Leita, B. A.; Moubaraki, B.; Murray, K. S.; Smith, J. P., *Polyhedron* **2005**, *24*, 2165-2172.
29. Matouzenko, G. S.; Perrin, M.; Le Guennic, B.; Genre, C.; Molnar, G.; Bousseksou, A.; Borshch, S. A., *Dalton Trans.* **2007**, 934-942.

30. Wu, A.; Masland, J.; Swartz, R. D.; Kaminsky, W.; Mayer, J. M., *Inorg. Chem.* **2007**, *46*, 11190-11201.
31. Gutlich, P.; Hauser, A.; Spiering, H., *Angew. Chem. Int. Ed.* **1994**, *33*, 2024-2054.
32. Halcrow, M. A., *Chem. Soc. Rev.* **2011**, *40*, 4119-4142.
33. A search of the CCDC was performed to find intermolecular N-H contacts with an aromatic 6-carbon ring. N-centroid distances were limited to those less than 4.3 Å with N-H-centroid angles between 120° and 180°. The average contact distance is 3.83[32]. This is only slightly longer than the contact distances between 3.2 Å and 3.8 Å observed for proteins in the following reference.
34. Steiner, T.; Koellner, G., *J. Mol. Biol.* **2001**, *305*, 535-557.
35. Taube, H., *Chem. Rev.* **1952**, *50*, 69-126.
36. Yatsunyk, L. A.; Walker, F. A., *Inorg. Chem.* **2003**, *43*, 757-777.
37. Steiner, T., *Acta Crystallogr., Sect. B: Struct. Sci* **1998**, *54*, 456-463.

CHAPTER 3: CRYSTALLOGRAPHIC STUDIES OF HOMOLEPTIC FE(II) COMPLEXES CONTAINING PYRIDINE-IMIDAZOLINE LIGANDS OF IMPORTANCE FOR SPIN CROSSOVER

3.1 Introduction

In previous efforts to understand the details of non-covalent binding contributions to spin-state switching, we have investigated and reported on heteroleptic Fe(II) complexes.[1-3] In these studies, we used two hydrogen-bond capable ligands and a third ligand of varying strength to attempt to tune the ligand field. In this way we can change the overall ligand field strength *and* maintain anion dependence via intermolecular hydrogen bonds. The ligand-field characteristics of imidazole-containing ligands make them suitable partners in Fe(II) coordination chemistry for the production of spin-crossover-capable materials. When studying pyridine-imidazole-containing complexes in heteroleptic species, we noticed that hydrogen bonding on the ligands could have different effects depending on the strength of the interaction (for more information see Chapter 2). Therefore, we became curious about other properties of this class of ligands.

Several iron complexes of pyridine-imidazole ligands have been structurally and magnetically characterized.[4-6] In contrast, the reduced pyridine-2-imidazoline ligands pizR (where R = H or Me(CH$_3$)) have not been as widely studied: only 1 structure of a complex containing pizH[7] has been reported and no structures of a complex containing pizMe have been reported in the CCDC. Moreover, our studies of pimR complexes were met with solution instability. Therefore, in this chapter, we explore the synthesis and structural chemistry of species where homoleptic complexes of pizR were targeted.

We report the preparations as well as structural and magnetic characterizations of a series of Fe(II) complexes featuring pyridine-2-imidazoline-containing ligands: $[Fe(pizH)_2Cl_2]$ (**3.1**), $[Fe(pizH)_3]Br_2$ (**3.2**), $[Fe(pizH)_3](BPh_4)_2$ (**3.3**), $[Fe(pizMe)Cl_2]_2$ (**3.4**), $[Fe(pizMe)_3]Br_2$ (**3.5**), $[Fe(pizMe)_3](FeCl_4)$ (**3.6**), $[Fe(pizMe)_3](BPh_4)_2$ (**3.7**), $[Fe(pizH)_2(SCN)_2]$ (**3.8**), and $[Fe(pizMe)_2(SCN)_2]$ (**3.9**), where pizH = 2-(2'-pyridinyl)-4,5-dihydroimidazole and pizMe = 2-(2'-pyridinyl)-4,5-dihydro-1-methylimidazole.

3.2. Division of Labor

Primary synthesis of **3.1**, **3.4**, and **3.6** was performed by Stephanie R. Fiedler. Optimized synthetic conditions, synthesis of other compounds and characterization of all Fe(II) compounds were performed by Kelsey A. Schulte.[8] Structural determination by x-ray crystallography of all compounds and ligand field strength determination of Ni(II) complexes were performed by Stephanie R. Fiedler.

3.3 Experimental Section

Preparation of Compounds. The ligand 2-(2'-pyridinyl)-4,5-dihydroimidazole (pizH) was synthesized according to the literature[9] and 2-(2'-pyridinyl)-4,5-dihydro-1-methylimidazole (pizMe) was synthesized as reported in Chapter 2.[9-10] All manipulations of iron complexes were performed inside a dinitrogen-filled glovebox (MBRAUN Labmaster 130). All non-deuterated solvents were sparged with dinitrogen, passed over alumina, and subjected to three freeze-pump-thaw cycles. All other compounds and reagents were obtained commercially and used as received. Synthesis of compounds **3.1**–**3.9** and related ^{1}H NMR, Evans' method $\chi_M T$ determination, elemental analysis, IR and UV-vis spectrophotometry are reported elsewhere.[8]

[Fe(pizH)₂Cl₂] (3.1). To a solution of $FeCl_2$ (0.028 g, 0.22 mmol in 6 mL of methanol (0.04 M) was added a solution of the pizH ligand (0.098 g, 0.66 mmol) in 6 mL of methanol (0.11 M), resulting in an immediate color change from colorless to purple. Crystals suitable for X-ray analysis were grown by slow diffusion of diethyl ether into a methanolic solution of **3.1** (97% yield).

[Fe(pizH)₃Br₂] (3.2). To a solution of $FeBr_2$ (0.048 g, 0.23 mmol) in 6 mL of methanol (0.04 M) was added a solution of the pizH ligand (0.100 g, 0.68 mmol) in 6 mL of methanol (0.11 M), resulting in an immediate color change from colorless to purple. Crystals suitable for X-ray analysis were grown by slow diffusion of diethyl ether into a methanolic solution of **3.2** (83% yield).

[Fe(pizMe)Cl₂]₂ (4). To a solution of $FeCl_2$ (0.196 g, 1.55 mmol,) in 15 mL of methanol (0.10 M) was added a solution of the pizMe ligand (0.250 g, 1.55 mmol) in 15 mL of methanol (0.10 M), resulting in an immediate change from colorless to red. Crystals suitable for X-ray analysis were grown by slow diffusion of diethyl ether into a methanolic solution of **3.4** (59% yield).

Ligand Field Strength Measurements. UV–visible spectra were recorded on a Hewlett-Packard 8453 spectrophotometer in an air-free glass cell. The λ_{max} obtained for the 1:6 Ni:ligand mixture was used to calculate the ligand field (*Dq*) value in order to mitigate the effect of ligand lability on the field strength.

[Ni(pizH)₃]Br₂ in methanol. To a solution of $NiBr_2$ (22 mg, 0.102 mmol) in methanol (8 mL) was added a solution of pizH (90 mg, 0.612 mmol) in methanol (1.00 mL) in 1 equiv. portions (0.17 mL of pizH-containing solution). A color change from pale yellow to pale green was observed over 5 minutes upon addition of the first two equivalents. Subsequent ligand

additions yielded a persistent brown-orange color. After each addition, the reaction was stirred for 5–10 min and monitored by UV–visible spectroscopy. Absorption spectrum of the 1:6 Ni:pizH solution (CH$_3$OH): λ_{max} 552, 783 (s), 892 nm.

[Ni(pizMe)$_3$]Br$_2$ in methanol. To a solution of NiBr$_2$ (23 mg, 0.1066 mmol) in methanol (8 mL) was added a solution of pizMe (174 mg, 1.08 mmol) in 2.00 mL of methanol in 1 equiv. portions (0.20 mL of pizMe-containing solution). A color change from pale yellow to pale green was observed over 5 minutes upon addition of the first two equivalents. Subsequent ligand additions yielded a persistent brown-orange color. After each addition, the reaction was stirred for 25–45 min and monitored by UV–visible spectroscopy. Absorption spectrum of the 1:6 Ni:pizMe solution (CH$_3$OH): λ_{max} 538 (s), 787 (s), 885 nm.

[Ni(H$_2$bip)$_3$]Br$_2$ in methanol. To a solution of NiBr$_2$ (22 mg, 0.102 mmol) in methanol (3 mL) was added a solution of H$_2$bip (102 mg, 0.612 mmol) in 2.00 mL of methanol in 1 equiv. portions (0.20 mL of H$_2$bip solution). A color change from pale yellow to colorless was observed upon addition of the first equivalent. Upon addition of the second and third equivalent, the initially formed solution was a pale lavender color but changed to light blue over several minutes. Subsequent ligand additions yielded a persistent pale lavender color. After each addition, the reaction was stirred for 25–45 min and monitored by UV–visible spectroscopy. Absorption spectrum of the 1:6 Ni:H$_2$bip solution (CH$_3$OH): λ_{max} 552, 792 (s), 901 nm.

X-Ray Structure Determinations. Structures were determined for the compounds listed in Table 3.1. All single crystals were coated in Paratone oil prior to removal from the glovebox. The crystals were supported on Cryoloops before being mounted on a Bruker Kappa Apex 2 CCD diffractometer under a stream of dinitrogen. Data were collected with Mo Kα radiation and a graphite monochromator. Initial lattice parameters were determined from reflections harvested

from 36 frames, and data sets were collected targeting complete coverage and 4-fold redundancy. Data were integrated and corrected for absorption effects with the Apex 2 software package.[13] Structures were solved by direct methods and refined with the SHELXTL software package.[14] Unless otherwise noted, thermal parameters for all fully occupied, non-hydrogen atoms were refined anisotropically. Except where noted, hydrogen atoms were added at the ideal positions and were refined using a riding model where the thermal parameters were set at 1.2 times those of the attached carbon atom (1.5 times that for methyl protons). Hydrogen atoms bound to nitrogen atoms with full occupancy (not disordered) in **3.1**, **3.2**, **3.3**, and **3.7** were found from electron density difference maps; positions were freely refined and thermal parameters were fixed to 1.2 times those of the attached nitrogen.

The initial solution of the structure of **3.1** revealed the observed structure, but with high residual values and an abnormally large 2nd weight parameter. Closer inspection of the data indicated pseudo-merohedral twinning present in the structure. This was resolved using the twin law 1 0 0 0 –1 0 0 0 –1, and the components refined to an 85:15 ratio.

Attempted data collection for **3.2** at 120 K displayed the expected structure, but with poor residuals. Closer inspection of the frames suggested crystal cracking at that temperature. Data collected at 275 K did not show signs of cracking; a structure was obtained at that temperature with lower final residuals.

The structure of **3.4** exhibited an inversion center located between the two iron centers such that the asymmetric unit is [Fe(pizMe)Cl$_{axial}$Cl$_{bridging}$] and the dinuclear complex is formed by symmetry generated atoms.

The structure of **3.7** at 120 K was impossible to solve in the expected monoclinic symmetry setting. Atoms were labeled in a triclinic solution and the ADDSYM function of the program

PLATON was used to transform the solution into the correct space group. The subsequent structure indicated positional disorder of one pizMe ligand such that 67% of the time the structure has a *mer* conformation and 33% of the time a *fac* conformation. Disordered atoms were modeled isotropically and made use of the SIMU command to refine thermal parameters in order to prevent unreasonable values. Residual electron density shows peaks near another pizMe ligand that suggests a potential additional site of positional disorder, however the largest peak at one of these positions is 1.07 e$^-$ so the disorder was not modeled.

Table 3.1. Crystallographic data[a] for compounds **3.1–3.8.**

	3.1	**3.2**	**3.3**	**3.4**
formula	$C_{16.9}H_{18}Cl_2FeN_6O_{1.2}$	$C_{26}H_{35}Br_2FeN_9O_2$	$C_{76}H_{67}B_2FeN_{11}$	$C_9H_{11}Cl_2FeN_3$
fw	451.59	721.30	1211.87	575.92
color, habit	blue prisms	red-brown prisms	purple prisms	red plates
T, K	120(2)	275(2)	120(2)	120(2)
space group	$P2_1/n$	$P2_1/n$	$P2_1/c$	$P\bar{1}$
Z	4.0	4.0	4.0	2.0
a, Å	9.7708(7)	9.5710(4)	19.5662(8)	8.9050(7)
b, Å	16.2407(11)	26.2871(10)	17.4547(6)	9.4601(7)
c, Å	12.3448(13)	12.6211(4)	19.4694(8)	15.4919(11)
α, deg	90.000	90.000	90.000	98.533(4)
β, deg	90.173(3)	104.203(2)	105.471(2)	90.169(4)
γ, deg	90.000	90.000	90.000	117.489(4)
V, Å^3	1958.9(3)	3078.3(2)	6408.3(4)	1141.11(15)
d_{calc}, g/cm^3	1.531	1.556	1.256	1.676
GooF	1.021	1.062	1.066	1.054
R_1 (wR_2)[b] %	3.14 (8.02)	4.99 (12.48)	7.39(17.55)	3.48 (7.53)

[a] Obtained with graphite-monochromated Mo Kα (λ = 0.71073 Å) radiation.
[b] $R_1 = \text{å}||F_o| - |F_c||/\text{å}|F_o|$, $wR_2 = \{\text{å}[w(F_o^2 - F_c^2)^2]/\text{å}[w(F_o^2)^2]\}^{1/2}$ for $F_o > 4\sigma(F_o)$.

Table 3.1 continued. Crystallographic data[a] for compounds **3.1–3.8.**

	3.5	3.6	3.7	3.8
formula	$C_{29}H_{39}Br_2FeN_oO$	$C_{27.7}H_{33}Cl_4Fe_2N_9O$	$C_{75}H_{73}B_2FeN_9$	$C_{18}H_{18}FeN_8S_2$
fw	745.36	761.38	1177.89	466.37
color, habit	purple prisms	purple prisms	purple prisms	red prisms
T, K	120(2)	120(2)	120(2)	120(2)
space group	$P2_1$	$Pca2_1$	$P2_1/c$	$P2_1/c$
Z	2.0	4.0	4.0	8.0
a, Å	9.2332(4)	16.9165(14)	12.3809(6)	15.668(2)
b, Å	16.8576(7)	9.9840(8)	14.4121(7)	17.374(3)
c, Å	10.2972(5)	19.6281(16)	34.4534(15)	14.929(2)
α, deg	90.000	90.000	90.000	90.000
β, deg	97.568(3)	90.000	95.200(2)	90.093
γ, deg	90.000	90.000	90.000	90.000
V, Å^3	1588.79(12)	3315.1(5)	6122.4(5)	4064.0(10)
d_{calc}, g/cm^3	1.558	1.526	1.278	1.524
GooF	0.775	1.067	1.037	1.033
R_1 $(wR_2)^b$ %	3.28 (9.62)	3.52 (8.20)	5.13 (11.93)	4.85 (11.66)

[a] Obtained with graphite-monochromated Mo Kα (λ = 0.71073 Å) radiation.
[b] $R_1 = å||F_o| - |F_c||/å|F_o|$, w$R_2 = \{å[w(F_o^2 - F_c^2)^2]/å[w(F_o^2)^2]\}^{1/2}$ for $F_o > 4\sigma(F_o)$.
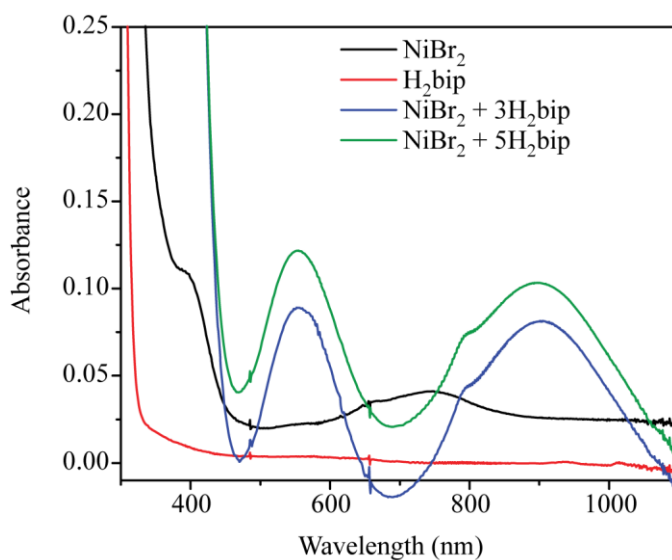
Figure 3.1. Electronic absorption spectra for titration of $NiBr_2$ with H_2bip in methanol at room temperature under air-free conditions.
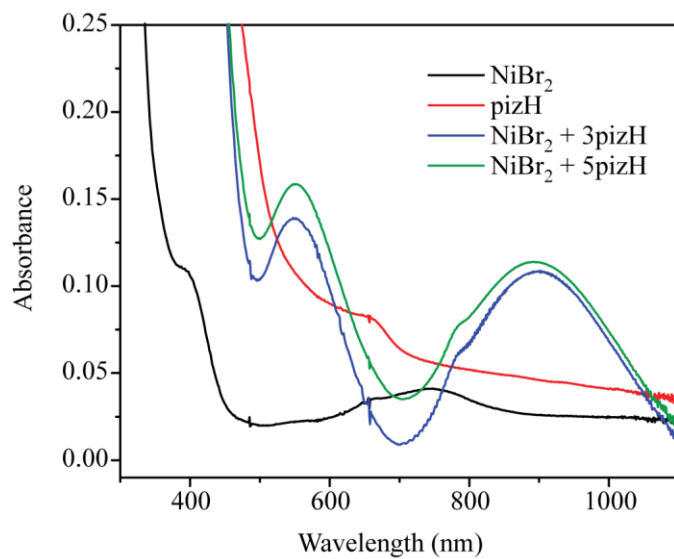
Figure 3.2. Electronic absorption spectra for titration of NiBr$_2$ with pizH in methanol at room temperature under air-free conditions.
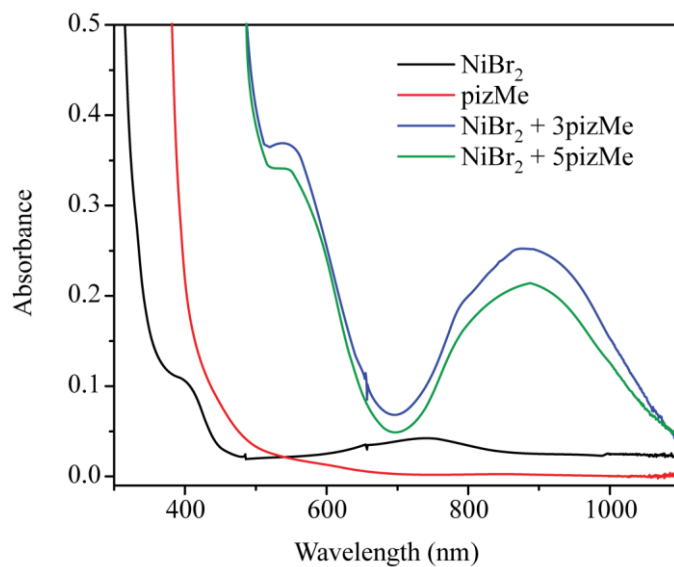
Figure 3.3. Electronic absorption spectra for titration of NiBr$_2$ with pizMe in methanol at room temperature under air-free conditions..

3.4 Results and Discussion

Ligand Field Strength Determination

Because strong charge transfer bands in Fe(II) complexes obscure the *d–d* transitions, homoleptic Ni complexes Ni(pizH)$_3$Br$_2$, Ni(pizMe)$_3$Br$_2$, and Ni(H$_2$bip)$_3$Br$_2$ were used to determine the ligand field strength generated by each ligand. Electronic absorption spectra (Figures 3.1–3.3) give Dq(pizH) = 1117 cm^{-1}, Dq(pizMe) = 1135 cm^{-1} and Dq(H$_2$bip) = 1110 cm^{-1}, respectively. Spectra were measured in methanol by step-wise addition of the NN ligand in one equivalence portions. Over the first three equivalents, some color changes and peak shifts occurred, but subsequent additions resulted in the same peak locations as shown in Figures 3.1–3.3. Due to changes in concentration, the absorbance shifted between equivalent five and equivalent six, but no other spectroscopic changes were observed.

The H$_2$bip ligand has been used previously to evoke anion-dependent spin crossover in homoleptic and heteroleptic Fe(II) complexes,[1-3,15] and the Dq value found here differs only slightly from the reported value of 1100 cm^{-1}, with differences attributed to variations in solvent and anion. The pizH and pizMe ligands show slightly larger Dq values than H$_2$bip, indicating stronger ligand fields, but within the range predicted to allow for spin crossover in Fe(II) complexes.[16-17]

Synthesis and crystallization

All compounds were synthesized using readily available Fe(II) reagents by stirring in methanol with a specific metal:ligand ratio (Figure 3.4). Compounds **3.4** and **3.6** were initially discovered serendipitously, but were optimized using the reaction conditions shown in Scheme 3.1 and reported elsewhere.[8] All compounds except **3.3**, **3.5**, and **3.7** were crystallized by slow

diffusion of diethyl ether into methanol. The BPh$_4$ salts, **3.3** and **3.7**, were crystallized by slow diffusion of diethyl ether into acetonitrile, while **3.5** crystallized by slow diffusion of diethyl ether into ethanol.

Crystal structures of **3.1**–**3.8** were obtained and parameters are contained in Table 3.1. The structures of **3.1** and **3.8** exhibit a distorted octahedral geometry consisting of two pizH ligands and two Cl$^-$ ligands (**3.1**) or two SCN$^-$ ligands (**3.8**). Compound **3.4** crystallizes as a dimer of pentacoordinate Fe(II) atoms with the coordination environment made up of one pizMe, one Cl$^-$ ligand and two bridging Cl$^-$ ligands. Structures of **3.2**, **3.3**, **3.5**, **3.6**, and **3.7** display three pizR ligands arranged around an Fe(II) cation in a distorted octahedral geometry. In addition, **3.6** contains a tetrahedral (FeCl$_4$)$^{2-}$ anion, while **3.2** and **3.5** each contain two Br$^-$ anions and **3.3** and **3.7** each have two (BPh$_4$)$^-$ anions. Selected bond distances and distortion parameters are contained in Table 3.2.
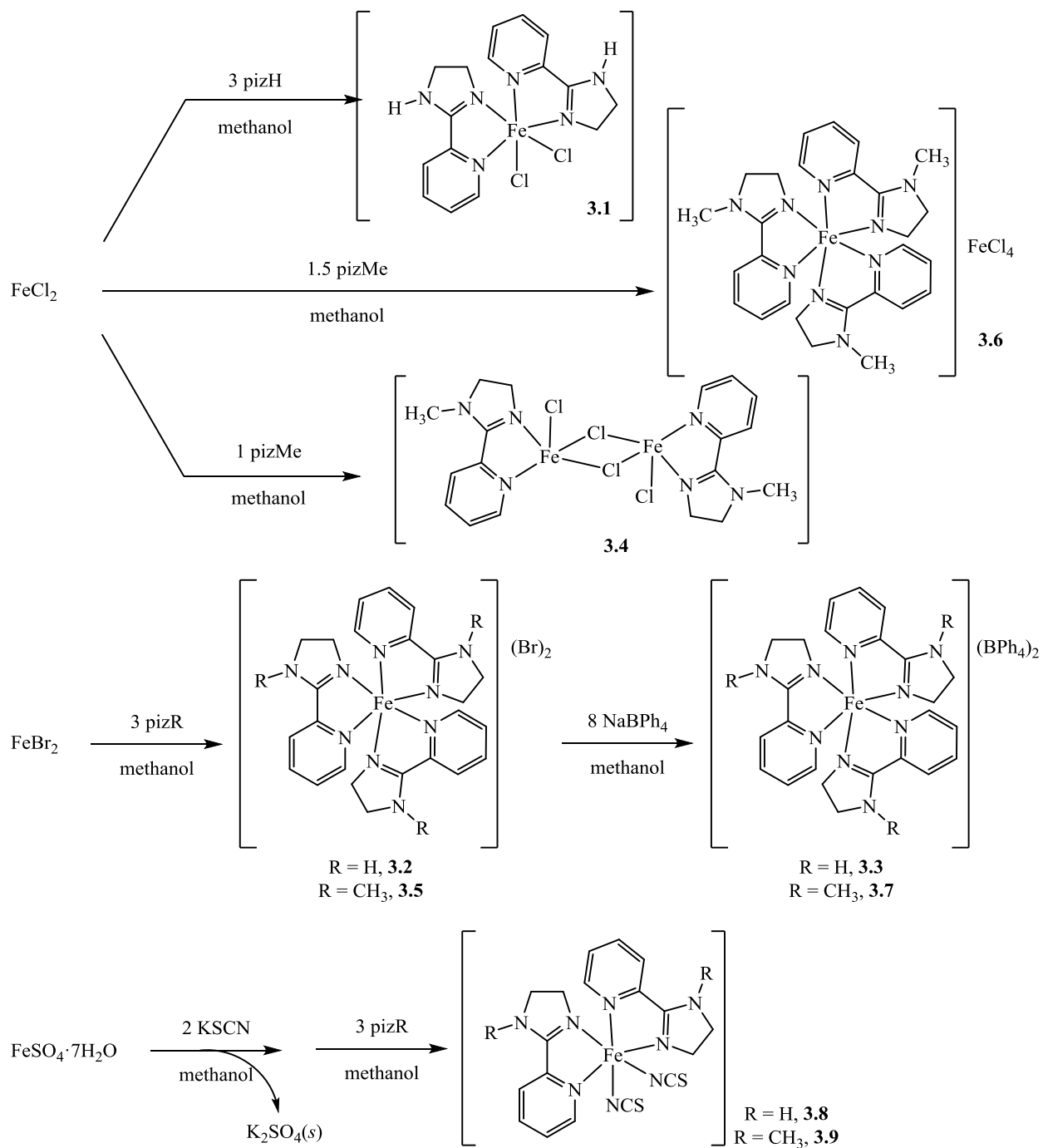
Figure 3.4. Synthetic routes used to isolate compounds **3.1**–**3.9**. Note that illustrations here are not meant to illustrate the isomer that is formed: for **3.2** and **3.6** the *mer* isomer is observed, while **3.3**, **3.5**, and **3.7** show disorder such that *mer* and *fac* are present.
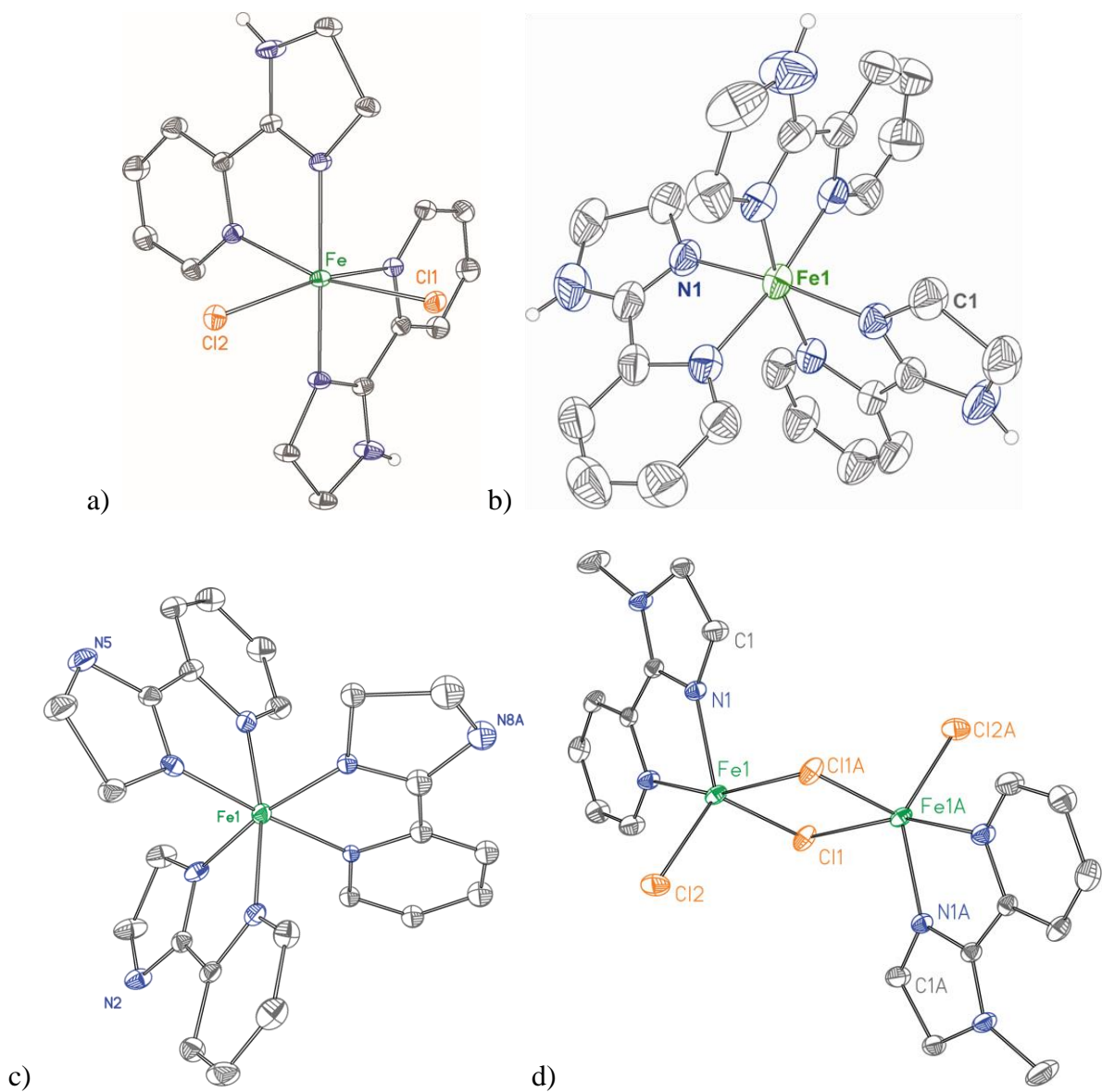
Figure 3.5. The crystal structures of **a)** [Fe(pizH)$_2$Cl$_2$] (**3.1**), **b)** Fe(pizH)$_3$Br$_2$ (**3.2**), **c)** Fe(pizH)$_3$(BPh$_4$)$_2$ (**3.3**), and **d)** [Fe(pizMe)Cl$_2$]$_2$ (**3.4**). Non-labeled grey atoms are carbon and hydrogen atoms have been omitted for clarity. Atoms are rendered at the 40% probability level.
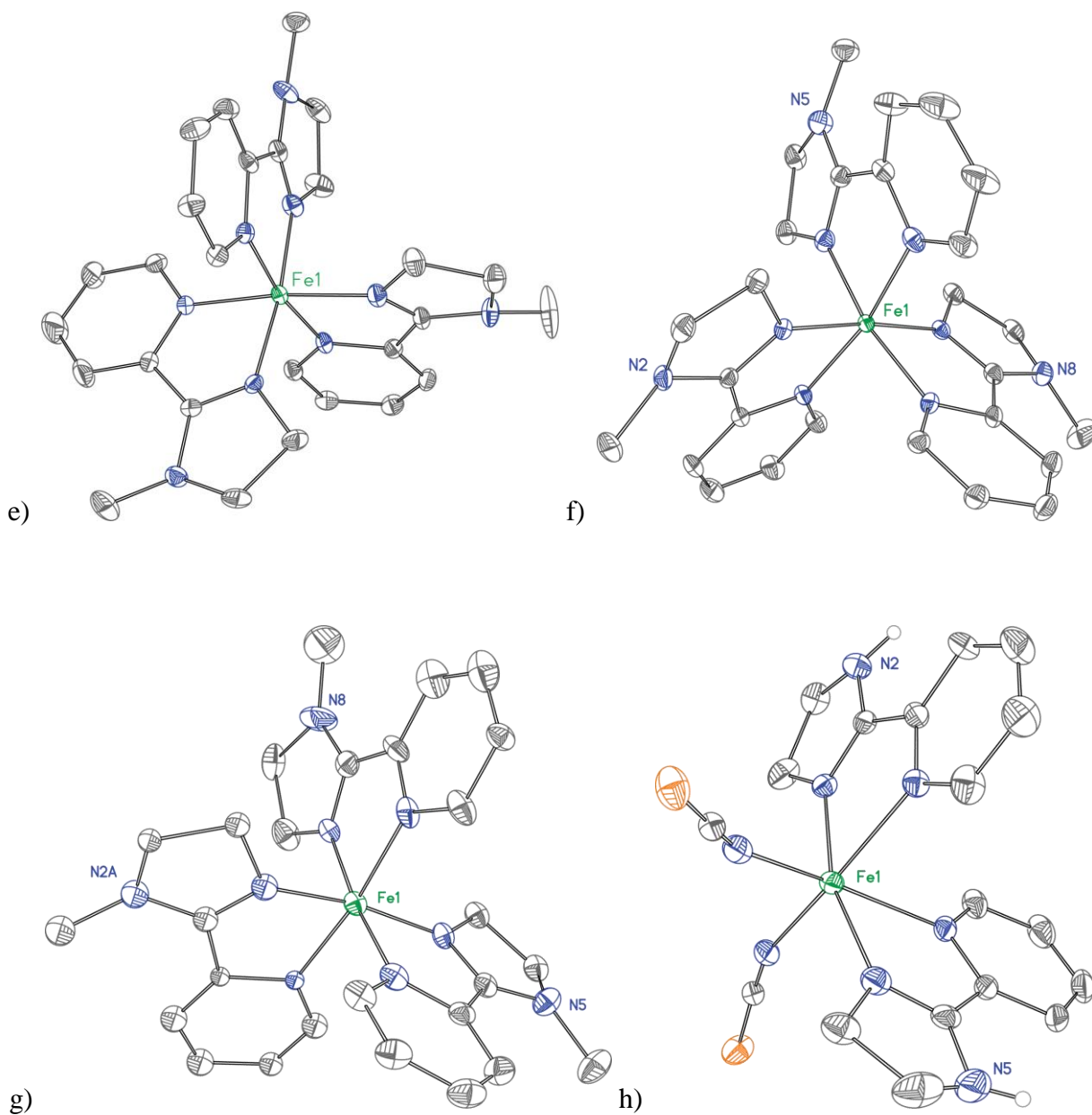
Figure 3.5 continued. The crystal structures of **e)** Fe(pizMe)$_3$Br$_2$ (**3.5**), **f)** [Fe(pizMe)$_3$](FeCl$_4$) (**3.6**), **g)** Fe(pizMe)$_3$(BPh$_4$)$_2$ (**3.7**), and **h)** [Fe(pizH)$_2$(NCS)$_2$] (**3.8**). Non-labeled grey atoms are carbon and hydrogen atoms have been omitted for clarity. Atoms are rendered at the 40% probability level.

Table 3.2. Selected bond distances (Å) and distortion parameters (°) for **3.1**, **3.4** and **3.8** and the cations in **3.2**, **3.3**, **3.5**, and **3.7**.[a]

	avg. Fe–N$_{pizR}$ [b]	Σ	Θ
3.2	1.969(9)	62.0(7)	144.8
3.3	1.96(2)	60.9(9)	150.4
3.5	1.954(7)	61.1(3)	142.9
3.6	1.965(4)	64.2(3)	166.2
3.7	1.95(3)	66(1)	154.0
	avg. Fe–N$_{pizR}$ [b]	avg. Fe–Cl	
3.1	2.175(2)	2.4822(6)	
3.4	2.134(2)	2.404(1)	
	avg. Fe–N$_{pizR}$ [b]	avg. Fe–NCS	
3.8	2.192(6)	2.119(6)	

[a] For determinations of Σ and Θ, see reference 18.
[b] Average value for all Fe–N distances in the structure.

Excluding the weak-field Cl- or NCS-containing complexes **3.1**, **3.4**, and **3.8**, the average Fe–N$_{pizR}$ bond lengths are the same in **3.2**, **3.3**, **3.5**, **3.6**, and **3.7** (Table 3.2) mirroring our previous observation that the ligand field strengths imparted by pizH and pizMe are similar. We addressed this topic in more detail in Chapter 2: the ligand field imparted by pizMe is stronger, which is visible at room temperature, however, low temperature solid state structures are reflective of the low-spin species. In each homoleptic complex, the bond lengths correspond to what is expected for low-spin species or mixed-spin states. Moreover, Σ and Θ are similar for all of the $[Fe(pizR)_3]^{2+}$ cations indicating a similar amount of distortion resulting from the low-spin state. Similar results are observed for SQUID measurements obtained on crystalline samples: **3.4** shows two high spin Fe(II) centers with weak ferromagnetic coupling while **3.6** shows susceptibility due to the high spin $(FeCl_4)^{2-}$ anion but little contribution is observed from the octahedral pizMe-containing cation.

Table 3.3. Selected intermolecular bond distances (Å) and angles (°).

[Fe(pizH)₂Cl₂] (3.1)			
N5···Cl2	3.235(1)	∠N5–H5a ···Cl2	172(2)
N2···Cl1	3.222(2)	∠N2–H2a ···Cl1	95.8(1)
O1···Cl2	3.200(2)	∠C17–O1 ···Cl2	175(2)
[Fe(pizH)₃Br₂] (3.2)			
N5···Br2	3.501(5)	∠N5–H5b···Br1	155(6)
N2···Br2	3.505(6)	∠N2–H2b···Br2	160(7)
N8···Br1	3.359(5)	∠N8–H8c···Br2	134(7)
[Fe(pizH)₃(BPh₄)₂] (3.3)			
N5···π	3.199		
N2···π	3.149		
N8a···π	3.298		
N8b···π	4.118		
[Fe(pizMe)Cl₂]₂ (3.4)			
Iz(N4)···Iz(N4')	4.149		
Py(N6)···Iz(N4')	4.029		
Py(N6)···Py(N6')	4.197		
Py(N3)···Py(N3')	4.046		
Py(N3)···Iz(N1')	4.152		
[Fe(pizMe)₃](FeCl₄) (3.6)			
Iz(N1)···Iz(N7')	3.924		
[Fe(pizH)₂(NCS)₂] (3.8)			
N8···S2	3.385(3)	∠N8–H8b···S2	146(4)
N5···S3	3.391(3)	∠N5–H5a···S3	145(4)
N11···S1	3.564(3)	∠N11–H11a···S1	176(3)
N2···S4	3.561(3)	∠N2–H2a···S4	174(3)
Iz(N1)···Py(N9)	3.722		
Iz(N7)···Py(N3)	3.938		
Iz(N10)···Py(N6)	3.717		
Iz(N4)···Py(N12)	3.931		

Intermolecular pizR-structural correlations

The pizH/halide-containing complexes display hydrogen bonds between the pizH N–H moiety and a nearby anion; either a Cl⁻ ligand (**3.1**) or a Br⁻ charge-balancing anion (**3.2**). The complex in **3.1** shows three hydrogen bonds in the solid state: two between pizH–Cl and one

incorporating a co-crystallized methanol between CH_3OH–Cl (Table 3.3). Complex **3.2** shows hydrogen bonds between N–H···Br, though all slightly bent relative to the hydrogen bonds in **3.1**. The N···Br distances are longer than the N···Cl distances in accordance with the larger anion size.

There are no direct interactions between pizMe and Cl⁻ in **3.4** and **3.6**; however, there are examples of π-π stacking. In **3.4**, separations between pyridine (Py) or imidazoline (Iz) rings are > 4 Å, similar to those observed in the literature (Table 3.3).[19] In this case, intermolecular ligands are oriented almost parallel to each other: however, because the interactions are more than 0.6 Å longer than the ideal separation (3.4 Å in graphite and porphyrin[20]), the π-π overlap is likely weak and imparts at most a minor effect on spin state. In **3.6**, π-π stacking separations are ~3.9 Å, but the ligands are nonplanar and intermolecular ligands deviate slightly from a parallel arrangement, which likely weakens π-π overlap. Like **3.4**, the effect of intermolecular interactions on spin state is likely insignificant. As expected, these complexes demonstrate few cation-anion interactions involving the pizMe ligand. Unlike these complexes, pizMe-containing **3.5** shows no intermolecular cation–anion interactions other than close contacts through packing via van der Waals forces.

The BPh_4-containing complexes **3.3** and **3.7** show different intermolecular interactions as predicted. Cation–anion interactions for **3.3** include N–H···π contacts comparable with what has been reported previously. These distances are shortest/strongest for the two full occupancy pizH ligands in the structure, while the ligand with positional disorder shows interactions longer by ~0.1 Å for one N–H···π contact and ~1 Å for another N–H···π contact. It is possible that packing forces encourage ligands to not be disordered when intermolecular contacts are available. When intermolecular contacts are not available (or are longer than is typical) ligand disorder occurs. On the other hand, contacts in **3.7** only employ van der Waals forces as there are no available hydrogen

bonding sites. There are no interactions that show preference for specific atoms or that indicate significant cation–anion interactions. Moreover, unlike **3.4**, there are no π–π interactions. We propose that the bulky nature of the BPh4⁻ anions prevents beneficial overlap in the crystal packing.

The most unique intermolecular interactions are in the structure of **3.8**, which shows both hydrogen bonds *and* π–π stacking. N–H···S contacts are observed between each pizH ligand and an NCS⁻ ligand on a neighboring molecule. These contacts are intermediate in length between the N–H···Cl contacts in **3.1** and the N–H···Br contacts in **3.2** and two are nearly linear while two are slightly bent. Because these hydrogen atoms are found based on residual electron density, the hydrogen bond distance and angle inform us about the strength of the interaction. Meanwhile, the π–π stacking contacts are shorter than those observed for **3.4** or **3.6**: two are similar in length and two are longer (~0.2 Å) than those observed in graphite or porphyrin.[20] The shorter π–π stacking distances allow for the π–π overlap that can stabilize the complex, though we still predict a weak effect on the spin state.

Intramolecular pizR-structural correlations

An unexpected correlation between pizR geometry and solid-state spin state was additionally observed. The R-substituted nitrogen atom (N_R) on the imidazoline ring is capable of two possible configurations: a planar amide-like geometry such that the lone pair is delocalized into the imidazoline ring or a pyramidal amine-like geometry such that the lone pair is localized on the nitrogen atom. For pizMe-containing complexes **3.4** and **3.6**, a distinct difference was observed in the structure. The high-spin complex **3.4** showed a nearly planar imidazoline nitrogen, with the sum of angles around N_R falling in the range 259.6–360.0° and the CH_3 moiety deviation

from the imidazoline mean plane falling in the range 0.149–0.232 Å. For an sp^2 atom, we would expect the sum of the angles around that atom to be 360° and for an sp^3 atom, we expect the sum of angles to be ~330°. On the other hand, the mostly low spin (at 120 K) **3.6** showed pyramidal imidazoline nitrogen atoms with the sum of angles in the range of 347.3–355.4° and the distance between CH_3 and the imidazoline plane in the range of 0.200–0.513 Å. Compounds **3.5** and **3.7** also show slightly pyramidalized imidazoline nitrogen atoms to accompany the low-spin state (Table 3.4).

The pizH-containing complexes were initially refined with all hydrogen atoms placed at idealized positions, but to compare with the pizMe complexes, final structures have hydrogen atoms bound to the imidazoline nitrogen that were located by investigating the residual electron density. These atoms are allowed to refine *x*, *y* and *z* coordinates with thermal parameters based on the nitrogen to which they are bound. Despite the high estimated standard deviations of angles associated with hydrogen atoms located in this way (Table 3.4), a similar trend is observed. The weak-field ligands NCS⁻ and Cl⁻ result in high spin complexes, which have planar (**3.1**) or nearly planar (**3.8**) imidazoline nitrogen atoms with the sum of angles close to 360° and slight deviations of the hydrogen atom from the imidazoline mean plane. Complexes **3.2** and **3.3,** on the other hand, are low spin and exhibit sums of angles <360° and greater deviations of the H-atom from the imidazoline ring.

Figure 3.6. Overlay of the pizH imidazoline moieties in **3.1** (blue) and **3.3** (red) on the left and pizMe imidazoline moieties in **3.4** (blue) and **3.6** (red) on the right.

Table 3.4. pizR ligand pyramidalization measurements: sum of angles (°), deviation of R from the mean plane of the imidazoline ring (Å) and carbon–nitrogen distances in the imidazoline ring (Å). (C–N distances are highlighted in pairs by ring.).

[Fe(pizH)$_2$Cl$_2$] (3.1)								
sum of angles around N$_R$ (°)	N2	359(1)	*H···Imz(plane) distance* (Å)	H2a	0.127	*Imz(C–N) distance*	N1–C3	1.300(2)
	N5	359(1)		H5a	0.091		C3–N2	1.337(2)
							N4–C11	1.300(2)
							C11–N5	1.338(2)
[Fe(pizH)$_3$]Br$_2$ (3.2)								
sum of angles around N$_R$ (°)	N2	359(6)	*H···Imz(plane) distance* (Å)	H2b	0.183	*Imz(C–N) distance*	N3–C6	1.282(6)
	N5	353(6)		H5b	0.227		C6–N2	1.342()
	N8	337(6)		H8c	0.349		N6–C14	1.297(6)
							C14–N5	1.343(8)
							N9–C22	1.274(6)
							C22–N8	1.351(8)
[Fe(pizH)$_3$](BPh$_4$)$_2$ (3.3)[a]								
sum of angles around N$_R$ (°)	N2	348(3)	*H···Imz(plane) distance* (Å)	H2c	0.350	*Imz(C–N) distances*	N1–C3	1.293(5)
	N5	337(3)		H5b	0.356		C3–N2	1.366(4)
							N4–C11	1.295(5)
							C11–N5	1.352(5)
							N7a–C19a	1.32(2)
							C19a–N8a	1.39(2)
							N8b–C19b	1.42(3)
							C19b–N7b	1.28(2)
[Fe(pizMe)$_2$Cl]$_2$ (3.4)								
sum of angles around N$_R$ (°)	N2	360.0(2)	*CH$_3$···Imz(plane) distance* (Å)	C3	0.232	*Imz(C–N) distances*	N4–C13	1.309(2)
	N5	359.6(2)		C12	0.149		C13–N5	1.338(2)
							N1–C4	1.302(2)
							C4–N2	1.345(2)

[a] The sum of bond angles and H···Imz(plane) distances are shown for only two N$_R$ atoms. The third ligand is disordered, so the positions of hydrogen atoms attached to N8a and N8b were calculated rather than found based on electron density. Therefore, structural parameters are less meaningful.

Table 3.4 continued. pizR ligand pyramidalization measurements: sum of angles (°), deviation of R from the mean plane of the imidazoline ring (Å) and carbon–nitrogen distances in the imidazoline ring (Å) (C–N distances are highlighted in pairs by ring.)

[Fe(pizMe)₃]Br₂ (3.5)								
sum of angles around N_R *(°)*	N2	353.1(5)	*CH₃···Imz(plane) distance* (Å)	C29	0.419	*Imz(C–N) distances*	N1–C30	1.296(5)
	N5	348.8(5)		C42	0.414		C30–N2	1.365(5)
	N8a	356(1)		C47a	0.470		N4–C41	1.299(4)
	N8b	360 (8)		C47b	0.066		C41–N5	1.366(4)
							N7–C48	1.375(8)
							C48–N8a	1.375(8)
							N7–C48	1.375(8)
							N8b–C48	1.30(4)
[Fe(pizMe)₃]FeCl₄ (3.6)								
sum of angles around N_R *(°)*	N2	347.3(4)	*CH₃···Imz(plane) distance* (Å)	C3	0.410	*Imz(C–N) distances*	N1–C4	1.300(3)
	N5	355.4(4)		C12	0.200		C4–N2	1.366(3)
	N8	347.4(4)		C21	0.513		N4–C13	1.289(3)
							C13–N5	1.365(3)
							N7–C22	1.297(3)
							C22–N8	1.370(3)
[Fe(pizMe)₃](BPh₄)₂ (3.7)								
sum of angles around N_R *(°)*	N2a	354(1)	*CH₃···Imz(plane) distance* (Å)	C3a	0.185	*Imz(C–N) distances*	N1a–C4a	1.30(1)
	N2b	356(2)		C3b	0.080		C4a–N2a	1.33(1)
	N5	359.7(5)		C12	0.206		N1b–C4b	1.13(3)
	N8	354.0(3)		C21	0.011		C4b–N2b	1.38(3)
							N4–C13	1.306(3)
							C13–N5	1.360(4)
							N7–C22	1.305(3)
							C22–N8	1.390(4)
[Fe(pizH)₂(NCS)₂] (3.8)								
sum of angles around N_R *(°)*	N2	350(3)	*H···Imz(plane) distance* (Å)	H2a	0.226	*Imz(C–N) distances*	N1–C3	1.297(3)
	N5	351(4)		H5a	0.126		C3–N2	1.354(4)
	N8	351(4)		H8b	0.121		N4–C11	1.293(4)
	N11	351(3)		H11a	0.218		C11–N5	1.350(4)
							N7–C19	1.290(4)
							C19–N8	1.349(4)
							N10–C27	1.299(3)
							C27–N11	1.352(4)

From these structural parameters, we consider the two possible resonance structures of the pizR ligands (Figure 3.7) and the subsequent effect on Fe–L binding. Though the zwitterionic resonance contributor is unlikely to contribute significantly to the isolated molecule, it can play a role in the properties of the coordinated ligand. For the neutral, pyramidalized, ligand (left of Figure 3.7), the bond between the nitrogen bound to iron (N_{Fe}) and carbon should be significantly shorter than the bond between the R-substituted nitrogen (N_R) and carbon. On the other hand, the delocalized resonance contributor (center of Figure 3.7) would be expected to have equal bond lengths, while the zwitterionic contributor (right of Figure 3.7) would have inverted relative bond lengths, with $N_R < N_{Fe}$. The crystallographic data for all complexes have $N_R > N_{Fe}$, indicating the neutral ligand contribution is, as expected, most significant. With the exceptions of **3.7** and **3.8**, the difference between N_R and N_{Fe} for the low-spin species is ~0.06 Å, while the difference for the high-spin species is slightly shorter at ~0.03 Å. This difference is small, but significant, suggesting at least a small contribution from the delocalized, zwitterionic version of the ligand.
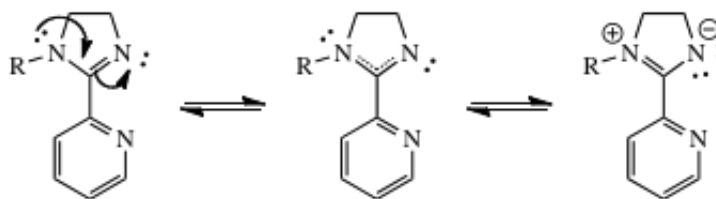
Figure 3.7. Resonance structures of the pizR ligands.

We attempt to rationalize this difference based on electronic properties: the zwitterionic resonance contributor with a negative charge adjacent to the iron center likely limits the amount of π-backbonding that is available from the Fe(II) center to the ligand, engendering the ligand with a weaker ligand field. The unconjugated, pyramidalized version of the ligand, however, would be predicted to have an orbital available for backbonding from the Fe(II) center, similarly to a CN⁻ ligand, which would result in a stronger ligand field. It is possible that the presence of another

weak-field ligand in **3.1**, **3.4**, and **3.8** directs the pizR ligands to adopt a ligand conformation that provides a similar field strength.

3.5 Conclusion

In conclusion, we observed a relationship between ligand structural parameters and spin-state within a Fe(II) complex. When Fe(II) is in a low-spin state due to anion hydrogen bonding interactions or pizR ligand field strength, the pizR ligand adopts a more planar geometry suggesting some amide-like properties of the imidazoline ring. On the contrary, when a weak-field ligand induces a high-spin state of the Fe(II), the pizR ligand adopts an envelope conformation with a pyramidalized nitrogen and little to no amide-like properties of the imidazoline ring. This is a novel case of a long-range structural change based on the electronic environment of the metal center.

3.6 Acknowledgments

CHAPTER 3 REFERENCES

1. Ni, Z.; McDaniel, A. M.; Shores, M. P., *Chem. Sci.* 2010, *1*, 615-621.
2. Ni, Z.; Shores, M. P., *Inorg. Chem.* 2010, *49*, 10727-10735.
3. Ni, Z.; Fiedler, S. R.; Shores, M. P., *Dalton Trans.* 2011, *40*, 944-950.
4. Leita, B. A.; Moubaraki, B.; Murray, K. S.; Smith, J. P., *Polyhedron* 2005, *24*, 2165-2172.
5. Matouzenko, G. S.; Molnar, G.; Bréfuel, N.; Perrin, M.; Bousseksou, A.; Borshch, S. A., *Chem. Mat.* 2002, *15*, 550-556.
6. Matouzenko, G. S.; Perrin, M.; Le Guennic, B.; Genre, C.; Molnar, G.; Bousseksou, A.; Borshch, S. A., *Dalton Trans.* 2007, 934-942.
7. Wu, A.; Masland, J.; Swartz, R. D.; Kaminsky, W.; Mayer, J. M., *Inorg. Chem.* 2007, *46*, 11190-11201.
8. Schulte, K. A. B.S. Thesis: The Preparation of Iron (II) Complexes with pizH and pizMe to Probe the Effects of Hydrogen Bonding on Spin Crossover. Colorado State University, Fort Collins, 2013.
9. Ishihara, M.; Togo, H., *Tetrahedron* 2007, *63*, 1474-1480.
10. Fiedler, S. R. PhD Thesis: A Study of Magnetostructural Parameters Related to Spin Crossover and Single Molecule Magnetism. Colorado State University, Fort Collins, 2013.
11. Evans, D. F., *J. Chem. Soc.* 1959, 2003-2005.
12. Yaws, C. L., *Thermodynamic and Physical Property Data*. Gulf Publishing Co.: Houston, 1992; p 6.
13. *APEX 2*. Bruker Analytical X-Ray Systems, Inc: Madison, WI, 2008.
14. Sheldrick, G. M. *SHELXTL*, Version 6.14; Bruker Analytical X-Ray Systems, Inc.: Madison, WI, 1999.
15. Ni, Z.; Shores, M. P., *J. Am. Chem. Soc.* 2009, *131*, 32-33.
16. Busch, D. H.; Bailar, J. C., *J. Am. Chem. Soc.* 1956, *78*, 1137-1142.
17. Goodwin, H. A., *Top. Curr. Chem.* 2004, *233*, 59-90.
18. Halcrow, M. A., *Chem. Soc. Rev.* 2011, *40*, 4119-4142.
19. Hostettler, M.; Toernroos, K. W.; Chernyshov, D.; Vangdal, B.; Buergi, H.-B., *Angew. Chem. Int. Ed.* 2004, *43*, 4589-4594.
20. Hunter, C. A.; Sanders, J. K. M., *J. Am. Chem. Soc.* 1990, *112*, 5525-5534.

CHAPTER 4: ANTIFERROMAGNETIC COUPLING ACROSS TETRAMETALLIC UNITS THROUGH NON-COVALENT INTERACTIONS

4.1 Introduction

It has long been a goal of synthetic chemistry to prepare materials in which rational control can be exerted over resulting electronic and magnetic properties. The manipulation of magnetic spins has been widely explored in the context of data storage,[1] and molecular imaging through MR contrast agents.[2] Linda Doerrer's group at Boston University is interested in the magnetic properties of extended metal atom chain (EMAC) systems with strong coupling between paramagnetic centers.[3-4] Metal-metal interactions can be formed via the phenomenon of metallophilicity,[5-7] in which non-covalent M–M interactions can form between closed shell and closed subshell metal centers affording the widely observed d^{10}–d^{10}, d^{10}–d^8, and d^8–d^8 combinations.[8] Square-planar or linear coordination geometries are typical for these interactions, and the metal complexes containing them are obvious candidates for highly anisotropic assemblies of metal atoms.[9]
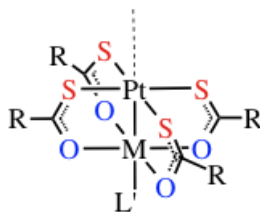
Figure 4.1. A bimetallic lantern complex where R = CH$_3$ (ligand: SAc) or C$_6$H$_5$ (ligand: tba).

One branch of these compounds are the heterobimetallic lantern-type (a.k.a. paddlewheel) complexes,[10-12] however, few lantern complexes of the form [PtM(L$_4$X$_4$)] with *3d* metals exist and none show Pt···Pt metallophilic interactions in the solid state. Previously reported lantern structures with thiobenzoate or thioacetate are also uncommon, consisting of only the

homobimetallic complexes.[13-16] Therefore, we became interested in understanding the magnetic exchange in these complexes using a "building up" strategy, by first considering isolated bimetallic lanterns, which can inform our understanding of "dimeric" tetranuclear complexes and subsequently the extended chains. From the geometrical anisotropy of these systems we envisage the possibility of co-axial magnetic anisotropy. Considering the molecules through the "building up" thought process could help us understand how molecular anisotropy manifests in an extended network.

Herein we report the magnetic characterization of a series of heterobimetallic lantern complexes using tba (thiobenzoate) or SAc (thioacetate) ligands with the forms $[(PtM(SAc)_4(py)_2]$ (M = Co(II) (**4.1**) or Ni(II) (**4.2**)); $[PtM(tba)_4(OH_2)]$ (M = Fe(II) (**4.3**), Co(II) (**4.4** and **4.11**), Ni(II) (**4.12**)); $[PtM(SAc)_4(L')]$ (M = Co(II); L' = OH_2 (**4.13**), 3-nitropyridine (3-NO_2py, **4.15**), open coordination site (**4.21**), pyridine (py, **4.5**), aminopyridine (amp, **4.7**), dimethylsulfoxide (DMSO, **4.9**), and M = Ni(II); L' = OH_2 (**4.14**), 3-NO_2py (**4.16**), open coordination site (**4.22**), py (**4.6**), amp (**4.8**), or dimethylformamide (DMF, **4.10**)), $[PtM(SAc)_4(pyz)]_\infty$ (pyz = pyrazine, M = Co(II) (**4.17**) or Ni(II) (**4.18**)) and $[PtM(SAc)_4(pyz)_{0.5}]_2$ (M = Co(II) (**4.19**) or Ni(II) (**4.20**)). These complexes incorporate high spin $3d^n$ M(II) and low spin $5d^8$ Pt(II) centers and some exhibit short Pt···Pt contacts in the solid state with antiferromagentic exchange between two $3d$ metals occurring through the unbridged Pt···Pt interaction. These complexes exhibit geometries ranging from isolated lantern complexes to dimeric species and extended network 1D chains.

4.2 Division of Labor

Synthesis and non-magnetic characterization for all compounds in this chapter were performed by Frederick G. Baddour and Eric W. Dahl at Boston University.[17-20] Preliminary

magnetic characterization of **4.3**, **4.4**, **4.11**, and **4.12** was performed by Wesley A. Hoffert.[20] Magnetic data collection via SQUID of **4.1, 4.2, 4.5–4.10**, and **4.17–4.20** was performed by Frederick G. Baddour.[17-18] Final magnetic characterization of **4.3**, **4.4**, **4.11–4.16**, **4.21**, and **4.22** and all data fitting and analysis were performed by Stephanie R. Fiedler. Details of complexes **4.3**, **4.4**, **4.11**, and **4.12**[20] and **4.13–4.16**, **4.21**, and **4.22**[19] were previously reported in the literature, while **4.1**, **4.2**, **4.5–4.10** have been submitted[18] and **4.17–4.20** are reported by F. G. Baddour.[17]

4.3 Experimental

Synthesis, NMR, EA, x-ray crystallography, diffuse reflectance measurements and DFT calculations have been previously reported for **4.3**, **4.4**, **4.11**, and **4.12**[20] and **4.13–4.16**, **4.21**, and **4.22**.[19] Synthesis, NMR, EA, x-ray crystallography, thermogravimetric analysis, UV-visible spectrophotometry and magnetic measurements of **4.1–4.22** have been reported by F. G. Baddour.[17]

Magnetic Measurements. Magnetic susceptibility data were collected at Colorado State University with a Quantum Design MPMS-XL SQUID magnetometer in the temperature range 2-300 K at an applied field of 1000 Oe. For measurement, samples were loaded into a gelatin capsule and inserted into drinking straws prior to analysis. Samples measured by F. G. Baddour at Boston University were collected with Quantum Design MPMS-XL (**4.1**, **4.5**, **4.7**, and **4.9**) and Quantum Design MPMS-5S (**4.2**, **4.6**, **4.8**, and **4.10**) SQUID magnetometers in the temperature range 2–300 K at an applied field of 1000 Oe.

Samples of **4.3** were measured as loosely-packed crystals as well as packed ground-up powders. The latter preparations show loss of solvate acetone, and data were interpreted accordingly. Since the dimeric compound **4.11** decomposes upon grinding, a sample of purple

crystalline blocks was left unground, and was measured as loosely-packed crystals and as crystals suspended in a matrix of eicosane to prevent torquing. Data for **4.4** were collected on light-yellow-colored powdered samples. Samples of **4.12** were measured in several different ways: as loosely-packed crystals, as crystals suspended in eicosane, as packed ground-up powders, and as powders suspended in eicosane. The first three preparations provide qualitatively similar data. However, ground samples of **4.12** mixed with eicosane gave significantly different data and powder XRD measurements did not match predicted patterns, so data from this preparation was not analyzed further.

Due to potential sensitivity to desolvation in compounds **4.13**, **4.14**, **4.15**, **4.16**, **4.21**, and **4.22**,[19] microcrystalline samples were used as-prepared: they were not subjected to further grinding or encasement in a polymer matrix. The as-prepared powder samples were loaded into gelatin capsules, inserted into straws, and tapped to pack the solid in place. The absence of ferromagnetic impurities was confirmed for **4.13**, **4.14**, **4.15**, **4.16**, **4.21**, and **4.22** by observing a linear relationship between magnetization and applied field (0.1-5 T) at 125 K. Microcrystalline samples of **4.1**, **4.2**, **4.5–4.10**, and **4.17–4.20** were used as prepared without encasement in a polymer matrix. The samples were loaded into a sample pouch made from a small section of a drinking straw and sealed on both ends with an impulse sealer. The sealed pouch was inserted into a drinking straw as a sample holder and measured.

For all measurements, diamagnetic corrections were applied by using Pascal's constants[21] and by subtracting the diamagnetic susceptibility from the sample holder (including eicosane where appropriate). Where possible, susceptibility data were fit with theoretical models using a relative error minimization routine (julX 1.41).[22] When appropriate, refinements included a

correction for temperature independent paramagnetism (TIP) and intermolecular interactions (through a mean field approximation defined by julX as the parameter θ).

Zero-field splitting parameters obtained with julX for monomeric species are based on the spin Hamiltonian in Equation 4.1, where D and E are the axial and rhombic zero-field splitting parameters, respectively, of each spin center, S is the local spin multiplicity of each spin center, B is the magnetic field vector and g is the isotropic average of the g value for each spin center.

$$\hat{H} = \sum D_i \left[S_{z,i}^2 - \tfrac{1}{3} S_i (S_i + 1) + E_i / D_i \left(S_{x,i}^2 - S_{y,i}^2 \right) \right] + \sum g \beta \vec{S}_i \cdot \vec{B} \tag{4.1}$$

Exchange coupling parameters for dimer species are based on the Hamiltonian in Equation 4.2, where J_{12} is the exchange coupling constant between the first and second spin center.

$$\hat{H} = -2 J_{12} (\hat{S}_1 \cdot \hat{S}_2) \tag{4.2}$$

Fits of magnetization data were obtained with the ANISOFIT program[23] and are based on the Hamiltonian in Equation 4.3, where D, E, g, S, and B have the same definitions as in Equation 4.1.

$$\hat{H} = D\hat{S}_z^2 + E \left(\hat{S}_x^2 + \hat{S}_y^2 \right) + g_{iso} \mu_B \mathbf{S} \cdot \mathbf{B} \tag{4.3}$$

The MagSaki program[24] was used to simulate magnetic susceptibility data involving axially distorted Co(II)-containing compounds according to the Hamiltonian shown in Equation 4.4, where λ is the spin-orbit coupling parameter, Δ is the axial ligand-field splitting parameter, and κ is an orbital reduction factor.

$$H = \Delta \left(L_z^2 - \tfrac{2}{3} \right) - \left(\tfrac{3}{2} \right) \kappa \lambda \mathbf{L} \cdot \mathbf{S} + \beta \left[\left(-\tfrac{3}{2} \right) \kappa \mathbf{L} + g_e \mathbf{S} \right] \tag{4.4}$$

We attempted to model extended chains as rings using julX as well using the Hamiltonian in Equation 4.5, where S is the spin multiplicity of each spin center and b is an integer from 2 to the number of spin centers and $a = b - 1$; J_{ab} is the intramolecular coupling constant between

adjacent spin centers *a* and *b*: a "ring"-closing coupling constant was included in the form of J_{1b}.

$$\hat{H} = -2J_{ab}(\hat{S}_a \cdot \hat{S}_b)$$

(4.5)

4.4 Results

Syntheses

As shown in Scheme 4.2, the combination of sodium thiocarboxylate with $K_2PtCl_4(aq)$ and then a first-row transition metal chloride hydrate yields $[PtM(tba)_4(OH_2)]$ (M = Fe(II), **4.3**; Co(II), **4.11** or **4.4**; Ni(II), **4.12**)[20] or $[PtM(SAc)_4(OH_2)]$ (M = Co(II), **4.13**; Ni(II), **4.14**). Compounds **4.13** and **4.14** undergo axial ligand exchange upon reaction with 3-NO_2py to yield $[PtM(SAc)_4(3-NO_2py)]$ (M = Co(II), **4.15**; Ni(II), **4.16**).[19] Alternatively, **4.13** and **4.14** could be converted into the insoluble powders $[PtM(SAc)_4]$ (M = Co(II), **4.21**; Ni(II), **4.22**) if dried under vacuum. Subsequent axial ligand substitution of **4.21** and **4.22** yields the complexes $[PtM(SAc)_4(py)_2]$ (M = Co(II), **4.1**; Ni(II), **4.2**) or $[PtM(SAc)_4(L')]$ (M = Co(II); L' = py (**4.5**), aminopyridine (amp) (**4.7**) or DMSO (**4.9**) and M = Ni(II); L' = py (**4.6**), amp (**4.8**), or DMF (**4.10**)).[17-18] Reaction of the aquo complexes **4.13** and **4.14** with pyrazine can yield the 1D chain $[PtM(SAc)_4(pyz)]_\infty$ (M = Co(II) (**4.17**) or Ni(II) (**4.18**)) and a bridged dimer $[PtM(SAc)_4(pyz)_{0.5}]_2$ (M = Co(II) (**4.19**) or Ni(II) (**4.20**)).[17]

Structural Characterization

Results of single crystal X-ray diffraction studies are summarized in Table 4.1 and are important for considering our "building up" comparison process. Crystals of **4.1** and **4.2** reveal capped monomers, where Pt–N_{py} bonding prevents any Pt···Pt interaction. Crystals of **4.3** and yellow crystals of **4.4**, grown from CH_2Cl_2, reveal an offset-dimer lantern structure, with short Pt–S contacts, but which display no direct Pt···Pt bonding interaction. Likewise, the structures of **4.5**–

4.10 show only offset dimer Pt–S interactions. In contrast, purple crystals of **4.11** grown from THF unveil a dimeric (tetranuclear) structure. The structures of **4.12**–**4.16** also exist as dimers of lanterns in the solid state. Meanwhile, compounds **4.17** and **4.18** are connected via a pyrazine ligand utilizing both M–N_{pyz} and Pt–N_{pyz} bonds to form an infinite chain. Compounds **4.19** and **4.20**, on the other hand, make use of a pyz ligand to bridge two lanterns through M–N_{pyz} bonds. Each bridged dimer is arranged in an offset Pt–Pt arrangement with another bridged dimer. Structures of complexes **4.21** and **4.22** have not yet been obtained.
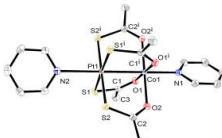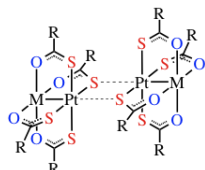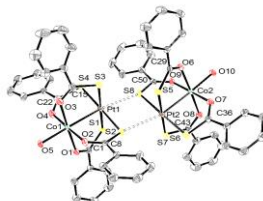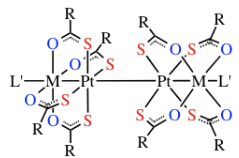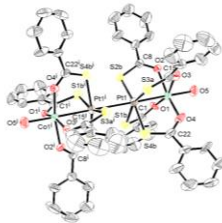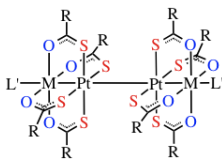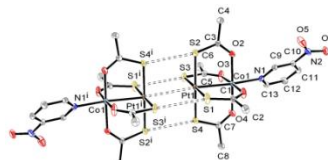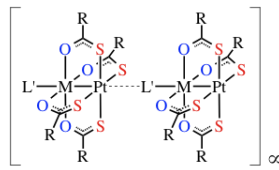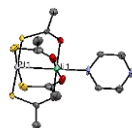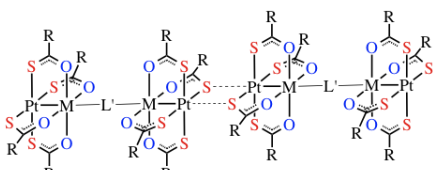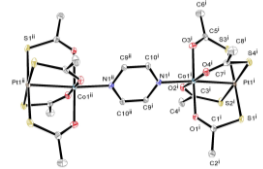
Solution Susceptibility

The Evans' method[25] solution phase susceptibility values of 5.18 (**4.1**), 3.15 (**4.2**), 5.11 (**4.3**), 5.02 (**4.4**), 3.11 (**4.12**), 4.93 (**4.13**), 2.84 (**4.14**), 5.06 (**4.15**), 3.05 μ_B (**4.16**), 4.61 (**4.5**), 3.09 (**4.6**), 4.87 (**4.7**), 2.97 (**4.8**), 5.01 μ_B (**4.9**), and 3.03 μ_B (**4.10**), are all consistent with high spin first-row transition metal centers as expected from the oxygen carboxylate donors and pseudo-octahedral coordination geometry. These values indicate that regardless of solid-state long-range organization, in solution each compound is behaving as a single monomeric {MPt} species.
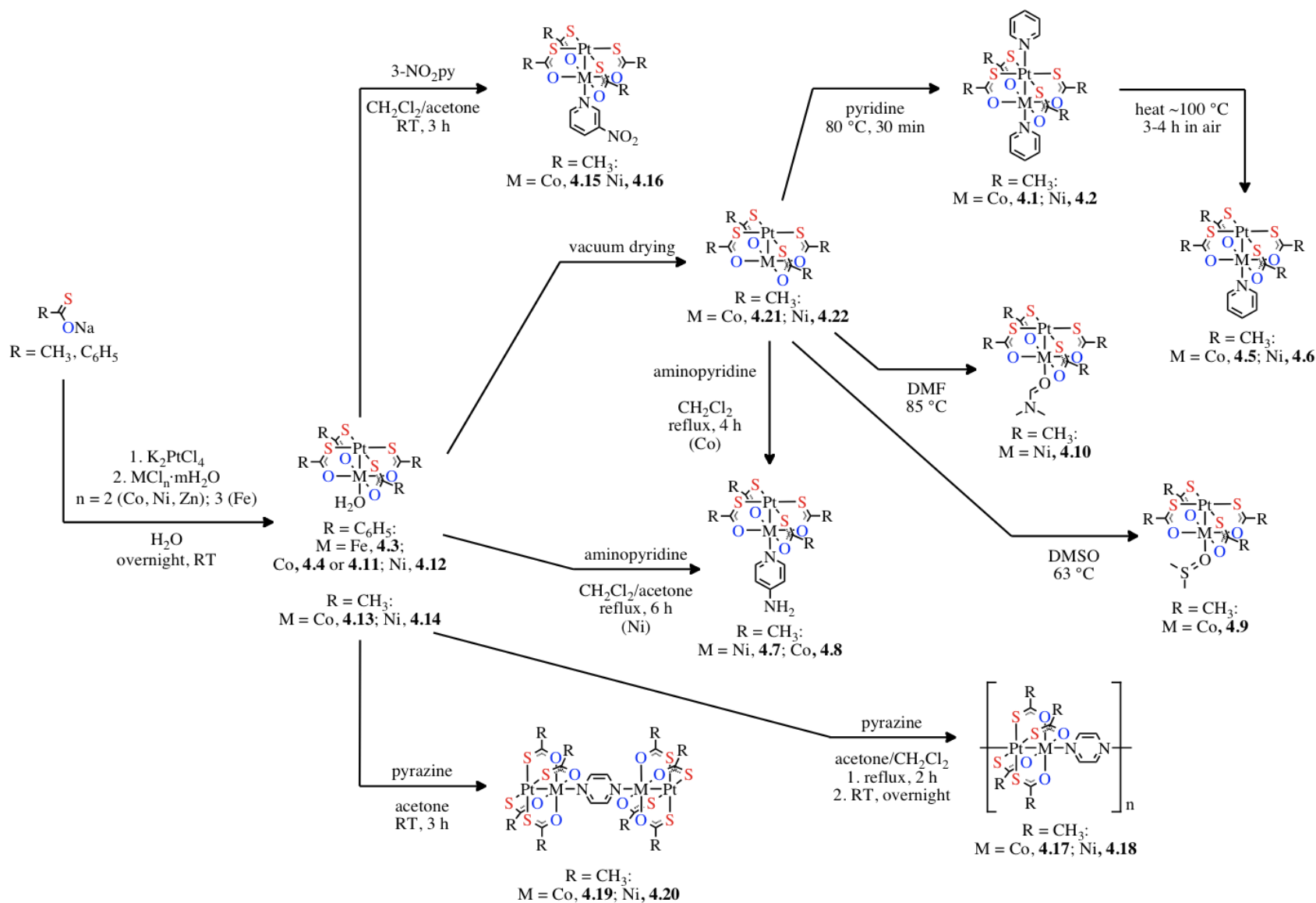
Figure 4.2. Synthesis of compounds described herein.

Table 4.1. Summary of the structure types described herein.

Structure Type	Example	Fe(II) center (R)	Co(II) center (R)	Ni(II) center (R)
non-bonded	[PtCo(SAc)$_4$(py)$_2$], **4.1**		**4.1** (CH$_3$)	**4.2** (CH$_3$)
offset non-bonded	[PtCo(tba)$_4$(OH$_2$)], **4.4**	**4.3** (C$_6$H$_5$)	**4.4** (C$_6$H$_5$) **4.5, 4.7, 4.9** (CH$_3$)	**4.6, 4.8, 4.10** (CH$_3$)
staggered bonded	[PtCo(tba)$_4$(OH$_2$)], **4.11**		**4.11** (C$_6$H$_5$) **4.13** (CH$_3$)	**4.12** (C$_6$H$_5$) **4.14, 4.16** (CH$_3$)
eclipsed bonded	[PtCo(SAc)$_4$(3-NO$_2$py)]$_2$, **4.15**		**4.15** (CH$_3$)	
infinite chain	[PtNi(SAc)$_4$(pyz)]$_\infty$, **4.18**		**4.17** (CH$_3$)	**4.18** (CH$_3$)
bridged dimer with offset non-bonded interaction	[PtCo(SAc)$_4$(pyz)$_{0.5}$]$_2$, **4.20**		**4.19** (CH$_3$)	**4.20** (CH$_3$)

Magnetic Susceptibility

Non-bonded compounds

The room temperature $\chi_M T$ value for the Co(II) complex **4.1,** 3.24 emu·K·mol^{-1}, is larger than what is expected for a spin-only Co(II) ion, but consistent with what is expected for a Co(II) ion when considering spin-orbit coupling. The room temperature $\chi_M T$ value for the Ni(II) complex **4.2**, 1.40 emu·K·mol^{-1}, is only slightly larger than what is expected for a spin-only Ni(II) ion.
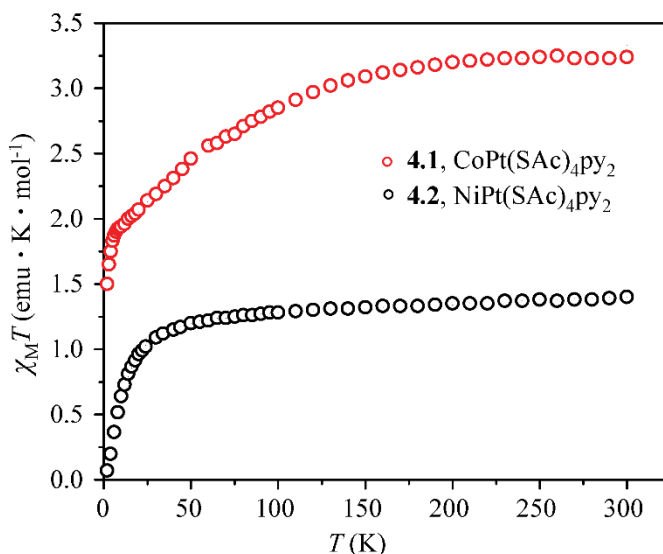
Figure 4.3. Temperature dependence of magnetic susceptibility for Co(II) complex **4.1**, and Ni(II) complex **4.2**.

Offset non-bonded compounds

The solid-state magnetic susceptibility of the Fe(II) complex **4.3** shows behavior consistent with well-isolated, high spin Fe(II) ions. At 295 K, the $\chi_M T$ value for loosely packed crystals is 3.24 emu·K·mol^{-1} ($\mu_{eff} = 5.09\ \mu_B$), which is slightly higher than that expected for a HS Fe(II) with g = 2.0 ($\chi_M T = 3.0$ emu·K·mol^{-1}). As the temperature is lowered, $\chi_M T$ decreases very gradually until 35 K (2.89 emu·K·mol^{-1}), when it begins to rapidly decrease due to zero field splitting.
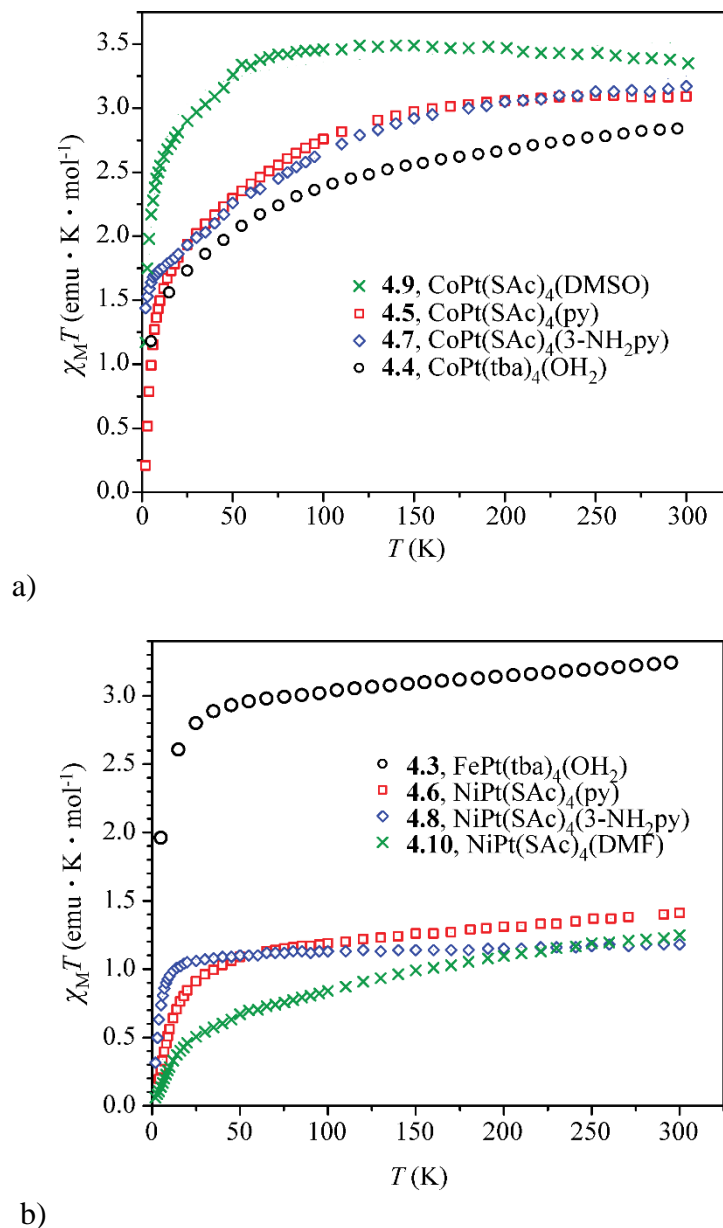
Figure 4.4. a) Temperature dependence of magnetic susceptibility for Co(II) complexes **4.4**, **4.5**, **4.7**, and **4.9**. **b)**Temperature dependence of magnetic susceptibility for the Fe(II) complex **4.3** and Ni(II) complexes **4.6**, **4.8**, and **4.10**.

Complex **4.4** appears to behave similarly to the Fe(II) analogue **4.3**. At room temperature, $\chi_M T$ for this powder is 2.85 emu·K·mol^{-1} (μ_{eff} = 4.77 μ_B). Upon cooling, the susceptibility decreases gradually down to ~85 K, where $\chi_M T$ = 2.31 emu·K·mol^{-1}. Below 80 K, the product drops off more steeply to 1.18 emu·K·mol^{-1} at 5 K. Room temperature values for **4.4** are larger

than expected for a single S = 3/2 ion (1.875 emu·K·mol^{-1}), respectively, but consistent with a significant orbital contribution to the susceptibility, common for Co(II) complexes.

Apical ligand substitution yields compounds with qualitatively similar $\chi_M T$ data to the {MPt} complexes **4.3** and **4.4** (shown in Figure 4.4). The room temperature $\chi_M T$ values for the Co(II) complexes (**4.5**: 3.09 emu·K·mol^{-1}, **4.7**: 3.18 emu·K·mol^{-1}, **4.9**: 3.35 emu·K·mol^{-1}) are larger than what is expected for a spin-only Co(II) ion (1.875 emu·K·mol^{-1}), but consistent with what is expected for a Co(II) ion when considering spin-orbit coupling. The room temperature $\chi_M T$ values for the Ni(II) complexes (**4.6**: 1.41 emu·K·mol^{-1}, **4.8**: 1.18 emu·K·mol^{-1}, **4.10**: 1.25 emu·K·mol^{-1}) are slightly larger than what is expected for a spin-only Ni(II) ion (1.00 emu·K·mol^{-1}). When each complex is worked up as a {MPt}$_2$ dimer, the $\chi_M T$ value is also larger than expected for two non-interacting M(II) ions (Co(II): 3.75 emu·K·mol^{-1}; Ni(II): 2.00 emu·K·mol^{-1}).

Staggered & eclipsed bonded compounds

Grinding the crystals of **4.11** causes a color change from purple to yellow, suggestive of desolvation toward formation of **4.4**; XRD patterns indicate that the yellow powder does not have the same crystal structure as **4.11**.[20] Thus, magnetic measurements for **4.11** were carried out on loosely-packed collections of single crystals of the compound, which do not decompose under the SQUID conditions used. At 295 K, the $\chi_M T$ product for crystalline **4.11** is 4.59 emu·K·mol^{-1} (μ_{eff} = 6.06 μ_B). The susceptibility decreases upon cooling, reaching 0.18 emu·K·mol^{-1} at 5 K.

Room temperature values for **4.11** are larger than expected for two magnetically isolated high spin Co(II) (S = 3/2) ions with g = 2 (3.75 emu·K·mol^{-1}), but consistent with a significant orbital contribution to the susceptibility, common for Co(II) complexes. This behavior of **4.11**

suggests that the spins of the Co(II) ions couple antiferromagnetically; thus the data are interpreted as a $(CoPt)_2$ species.

In contrast, the Ni(II) compound **4.12** shows no sharp color changes upon grinding crystals into a powder. The temperature-dependent susceptibility data for crystalline samples and powdered samples give virtually identical data, and XRD data collected after SQUID measurements match the calculated pattern for **4.12**,[20] confirming that the structure of the powder is largely unchanged compared to the crystal. Similar to the cobalt analogue **4.11**, the data for **4.12** show antiferromagnetic coupling, this time of two S = 1 ions to give a singlet ground state. At 295 K, the $\chi_M T$ product for crystalline **4.12** is 1.81 emu·K·mol^{-1} (μ_{eff} = 3.80 μ_B). This value is only slightly lower than expected for two magnetically isolated Ni(II) ions with g = 2 (2.00 emu·K·mol^{-1} expected). The susceptibility decreases monotonically upon cooling, reaching 0.02 emu·K·mol^{-1} at 25 K and 0.01 emu·K·mol^{-1} at 5 K.

Like **4.11** and **4.12**, the $\chi_M T$ products for **4.13**, **4.14**, **4.15**, and **4.16** are presented as $\{MPt\}_2$ dimeric units, because the downturns suggest antiferromagnetic coupling of paramagnetic centers to afford singlet ground states. Moreover, attempts to interpret these data as {MPt} species give nonsensical results. At 300 K the $\chi_M T$ products for **4.13** and **4.15** are 5.71 and 5.74 emu·K·mol^{-1}, respectively (μ_{eff} = 6.76 and 6.78 μ_B), higher than expected for two magnetically uncoupled S = 3/2 Co(II) centers with g = 2 (3.75 emu·K·mol^{-1}), but consistent with spin-orbit coupling and unquenched orbital contributions to the magnetic susceptibilities. At 300 K the $\chi_M T$ products for **4.14** and **4.16** are 1.68 and 2.04 emu·K·mol^{-1} (μ_{eff} = 3.66 and 4.04 μ_B), respectively. These values are very similar to what would be expected for two uncoupled Ni(II) centers with g = 2 (2.00 emu·K·mol^{-1}). The ambient temperature susceptibilities reflect the first row transition metal employed and are not perturbed significantly by the apical ligand.
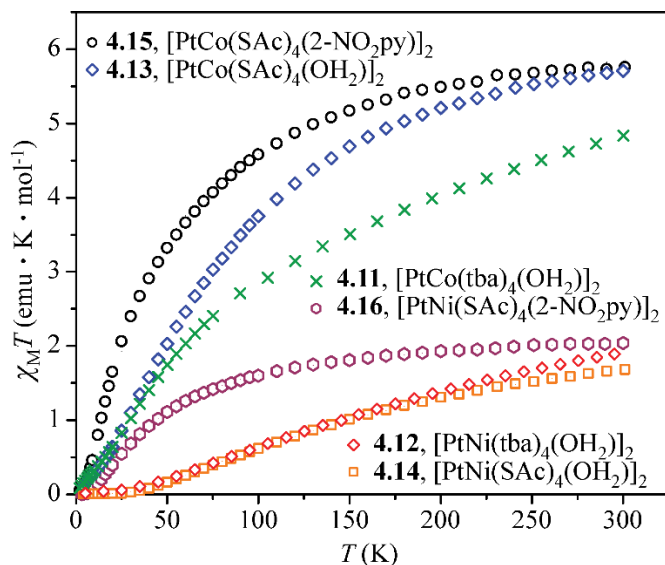
Figure 4.5. Temperature dependence of magnetic susceptibility for **4.11**–**4.16** measured at 1000 G. In each case, data are treated as M–Pt···Pt–M dimer units.

Infinite chain compounds

Infinite chain compounds **4.17** (2.22 emu·K·mol^{-1}) and **4.18** (1.19 emu·K·mol^{-1}) show room temperature $\chi_M T$ values (Figure 4.7) that are slightly larger than what is expected for spin-only M(II) ions (Co(II): 1.875 emu·K·mol^{-1} and Ni(II): 1.00 emu·K·mol^{-1}).
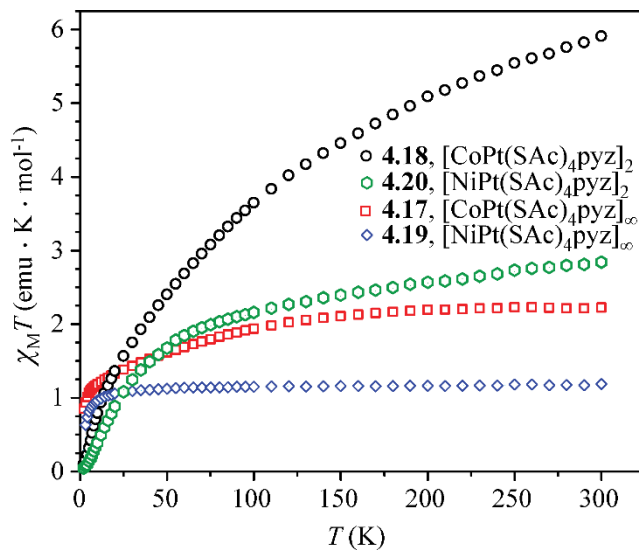
Figure 4.6. The magnetic susceptibility data for pyrazine-bridged chains **4.17** and **4.18** and dimers **4.19** and **4.20**.

Bridged dimer with offset non-bonded interaction compounds

The room temperature values for the pyrazine-bridged dimers **4.19** (5.91 emu·K·mol^{-1}) and **4.20** (2.84 emu·K·mol^{-1}) (Figure 4.7) are larger than what is expected for two non-interacting Co(II) ions (3.75 emu·K·mol^{-1}) or two non-interacting Ni(II) ions (2.00 emu·K·mol^{-1}), respectively, but consistent with spin-orbit coupling in the former case.

Open coordination site compounds

Lacking structural parameters for **4.21** and **4.22** makes meaningful magnetic fitting impractical. Therefore, magnetic data are not reported.

Magnetic Fitting: Non-bonded compounds

The low temperature downturns for **4.1**–**4.10** are consistent with zero-field splitting, which are expected to be small for octahedral Ni(II) due to the orbital symmetry, but significant for octahedral high-spin Co(II). Therefore, the low temperature downturns do not indicate magnetic coupling, so monomer fits were attempted using julX.[22] Dimer fits were also attempted for **4.5**–**4.10** to confirm the θ value obtained for the monomer. Fits to the $\chi_M T$ data for non-bonded complexes **4.1**–**4.10** are summarized in Table 4.2.

It is difficult to generate satisfactory fits for the $\chi_M T$ data of complex **4.1** without resorting to complex expressions for magnetic anisotropy (zero-field splitting) and spin-orbit coupling typical for paramagnetic pseudo-octahedral Co(II) centers. Fits obtained for Co(II)-containing **4.1** agree only moderately with the data (Figure 4.1). A non-θ fit, though lower quality, has parameters similar to **4.5**, **4.7** and **4.9** (*vide infra*). The θ fit, on the other hand, has a larger D than expected

and smaller TIP than expected. In the absence of significant intermolecular interactions, we conclude that the better fit is the non-θ model.
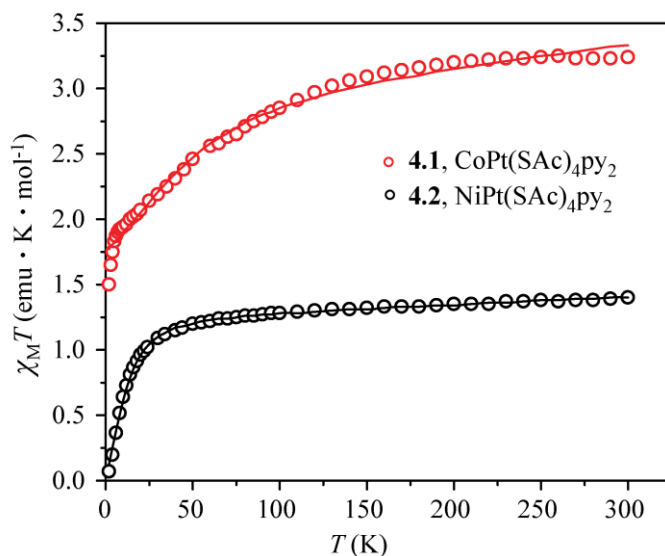
Figure 4.7. Temperature dependence of magnetic susceptibility for Co(II) complex **4.1**, and Ni(II) complex **4.2**. Best fits from julX are shown as solid lines.

In contrast, reasonable fits to the solid state magnetic susceptibility data are obtained for the Ni(II)-containing complex **4.2** (Figure 4.7).[22] Note that inclusion of θ does not significantly improve the fit of **4.2**. The lack of significant intermolecular contacts observed in the crystal structures suggests that the intermolecular mean field approximation parameter (θ in julX) should be negligible. Therefore, a model excluding θ was used to avoid over-parameterization.

Although the PtCo complexes in **4.4** show close intermolecular contacts via S atoms in the solid state (vide infra), attempts to fit the magnetic susceptibility data as a "dimeric" $(CoPt)_2$ species give negligible exchange coupling (J) values, which support the assumption of minimal Co⋯Co magnetic interactions and the treatment of **4.4** as a monomer. Superior fits (Figure 4.8) are obtained when **4.4** is treated as a monomeric species, fit to the Hamiltonian in Equation 4.1, albeit with a θ indicative of weak intermolecular exchange interactions.
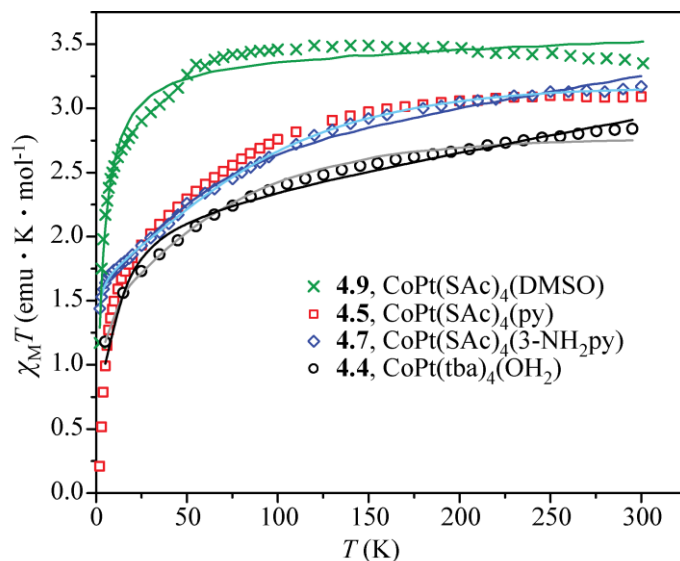
Figure 4.8. Temperature dependence of magnetic susceptibility for Co(II) complexes **4.4**, **4.5**, **4.7**, and **4.9**. Best fits from julX are shown as solid lines and best fits from MagSaki are shown as solid lines of light blue (**4.7**) and grey (**4.4**). No fit was obtained for **4.5**; see text for details.

The parameter D is refined for **4.1**–**4.3** and **4.5**–**4.10** to improve the fit quality and to model the anisotropic ground state that is available for these species. Unlike **4.11**–**4.16** (*vide infra*), models without D give significantly worse fits to the data. The counterpart to D, E (transverse anisotropy), is therefore included as well. For complexes **4.1**–**4.3** and **4.5**–**4.10**, E/D is fixed = 0.333 when free refinement gives $E/D > {}^1\!/_3$, which is equivalent to redefining the molecular axes. An E/D ratio of ${}^1\!/_3$ corresponds to maximum rhombic distortion, such that axial and planar anisotropy are both large. We generated fits to the magnetic susceptibility data for **4.4**, however, without including axial anisotropy (D) since $S = \frac{1}{2}$ states cannot have D (**4.4** acts like $S = \frac{1}{2}$ at low temperature). For comparison, we attempted fits where we treat "D" simply as a parameter to be varied.[20] In both cases, the "D"-inclusive fits are similar to the fits obtained without "D". Therefore, we concluded that reducing the number of parameters was warranted. These fits include a θ in both monomer and dimer cases to account for intermolecular interactions via the mean field

approximation: they are consistent with intermolecular interactions observed in the solid-state crystal structure.

The spin Hamiltonian used by julX does not explicitly account for unquenched orbital angular momentum and/or spin-orbit coupling, commonly encountered with 6-coordinate Co(II) complexes. Because julX does not explicitly treat the orbital contributions in **4.4** (it is used here for comparison with other complexes), we have also attempted simulations of the data using the MagSaki program,[24] (Figure 4.2). In this alternative fitting method, Sakiyama[27-30] and others[31-34] have considered effects of ligand-field distortions on the magnetic behavior of Co(II) ions. These systems can be modeled by accounting for the spin-orbit coupling (λ), axial ligand-field splitting (Δ), and an orbital reduction factor (κ).

Simulating the data for **4.4** with MagSaki[24] and fixing $S = 3/2$, $g = 2.0$, gives fitted parameters $\Delta = 351$ cm^{-1}, $\kappa = 0.7$, $\lambda = -173$ cm^{-1}, $\theta = -1.9$ K, and TIP $= 1.21 \times 10^{-4}$ emu/mol. These values are typical for a Co(II) ion in an axially-distorted octahedral ligand field.[32] If we assume no intermolecular interactions (i.e. θ fixed to 0 K), similar parameters are obtained: TIP $= 0.001000$ emu/mol (fixed), $\Delta = 658$ cm^{-1}, $\kappa = 0.66$, and $\lambda = -173$ cm^{-1}; note that Δ is larger and TIP refines to unreasonably small values, supporting the inclusion of θ.

It is also difficult to generate fits for the $\chi_M T$ data of complexes **4.5**, **4.7** and **4.9** due to zero-field splitting and spin-orbit coupling typical for paramagnetic pseudo-octahedral Co(II) centers. The data for Co(II)-containing **4.5** are not readily fit by monomeric or dimeric models. Even a likely overparameterized monomeric system with g, D, E/D, TIP, and θ, does not model the data well. The θ-inclusive fits are significantly better than the θ-exclusive fits, and make use of a large θ (-6.99 cm^{-1}), suggesting a dimer fit is promising. Unfortunately, attempted fits to a dimer model are not successful: the fits agree poorly with the data, and include an unexpectedly small J and

large TIP ($J \sim -1$ cm^{-1} & TIP ~ 0.003500). Moreover, the "best" fit parameters vary depending on the input starting parameters, indicating that the ground state is not well isolated. Several factors contribute to the difficulty in fitting this data. First, the $\chi_M T$ data show a low temperature trend to 0 emu K mol^{-1} reminiscent of antiferromagnetic coupling. Compared to complexes **4.7** and **4.9**, which trend to non-zero $\chi_M T$ values at low temperature, this trend makes fitting of **4.5** more difficult. However, the solid state structure does not show any unique interactions or ligand conformations that would contribute to antiferromagnetic coupling in this complex relative to the other Co(II) complexes. More significantly, both **4.5** and **4.10** show a slight increase in $\chi_M T$ as the temperature decreases (most easily observed at higher temperatures), which may be attributed to torquing of the particles in a magnetic field. This trend makes fitting of the data for **4.5** impractical with julX.

The data for **4.7** are fit comparatively well by a monomer model, however the fit quality is still poor. Dimer fits are unsatisfactory: J values are very small, suggesting monomer behavior; TIP is large, and adding θ does not improve the fits, but instead makes J even smaller. Alternate fits to **4.7** were attempted using the MagSaki program[24] and give similar results: with $S = {}^3/_2$ and $g = 2.0$ the best fit gives parameters $\Delta = 282$ cm^{-1}, $\kappa = 0.86$, $\lambda = -156$ cm^{-1}, $\theta = -0.34$ K, and TIP $= 2.93 \times 10^{-4}$ emu/mol. The Δ value is slightly smaller than expected, but other values are typical for a Co(II) ion in an axially-distorted octahedral ligand field.[32] Meanwhile, attempts to treat the data as a dimer and fit with MagSaki were unsuccessful. All attempts model the low temperature data moderately well, but not the data above 50 K.

The data for **4.9** agrees only moderately well with an initial monomer fit from julX, but attempting to improve the fit by inclusion of θ results in TIP < 0, which is physically meaningless. With TIP fixed $= 0.000450$ (close to the value obtained for the monomer fit without θ) we obtained

parameters that provide a more reasonable model for the data. A dimer model gives similar quality fits with $J \sim -0.5$ cm^{-1}, supporting the monomer model. Overall, the quality of this fit is mediocre: f is relatively large and the model does not fit the high temperature data very well. As mentioned above, torquing of the sample can cause the gradual increase in $\chi_M T$ as temperature decreases (most easily observed at high temperatures). We predict that the co-crystallized solvent molecule can play a role in intermolecular interactions, even though no well-defined hydrogen bonds are observed in the solid state. The effect of torquing on the sample can be masking this effect.

The best fit for Fe(II)-containing **4.3** using the Hamiltonian in Equation 4.1[22] gives a good fit (Figure 4.9), albeit with unexpectedly large TIP. For Fe(II) coordination complexes, we would normally expect g > 2 and TIP ~2×10^{-4} emu/mol. However, large TIP values are provisionally attributed to the influence of the heavy Pt(II) ion. Moreover, large TIP values have been previously observed for a Pd–Co(II) complex,[3] and explained by incorporating strong orbital coupling into the spin Hamiltonian,[26] The small θ is an indication of very weak intermolecular antiferromagnetic coupling in **4.3**, consistent with the hydrogen bonding interactions in the solid state (vide infra).

In contrast, reasonable fits to the solid state magnetic susceptibility data are obtained for Ni(II)-containing complexes **4.6** and **4.8** (Figure 4.9) using julX. Attempts to fit the data for **4.6** as a dimer gives a small but nonzero J value, suggesting there may be some coupling between the monomers; however, the fit quality (*f*) for the monomer is better, and the structural parameters (*vide supra*) support a monomer model. Similarly, fitting **4.8** as a monomer gives a good fit. Addition of a θ parameter suggests very little intermolecular interaction, and attempts to fit the data to a dimer model give a small J.
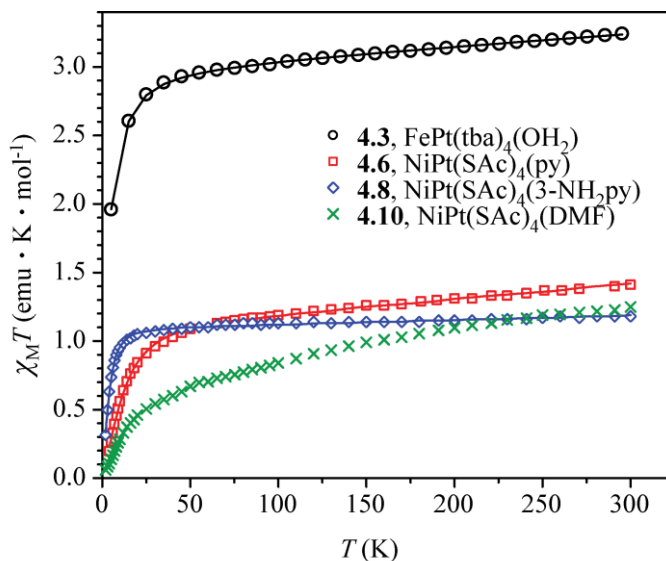
Figure 4.9. Temperature dependence of magnetic susceptibility for the Fe(II) complex **4.3** and Ni(II) complexes **4.6**, **4.8**, and **4.10**. Best fits from julX are shown as solid lines. No fit was obtained for **4.10**; see text for details.

Note that an appropriate theoretical fit for the magnetic susceptibility data of **4.10** has not been obtained. Fitting to a monomer model initially refines with g < 2.00. Ni(II) ions should have a $g > 2.00$, so this parameter is fixed in further refinements. Refinement of the other parameters gives a substantial θ, suggesting strong intermolecular interactions. Fitting as a dimer, however, suggests a contradictory result: without θ, an unsatisfactory fit is obtained, however, with θ, J is very small suggesting it is not a true dimer.

Magnetic Fitting: Bonded compounds

The best fit to the data for **4.11** using the Hamiltonian in Equation 4.2 to model a dimer gives a strong exchange coupling constant with the inclusion of $\theta = -6.4$ cm^{-1} is required to adequately fit the observed data ($f = 0.0335$). Antiferromagnetic coupling for **4.11** arises from both intra- and inter-dimer magnetic exchange interactions. Best fits to the data for **4.12**, **4.13**, **4.14**, **4.15**, and **4.16** were also obtained using the Hamiltonian in Equation 4.2 and best-fit parameters

are summarized in Table 4.3. Because the overall ground state of the antiferromagnetically coupled dinuclear systems is $S=0$ (and therefore $D=0$), we chose to continue using an isotropic exchange model, which allows us to compare coupling parameters between tba complexes and SAc complexes. Fits to **4.12** are straightforward, with a negligible θ and strong coupling between spin centers, especially compared to **4.11** (Figure 4.10).
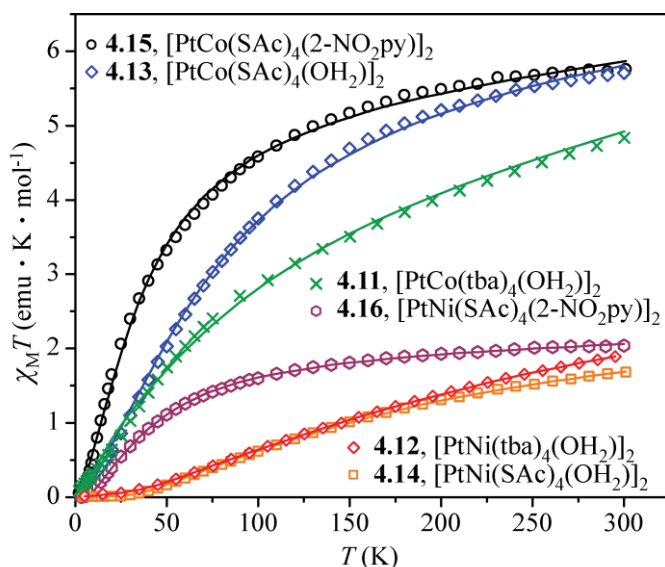
Figure 4.10. Temperature dependence of magnetic susceptibility for **4.11**–**4.16** measured at 1000 G. In each case, data are treated as M–Pt···Pt–M dimer units. The best fits obtained from julX are presented as solid lines. See the text for a description of the fitting methods and parameters.

An attempt was also made to simulate the magnetic data for **4.11** using MagSaki. Here, κ, λ, and Δ were obtained first by fitting the data above 100 K and then J was added to fit all the data. A large TIP value was necessary to reproduce the monotonic behaviour at higher temperatures: $g = 2.0$ (fixed), $\theta = 0$ K (fixed), $J = -11.6$ cm^{-1}, TIP $= 4.4 \times 10^{-3}$ emu/mol, $\kappa = 0.92$, $\lambda = -172$ cm^{-1}, $\Delta = 15.8$ cm^{-1}. For comparison, refining the θ parameter results in similar values: $g = 2.0$ (fixed), $\theta = -11.11$ K, $J = -11.1$ cm^{-1}, TIP $= 4.6 \times 10^{-3}$ emu, $\kappa = 0.92$, $\lambda = -173$ cm^{-1}, $\Delta = -15.9$ cm^{-1}.

Lacking independent determinations of simulated values (e.g. g from EPR), the simulation is over-parameterized; nevertheless, the values obtained are consistent with complexes containing axially-distorted Co(II) ions.

The aquo thioacetate complexes **4.13** and **4.14** readily desolvate in air, so are stored in water. Prior to SQUID analysis, samples of **4.13** and **4.14** were dried *in vacuo* at room temperature. A long drying sample of **4.13** was dried for 25 minutes and worked up as $[PtCo(SAc)_4(H_2O)]_2$, while a short drying sample was dried only until the visible storage water was removed and worked up as $[PtCo(SAc)_4(H_2O)]_2 \cdot 4H_2O$ (**4.4**): the data are nearly identical.[20] Initial fitting of **4.4** with all parameters freely refined gave many similar-quality fits to the data despite differing parameters. There is likely only weak coupling observed in this complex (and others, vide infra) resulting in an inability to model the poorly isolated ground state with julX. In this case, the fits all optimized with $g \approx 2.6$, therefore, by fixing this value a final set of fitted parameters were obtained (Figure 4.4).

A long drying sample of **4.14** was dried for 25 minutes, which resulted in a color change from yellow-green to lemon yellow, while a short drying sample was dried only until the visible storage water was removed and showed no color change. Data for the long drying sample were worked up as $[PtNi(SAc)_4(H_2O)]_2$ while data for the short drying were treated as $[PtNi(SAc)_4(H_2O)]_2 \cdot 4H_2O$ (**4.14**); slight differences in $\chi_M T$ can be attributed to unaccounted solvent loss.[20] Initial fitting attempts for **4.14** allowing all parameters, including TIP, to refine freely, optimized with values of TIP ≈ 0 emu/mol. Because the coordination environment is similar for **4.14** and **4.16** in terms of M$\cdots$Pt and Pt–Pt distances, TIP was fixed to 0.000500 emu/mol, which is similar to the value found for fits to the data for **4.16** (*vide infra*). The final fitted parameters were found in this way.

Fitted parameters obtained for **4.15** indicated several similar-quality fits with quite different TIP and θ parameters, which varied depending on input starting values for the parameters. We again attribute this behavior to weak coupling and a poorly isolated ground state (like **4.13**, *vide supra*). In several fits, $J \approx -6$ cm^{-1} and $g_1 = g_2 \approx 2.45$, therefore TIP and θ were refined with J and g fixed to those values to obtain a final set of parameters. For **4.16**, all parameters were freely refined to give final values.

Magnetic Fitting: Infinite chain and bridged dimer with offset non-bonding interaction compounds

Compounds **4.17** and **4.18** show $\chi_M T$ downturns that are consistent with zero-field splitting, but structural parameters suggest a chain structure with intermolecular contacts. Ferromagnetically coupled single chain magnets show $\chi_M T$ that increases continuously as temperature decreases. Antiferromagnetically coupled single chain magnets have an overall spin of zero, but $\chi_M T$ exhibits a rounded maximum before approaching a non-zero value at low temperature. Neither of these describes the data for **4.17** and **4.18**: if we extrapolate the data, it *would* go to zero, which suggests the data are not behaving as a chain with strong coupling. This is in contradiction with the crystallographic evidence, so both monomer and chain fits were attempted. Data for complexes **4.19** and **4.20** trend to zero at low temperature, and appear to be antiferromagnetic coupling rather than zero-field splitting, so fits using julX to a {MPt}$_2$ model were attempted.

A monomeric model from julX provides a moderately good fit to the data for both infinite chains **4.17** and **4.18**. For **4.17**, $g = 2.10$, $D = -65.15$ cm^{-1}, $E/D = 0.333$ (fixed), TIP = 0.0008157 emu/mol, and $\theta = -0.79$ cm^{-1} ($f = 0.0251$) and for **4.18**, the parameters are $g = 2.15$, $D = 4.48$ cm^{-1}, $E/D = 0.333$ (fixed), TIP = 0.0000806 emu/mol, and $\theta = -1.25$ cm^{-1} ($f = 0.00494$).

In both, θ is necessary to get reasonable fits (without, the fit is visibly worse and f is ~3 times larger), which corresponds to the infinite chain structure observed in the solid state.

We attempted the Bleaney-Bowers method of fitting a chain: the complex was treated as a ring of increasing size, such that the number of spin centers in the ring approaches infinity.[35] At this point, the ring will act like a chain and allow for calculation of coupling constants. Because of previous complications fitting Co(II) complexes due to orbital contributions, only **4.18** here is fit to the chain model as a preliminary test. The program julX was used to model the chain as a dimer, trimer and tetramer using the Hamiltonian in Equation 4.5. The fit quality is good and increasing the number of spins from dimer to trimer to tetramer gives the same parameters: $J_{12} = J_{23} = J_{34} = J_{14} = -0.454$ cm^{-1}, $g_1 = g_2 = g_3 = g_4 = 2.154$, all D, E/D and θ are fixed $= 0$ and TIP $= 0.0002574$ ($f = 0.00257$). Meanwhile, g and TIP are in the range expected for Ni(II) and J is small and negative suggesting weak antiferromagnetic coupling.

Next, fits were attempted with the program MagPack, which can consider rings of larger size (julX is limited to 4 spin centers). In this case, fits can be obtained with the ring size up to six (a hexamer) with $J = -0.7$ cm^{-1} and g = 2.18. (There is no "fitting" or error minimization in MagPack, just simulations and judging the fit quality visually.) Preliminarily, based on julX and initial MagPack values, J is very weak in the chain and g is similar to what we expect for Ni(II). The plot of normalized data is shown in Figure 4.11.

A good fit is obtained for the bridged-dimer **4.20** using the Hamiltonian in Equation 4.2. Interestingly, **4.20** refines to much stronger J than observed for the infinite chain and TIP an order of magnitude larger than expected for Ni(II) (reminiscent of **4.3**, **4.4**, **4.11**, and **4.12**). Unexpectedly, the inclusion of θ improves the fit (f ~ half) despite θ being small (-2.2 cm^{-1}). Like the {MPt}$_2$ dimers, inclusion of D and E/D did not change the other parameters or the fit quality.
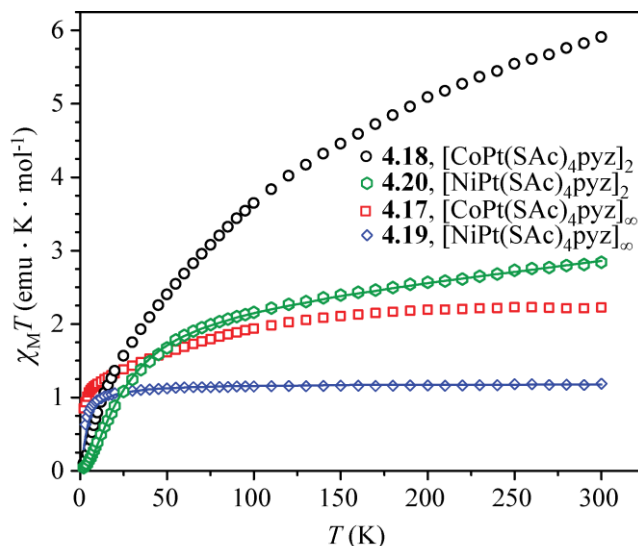
Figure 4.11. The magnetic susceptibility data for pyrazine-bridged chains **4.17** (red squares) and **4.18** (blue diamonds), and dimers **4.19** (black circles) and **4.20** (green hexagons). The best fit from MagPack for **4.18** and the best fit for **4.20** from julX are shown as solid lines. Due to difficulty fitting the data for **4.17** and **4.19**, no best fits are shown.

The fitting of **4.19** behaves differently: initial fits refine to $g < 2$, whereas Co(II) should have $g > 2$. A preliminary fit of just J and g gives a rough fit to the data with $g = 2.582$. With $g = 2.582$ fixed and other parameters added to the refinement, low quality fits are obtained with $f \sim 0.3$ (an order of magnitude larger than most of the other Co(II) fits). The inclusion of D and E/D does not improve the fit and thus were not used for refinements. When adding θ, J refines to ~ 0 and θ refines to ~ -50 cm^{-1}. Because of this irrational result, and the structural similarity to the monomeric [PtM(SAc)$_4$(L')] complexes, only fits *without* θ are reported. Ultimately, simulations were performed while decreasing the value of g: this improves the fits while decreasing J and increasing TIP. The "best" fit here is still only moderate quality; the relative energies of each fit are likely similar, preventing julX from being able to isolate a true best fit. Again, julX does a poor job of fitting the data here, at least in part due to problems based on unquenched orbital momentum.

Table 4.2. Comparison of fitted magnetic parameters and structural parameters for non-bonded complexes studied herein.[a]

	Solid state $\chi_M T$ at 300 K (emu K mol^{-1})	D (cm^{-1}) [b]	g	TIP (emu K mol^{-1})	θ (cm^{-1})	f [c]	Pt···Pt [d] (Å)	M–Pt (Å)	Pt···X (Å) (closest)	Angle of Offset (°)
4.1	3.24	50.2	2.49	0.001510	0 [e]	0.0599	n/a	2.5817(7)	2.567(4), X=N	n/a
4.2	1.40	29.2	2.22	0.000580	0 [e]	0.0152	n/a	2.5506(4)	2.533(2), X=N	n/a
4.3	3.24	6.253	1.99	0.000907	−0.72	0.0066	4.2517(2)	2.6320(6)	3.2596(9), X=S	134.63(2)
4.4	2.85	0 [f]	2.18	0.002490	−4.3	0.0589	3.9713(3)	2.5521(5)	2.978(1), X=S	134.46(1)
4.5	3.09						4.3042(3)	2.6298(5)	3.0774(9), X=S	133.03(1)
4.13	1.41	30.5	2.09	0.001072	0 [e]	0.0127	4.2308(6)	2.5831(6)	3.0587(9), X=S	133.51(1)
4.7	3.18	52.3	2.37	0.002180	0 [e]	0.0454	4.1224(3)	2.6405(4)	3.2646(7), X=S	142.51(1)
4.15	1.18	9.773	2.09	0.000324	0 [e]	0.0079	4.1304(2)	2.5951(3)	3.2123(6), X=S	140.34(1)
4.9	3.35	0.012	2.70	0.000450	−2.28	0.0915	3.8489(3)	2.6223(9)	3.225(2), X=S	146.38(2)
4.10	1.25						4.2171(2)	2.5571(6)	3.0716(9), X=S	135.14(1)

(a) Best fit parameters for **4.5**, are **4.10** are not reported; see the text for explanations; (b) when D is refined, E/D is as well, for all cases, E/D is fixed = 0.333 except for **4.2** where it refines to 0.279. More information is provided in the text; (c) sum of the deviation squared; (d) non-bonding interaction; (e) fixed parameter; (f) parameter refined to ~0, so it was fixed at 0.

Table 4.3. Comparison of fitted magnetic parameters and structural parameters for bonded complexes studied herein.[a]

	$\chi_M T$ at 300 K (emu K mol^{-1})	J (cm^{-1})	g	TIP (emu K mol^{-1})	θ (cm^{-1})	J/θ	f[b]	Pt$\cdots$X (Å)	dihedral angle, τ (°)	M–Pt (Å)
				bonded dimer						
4.11	4.59	−10.8	2.15	0.003470	−6.4	1.69	0.0335	3.0650(3), X=Pt	45.0(17.6)	2.5992(7)
4.12	1.81	−60	2.187	0.001220	0 [d]	undef	0.0039	3.0823(4), X=Pt	45.0(5.6)	2.570(1)
4.4	5.71	−12.7	2.6[c]	0.001657	−2.5	5.08	0.0572	3.1261(3), X=Pt	45.0(8.2)	2.6343(5)
4.14	1.68	−50.8	2.14	0.000500[c]	−2.3	22.08	0.0058	3.0794(6), X=Pt	45.0(8.2)	2.585(2)
4.16	5.74	−6.0[c]	2.45[c]	0.002181	−0.6	10	0.0678	3.489(2), X=Pt	0.7(0.1) [e]	2.6347(4)
4.16	2.04	−12.6	2.04	0.000491	0 [d]	undef	0.0059	3.0583(4), X=Pt	45.0(1.7)	2.5682(9)
infinite chain [f]										
4.17	2.22							2.65(1), X=N	n/a	2.588(2)
4.18	1.19	−0.7	2.18					2.539(2), X=N	n/a	2.539(2)
bridged dimer										
4.19	5.91	−7.8	2.20	0.005668	0 [c]	undef	0.2210	3.3232(7), X=S	n/a	2.5986(4)
4.20	2.84	−7.7	2.18	0.001998	−2.2	undef	0.0108	3.3278(9), X=S	n/a	2.5597(4)

(a) Best fit parameters for **4.18** are not reported. See the text for explanations; (b) sum of the deviation squared; (c) fixed parameter; (d) parameter refined to ~0, so it was fixed at 0; (e) note PtS$_4$ faces are slipped; (f) best fit parameters from MagPack

4.5 Discussion

Electronic Structure

A general MO scheme for the *d*-orbitals in [PtNi(tba)$_4$] is shown in Figure 4.12. The sides of Figure 4.12 show the qualitative ligand field splitting and high-spin occupation expected for a {NiO$_4$} environment and the low-spin environment for {PtS$_4$}. The center of Figure 4.12 indicates how these two square planar centers overlap to form a new high spin system. This qualitative MO description provides an illustrative example of the M–Pt orbitals, for example the σ* and Ni(II)-based dx^2-y^2 SOMOs, that overlap to allow for Pt–Pt electronic communication. Stronger coupling between the original M- and Pt-orbitals results in greater electron density on Pt-based orbitals and therefore stronger Pt–Pt coupling.
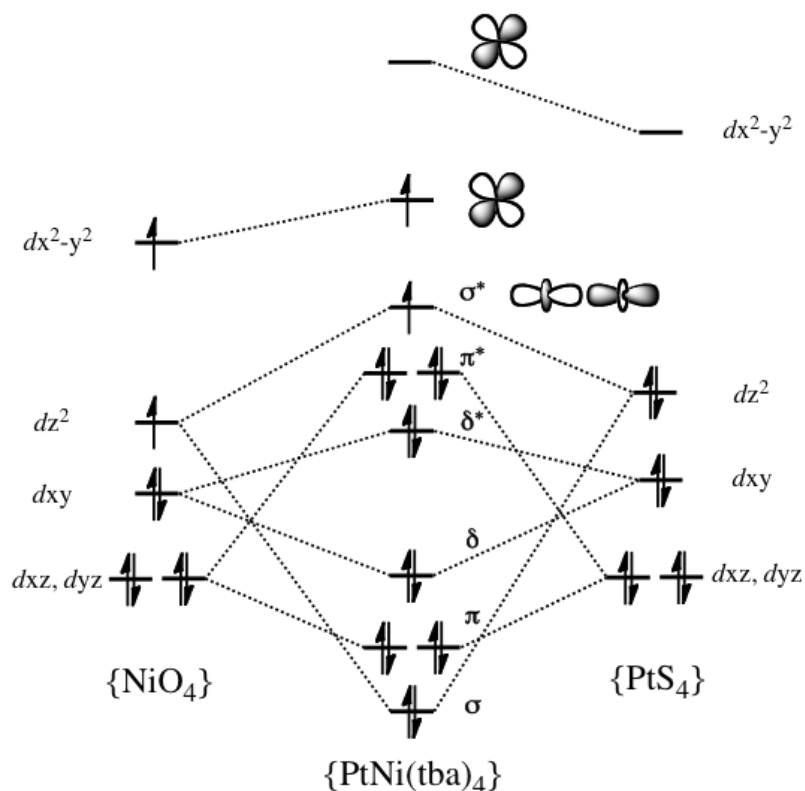
Figure 4.12. Qualitative MO Diagram for Pt-Ni interaction in [PtNi(tba)$_4$(OH$_2$)]. Reproduced from reference 20.

Magneto structural correlations

Besides the Pt···Pt non-covalent interactions, alternative or additional pathways for antiferromagnetic coupling may arise through intermolecular contacts between [PtM(L$_{SO}$)$_4$(OH$_2$)] lantern units. The non-bonded monomeric compounds, **4.1** and **4.2**, exist as nearly isolated complexes. These compounds have a pyridine cap on each metal atom, which precludes the formation of intermolecular interactions. Similarly, fitting attempts that include a mean field approximation to account for intermolecular interactions show little improvement over fitting attempts without intermolecular interactions.

Offset non-bonded compounds show potential for intermolecular interactions through close Pt–S contacts and hydrogen bonds. Although these intermolecular interactions between molecules are noted, there is no evidence for strong antiferromagnetic coupling in the magnetic data. Compound **4.3** shows H-bonding contacts between the axial water molecule and one lattice acetone molecule and one carboxylate oxygen of a neighboring molecule, resulting in a H-bonded dimer. Axial water-carboxylate interactions for **4.4** also give an H-bonded dimer in the solid state like that of **4.3**. The platinum centers of **4.5**–**4.10** are not terminated by an axial ligand allowing for the formation of reciprocal, short intermolecular Pt···S contacts creating an offset dimer of lantern units. Unlike **4.3** and **4.4**, **4.5** and **4.6** show no evidence of intermolecular hydrogen bonds or other interactions that could contribute to magnetic coupling. The NH$_2$py complexes, **4.7** and **4.8**, on the other hand, show hydrogen-bonding interactions between an NH$_2$ moiety on one molecule and two S atoms on adjacent molecules. Complexes **4.9** and **4.10** are unique in that the complexes co-crystallize with a solvent molecule, however, these molecules do not induce hydrogen bonds.

Qualitatively, the temperature dependence of the $\chi_M T$ product of **4.10** is between the monomeric behavior of **4.11**, **4.13** and **4.15** and the dimeric behavior of **4.12**, **4.14**, and **4.16**, possibly indicating that both single-ion anisotropy and intermolecular antiferromagnetic coupling are operative. In addition to possible coupling in **4.10**, attempts to fit **4.9** with julX (*vide infra*) suggest θ is important and that intermolecular coupling plays a role. The oxygen-containing compounds **4.9** and **4.10** are the only two species reported here that contain co-crystallized solvent molecules, and which show factors indicative of antiferromagnetic coupling. We reason that the co-crystallized solvent may contribute to the intermolecular interactions, even without well-defined intermolecular contacts, e.g. hydrogen bonds. These interactions complicate the expected fitting procedure.

As noted before, julX is not the best model for a system with unquenched orbital momentum because it ignores orbital contributions. This complication helps explain why we observe much larger D values than expected for transition metal complexes. Nevertheless, the relatively simple model used here allows for comparison between compounds **4.1**–**4.16**. Regardless of the poor fit qualities obtained here, fitting attempts with julX support monomer models for the data. In all cases, the dimer parameters are nonsensical and/or provide worse fits than the monomer models. Coupled with similar structural parameters for all complexes presented herein, we conclude that in these complexes there is little or no magnetic coupling between paramagnetic centers via Pt–Pt interactions.

It is clear from attempts to fit the data for the complexes **4.1**–**4.10** using a spin-only model obtained from julX that the complexes behave as "monomeric" {PtM} units. Similar fitting attempts for **4.4** and **4.7** using Magsaki are also consistent with the conclusion that modeling these complexes as {PtM}$_2$ species yield nonsensical results. These data suggest that the short Pt···S and

S···S contacts observed in offset dimer structures do not facilitate an antiferromagnetic coupling interaction that has been observed when short Pt···Pt interactions exist between staggered or eclipsed lantern units.

Structural parameters for **4.5**–**4.10** support monomer models for the complexes. The *Pt–S* distances are similar to the *Pt–Pt* distances in the dimers **4.13**–**4.16** (*vide infra*). The qualitative MO diagram suggests that magnetic exchange occurs through Pt–Pt orbital overlap, therefore, the longer physical separation would likely decrease the dimer nature and increase the monomer nature of the complexes. Furthermore, the distortion/angle of offset could give some explanation why coupling through the ligand would be weak. Optimized orbital overlap would be required to give strong communication. Based on orbital geometry, overlap is predicted to be strongest when the Pt–S–Pt angle is 90° or 180°. The deviation from linearity indicated by the angle of offset suggests that communication through the Pt–S interaction is weakened. Combining weak overlap with long Pt–Pt separation supports modeling these complexes as monomers rather than dimers.
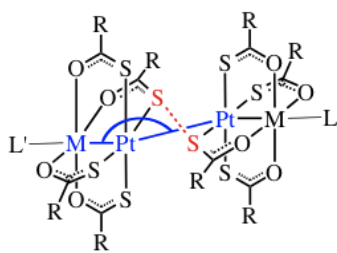
Figure 4.13. Angle of offset illustrated in blue and a short S−S contact highlighted in red.

The bonded dimeric compounds **4.11**–**4.16** show possibilities for antiferromagnetic coupling through the Pt–Pt orbital overlap indicated in the electronic structure estimation (*vide infra*). For example, in compound **4.11**, the axial water-carboxylate interactions on both ends of the dimer result in a H-bonded chain of dimers, giving rise to intermolecular magnetic interactions. Although structurally both **4.11** and **4.4** show intermolecular interactions in the solid state, the

paths for possible magnetic exchange are significantly different, such that **4.11** is best thought of as a (CoPt)$_2$ species while **4.4** acts more like a (CoPt) entity. The differences in the magnetic behavior of **4.11** and **4.4** strongly suggest that the Pt···Pt contact in **4.11** is associated with the antiferromagnetic coupling in that case. The DFT calculations described previously[19-20] show unpaired electron density in orbitals formed from dz^2(Pt)–dz^2(M) overlap. Coupling of electrons from each of two 3d metals via the Pt···Pt non-bonded contact is possible and supported by these electronic structure studies.

Among **4.3**, **4.4**, **4.11**, and **4.12**, **4.12** contains the most isolated molecules, and the strongest *inter*molecular antiferromagnetic coupling: H-bonding between lantern units is interrupted by solvate THF molecules. One axial water molecule of **4.13** forms H-bonding interactions with a molecule of lattice water and to an oxygen from a thioacetate moiety of a neighboring lantern unit, while the other terminal aquo forms H-bonding contacts with two molecules of lattice water. Compound **4.14** forms the same H-bonding contacts as **4.13**; despite longer hydrogen bonding interactions than are observed in **4.13**, there is a greater degree of antiferromagnetic coupling in **4.14**. Furthermore, a H-bonding pathway for magnetic coupling cannot be operative in **4.15** and **4.16** as no hydrogen bonding interactions are present in the lattice. Conversely, complexes **4.7** and **4.8** show an intermolecular hydrogen-bonding lattice yet are fit with a monomer model as well as the pyridine-analogues **4.5** and **4.6**. The lack of a correlation between the presence of hydrogen bonding in {PtM}$_n$ species and the degree of intermolecular antiferromagnetic coupling suggests that another orbital pathway is responsible for the magnetic properties.

Several trends emerge from a comparison of the susceptibility data. First, the Ni(II)-containing complexes **4.12**, **4.14** and **4.16** consistently show significantly stronger intramolecular

exchange interactions (larger $|J|$) and more isolated behavior (larger $J/|\theta|$) than the Co(II) analogs. This pattern does not seem to be correlated to Pt$\cdots$Pt distances or the S-Pt$\cdots$Pt-S dihedral angle τ (Table 4.3), but instead likely reflects differences in M-Pt orbital overlap. Specifically, stronger coupling observed for the Ni(II)-containing complexes suggests better M–Pt orbital overlap and more facile Pt–Pt coupling. Second, the substitution of thiobenzoate (tba) with thioacetate (SAc) has a moderate but inconsistent effect on the strength of magnetic exchange, as $|J|$ changes by ~17% upon adoption of SAc, this is an increase for the Co(II) complex and a decrease for the Ni(II) analog. Local structural parameters (Pt$\cdots$Pt distance, {MPt}$_2$ dihedral angles) are similar for the Ni(II) complexes, and the Pt$\cdots$Pt distance actually increases for the Co(II) complex (tba vs SAc), suggesting that the structural changes are not directly responsible for the changes in coupling.

Combining both the intra- and intermolecular exchange terms, one can argue that the SAc ligand decreases coupling overall for both **4.13** and **4.14**, but packing effects or intermolecular interactions appear to isolate the {CoPt}$_2$ species better for SAc than tba, resulting in a somewhat larger relative coupling constant (i.e. larger $J/|\theta|$). Third, the substitution of apical aquo with py-NO$_2$ ligands significantly reduces the coupling between {MPt} units. It is tempting to add that the py-NO$_2$ ligands also increase separation of {MPt}$_2$ dimers, but that is confounded somewhat by the slightly different structure of **4.15** compared to the other species. Further substitution with py and pyNH$_2$ appears to further reduce the coupling, concomitant with a structural shift that eliminates the Pt–Pt overlap.

The fits for the infinite chain complexes **4.17** and **4.18** require some special consideration. As is, the data for **4.18** is fit well as a hexamer; a true infinite chain model may not show significantly different fitted values, but is important for completeness. Understanding the fitting method for **4.18** will aid in fitting the Co(II) analogue **4.17**, which has not been attempted.

Compared to the dimers, the coupling constant J is small, however, the data is qualitatively quite similar to the offset dimers. Structural parameters suggest an extended network of interactions, but as we have seen, intermolecular interactions in the solid state are not a guarantee of magnetic interactions. The Pt–N$_{(pyz)}$ distances observed are notably longer than those for other Pt–N$_{(pyz)}$ distances in the literature, suggesting the antiferromagnetic coupling might be weaker than otherwise anticipated.[17]

Both dimers **4.19** and **4.20** exhibit strong coupling through the pyrazine bridge, as expected based on the symmetrical covalent bonds and extended π system, which allow for efficient electronic communication. In addition, each shows Pt–S intermolecular contacts to form offset P–P interactions as observed in the monomeric complexes **4.5**–**4.10**. The value for θ suggested by julX for **4.21** is small, but significant, while that suggested for **4.20** is contradictory with the J value suggested. Meanwhile, the angle of offset, Pt–S distances and M–Pt distances are similar to the monomers, suggesting that **4.20** and **4.21** are best considered as dimers rather than polymers.

4.6 Conclusions

In summary, novel heterobimetallic lantern compounds have been prepared and thoroughly characterized, including an electronic structure description of the intra-lantern Pt-M interaction and the dimeric {MPtPtM} interactions. Both **4.1** and **4.2** exhibit an isolated non-bonded structure in the solid state. All other derivatives exhibit "dimeric" structures in the solid state linked *via* close Pt···Pt interactions or Pt···S interactions. Most of these complexes, **4.3**–**4.10**, exhibit magnetic data that supports a monomeric model, despite the intermolecular interactions that exist in the solid state. In this way the lantern units **4.1**–**4.8** are best considered as monomeric magnetic

species, while **4.9** and **4.10** may contain some elements of intermolecular antiferromagnetic coupling. Further analysis of the ambiguous fits is required to determine reliable fitted parameters to compare with other results. This analysis can include duplication of data to test reproducibility and additional magnetization or EPR experiments to confirm D and E/D parameters from julX.

Compounds **4.11**–**4.16** exhibit magnetic data that indicates antiferromagnetic coupling of paramagnetic $3d$ metal ions occurs through Pt$\cdots$Pt interactions. The magnetic coupling observed in these complexes is, to the best of our knowledge, the first time that any dispersion interaction has been shown to give rise to any magnetic coupling via a metallophilic contact. It has been determined that neither the Pt$\cdots$Pt interaction between lantern complexes nor the resulting antiferromagnetic coupling is an isolated phenomenon of the thiobenzoate supporting ligand, nor is an axially coordinated H_2O required for the formation of the observed tetrametallic units. Furthermore, we note that for all of these complexes, intermolecular interactions appear to play a role by imparting weak magnetic interactions, but the strength of the Pt$\cdots$Pt coupling is relatively independent of intermolecular contacts. Instead, we notice that the *relative* coupling $J/|\theta|$ shows a correlation to ligand size and intermolecular interactions.

Additionally, infinite molecular chains of the form $[PtM(SAc)_4(pyz)]_\infty$ (M = Co(II), Ni(II)) and dimeric complexes of the form $[PtM(SAc)_4(pyz)_{0.5}]_2$ (M = Co(II), Ni(II)) were synthesized and examined. The structural parameters of the infinite chain suggest an extended intermolecular interactions, however the magnetic susceptibility data is fit equally well by a monomer model as by a tetramer or hexamer model. Further investigation is required to analyze this system. The dimer complexes show covalently bonded pyz-bridged M(II) atoms, which are antiferromagnetically coupled. The structures also exhibit "off-set dimer" type interactions to form an extended network.

Like the off-set dimers, these interactions do not impart magnetic coupling to the system, resulting in relatively isolated dimeric species, rather than extended polymeric systems.

4.7 Acknowledgments

CHAPTER 4 REFERENCES

1. Lahti, P. M., *Magnetic Properties of Organic Materials*. Marcel Dekker: 1999.
2. Krause, W., *Contrast Agents I: Magnetic Resonance Imaging (Topics in Current Chemistry) (Part 1)*. Springer: 2002.
3. Rohmer, M. M.; Liu, I. P. C.; Lin, J. C.; Chiu, M. J.; Lee, C. H.; Lee, G. H.; Benard, M.; Lopez, X.; Peng, S. M., *Angew. Chem. Int. Ed.* **2007**, *46*, 3533-3536.
4. Liu, I. P. C.; Chen, C. H.; Chen, C. F.; Lee, G. H.; Peng, S. M., *Chem. Commun.* **2009**, 577-579.
5. Jansen, M., *Angew. Chem. Int. Ed.* **1987**, *26*, 1098-1110.
6. Pyykko, P., *Chem. Rev.* **1997**, *97*, 597-636.
7. Schmidbaur, H.; Schier, A., *Chem. Soc. Rev.* **2008**, *37*, 1931-1951.
8. Doerrer, L. H., *Dalton Trans.* **2010**, *39*, 3543-3553.
9. Bera, J. K.; Dunbar, K. R., *Angew. Chem. Int. Ed.* **2002**, *41*, 4453-+.
10. Greenwood, B. P.; Forman, S. I.; Rowe, G. T.; Chen, C. H.; Foxman, B. M.; Thomas, C. M., *Inorg. Chem.* **2009**, *48*, 6251-6260.
11. Nippe, M.; Bill, E.; Berry, J. F., *Inorg. Chem.* **2011**, *50*, 7650-7661.
12. Pal, K.; Nakao, K.; Mashima, K., *Eur. J. Inorg. Chem.* **2010**, 5668-5674.
13. Cindric, M.; Vrdoljak, V.; MatkovicCalogovic, D.; Kamenar, B., *Acta Crystallographica Section C-Crystal Structure Communications* **1996**, *52*, 3016-3018.
14. Dikareva, L. M. S., G. G.; Porai-Koshits, M. A; Golubnichaya, M. A.; Baranovskii, L B.; Shchelokov, R. N., *Russ. J. Inorg. Chem.* **1977**, *22*, 1093.
15. Mehmet, N.; Tocher, D. A., *Inorg. Chim. Acta* **1991**, *188*, 71-77.
16. Melson, G. A.; Crawford, N. P.; Geddes, B. J., *Inorg. Chem.* **1970**, *9*, 1123-&.
17. Baddour, F. G. PhD Thesis. Boston University, Boston, 2013.
18. Baddour, F. G.; Fiedler, S. R.; Shores, M. P.; Golen, J. A.; Rheingold, A. L.; Bacon, J. W.; Doerrer, L. H., *Submitted* **2013**.
19. Baddour, F. G.; Fiedler, S. R.; Shores, M. P.; Golen, J. A.; Rheingold, A. L.; Doerrer, L. H., *Inorg. Chem.* **2013**, *52*, 4926-4933.
20. Dahl, E. W.; Baddour, F. G.; Fiedler, S. R.; Hoffert, W. A.; Shores, M. P.; Yee, G. T.; Djukic, J. P.; Bacon, J. W.; Rheingold, A. L.; Doerrer, L. H., *Chem. Sci.* **2012**, *3*, 602-609.
21. Bain, G. A.; Berry, J. F., *J. Chem. Educ.* **2008**, *85*, 532.
22. Bill, E. julX; Version 1.41; Max Planck Institute for Bioinorganic Chemistry, Mullheim an der Ruhr. http://ewww.mpi-muelheim.mpg.de/bac/logins/bill/julX_en.php; 2008.
23. Shores, M. P.; Sokol, J. J.; Long, J. R., *J. Am. Chem. Soc.* **2002**, *124*, 2279-2292.
24. Sakiyama, H. *MagSaki*, Sakiyama Laboratory: 2007.
25. Evans, D. F., *J. Chem. Soc.* **1959**, 2003-2005.
26. Van den Heuvel, W.; Chibotaru, L. F., *Inorg. Chem.* **2009**, *48*, 7557-7563.
27. Sakiyama, H., *Inorg. Chim. Acta* **2006**, *359*, 2097-2100.
28. Sakiyama, H., *Inorg. Chim. Acta* **2007**, *360*, 715-716.
29. Sakiyama, H.; Ito, R.; Kumagai, H.; Inoue, K.; Sakamoto, M.; Nishida, Y.; Yamasaki, M., *Eur. J. Inorg. Chem.* **2001**, 2705-2705.
30. Sakiyama, H.; Ito, R.; Kumagai, H.; Inoue, K.; Sakamoto, M.; Nishida, Y.; Yamasaki, M., *Eur. J. Inorg. Chem.* **2001**, 2027-2032.
31. Herrera, J. M.; Bleuzen, A.; Dromzee, Y.; Julve, M.; Lloret, F.; Verdaguer, M., *Inorg. Chem.* **2003**, *42*, 7052-7059.

32.   Hossain, M. J.; Yamasaki, M.; Mikuriya, M.; Kuribayashi, A.; Sakiyama, H., *Inorg. Chem.* **2002**, *41*, 4058-4062.

33.   Rodriguez, A.; Sakiyama, H.; Masciocchi, N.; Galli, S.; Galez, N.; Lloret, F.; Colacio, E., *Inorg. Chem.* **2005**, *44*, 8399-8406.

34.   Toma, L. M.; Lescouezec, R.; Pasan, J.; Ruiz-Perez, C.; Vaissermann, J.; Cano, J.; Carrasco, R.; Wernsdorfer, W.; Lloret, F.; Julve, M., *J. Am. Chem. Soc.* **2006**, *128*, 4842-4853.

35.   Kahn, O., *Molecular Magnetism.* VCH: New York, 1993.

CHAPTER 5: MAGNETIC-STRUCTURAL RELATIONSHIPS IN AN ASYMMETRIC TRINUCLEAR MANGANESE COMPLEX AND TWO SQUARE PLANAR MONONUCLEAR COMPLEXES OF COBALT OR IRON

5.1 Introduction

The study of unexpected structural parameters and magnetic properties provides insight into the correlation of these two important features. The discovery of novel complexes with interesting magnetostructural relationships can guide future development of complexes with specific, desirable properties and behavior. Though often serendipitous, rational design of such complexes could be preferential for widely applicable complexes. In this chapter I discuss two examples: first, an asymmetric trinuclear manganese structure with magnetic coupling between metal atoms and second, two mononuclear high-spin square-planar complexes.
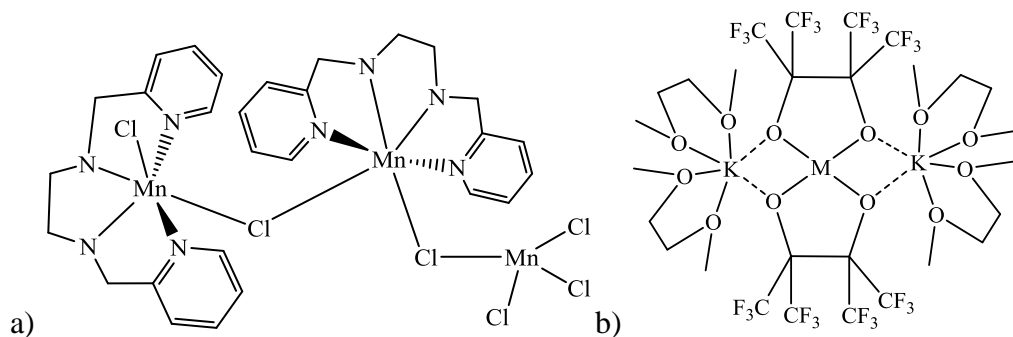
Figure 5.1. a) The trinuclear manganese comples, **5.1** and **b)** the generic structure of **5.2** and **5.3**.

Christian Goldsmith's group at Auburn University became interested in trinuclear manganese structures with Mn(II) and Mn(III) ions arrayed in either triangular (closed structure)[1-5] or linear (open structure) geometries,[3,5-13] which can serve as precursors to higher nuclearity clusters. Asymmetric linear [$Mn^{III}Mn^{III}Mn^{II}$] and [$Mn^{II}Mn^{II}Mn^{II}$] compounds have been reported,

but are rare: in two recent examples, the manganese ions are bridged and oriented by long polydentate ligands.[12-13] When they synthesized an unusual example of an asymmetric linear array of chloride-bridged Mn(II) ions (**5.1**), with each metal ion in a different coordination environment, we examined the magnetic properties. We found that the type and strength of magnetic coupling observed between each pair of metal ions is directly impacted by the coordination environment.

Linda Doerrer's group at Boston University is interested in investigating coordination compounds with interesting geometry in order to probe our understanding of unusual and unexpected species. For example, ligand field strength in transition metal complexes has been well-studied; the number and type of donor atoms, ligand substituents, and the presence or absence of chelate rings all influence metal spin states. In spite of such variety, high-spin, square-planar complexes are rare because the large separation of the dx^2-y^2 orbital from the rest of the d-manifold favors low-spin electron configurations for d^n with $n > 4$, and four-coordinate compounds are rare for d^4 systems which could have all four low-lying d-orbitals half filled.

Spectroscopic[14] and computational[15] work on other homoleptic fluorinated aryloxide and alkoxide complexes have shown that these fluorinated ligands are medium field ligands, on par with OH^- and F^-, and stronger than NCO^-. The electron-withdrawing power of extensively fluorinated ligands reduces the π-donor character of the O atom, such that bridging is not observed and mononuclear species are readily prepared. Despite the relative ease in making $[M(ddfp)_2]^{2-}$ complexes with first row transition metals, no examples of M = Co^{II} or Fe^{II} have been published. When her group synthesized a high-spin, square-planar Co^{II} complex, $\{K(DME)_2\}_2[Co(ddfp)_2]$, **5.2** and an analogous high-spin, square-planar Fe^{II} complex $\{K(DME)_2\}_2[Fe(ddfp)_2]$, **5.3** we investigated the magnetic data to further probe the spin state**.** The syntheses, characterization and

magnetic susceptibility data for the trinuclear manganese complex, **5.1** as well as the square planar complexes **5.2**–**5.3** have been reported in the literature.[16-17]

5.2 Division of Labor

Synthesis and non-magnetic characterizations for compound **5.1** were performed by Christina M. Coates and T. Laura McCullough at Auburn University. Procedures, results and discussion of this compound have been reported.[17] Synthesis and non-magnetic characterization for compounds **5.2** and **5.3** were performed by Stefanie A. Cantalupo at Boston University. Procedures, results and discussion of these compounds have been reported.[16] Magnetic characterization, data fitting and analysis of all compounds was performed by Stephanie R. Fiedler.

5.3 Experimental Section

Synthetic details of **5.1** and characterization by NMR, EA, EPR, cyclic voltammetry and x-ray crystallography have been previously reported.[17] Synthetic details of **5.2** and **5.3** and characterization by NMR, EA, EPR, cyclic voltammetry, and x-ray crystallography have been previously reported.[16]

Magnetic Measurements of 5.1

Magnetic susceptibility data were collected using a Quantum Design MPMS-XL SQUID magnetometer at temperatures ranging from 2 to 300 K under an applied field of 1000 G. Powdered samples were loaded into gelatin capsules and inserted into straws for analysis. Magnetization data were collected at temperatures ranging from 2 to 25 K under applied fields of 10, 20, 30, 40 and 50 kG. Samples for magnetization studies were encased in eicosane to prevent torquing of

crystallites at high magnetic fields. Alternating current (AC) susceptibility data were collected at temperatures ranging from 2 to 5 K in a zero applied direct current (DC) field and a 1-G AC field oscillating at a frequency of 100 Hz. All data were corrected for diamagnetic corrections using Pascal's constants and by subtracting the diamagnetic susceptibility of an empty sample holder.

Susceptibility data were fit to magnetic models using a trinuclear exchange Hamiltonian in Equation 5.1 using the program julX[18-19] where S is the local spin multiplicity of each spin center and Jij is the exchange coupling constant between the ith and j[th] spin centers.

$$\hat{H} = -2J_{12}(\hat{S}_1 \cdot \hat{S}_2) - 2J_{23}(\hat{S}_2 \cdot \hat{S}_3) - 2J_{13}(\hat{S}_1 \cdot \hat{S}_3) \tag{5.1}$$

In addition, the spin-Hamiltonian from ANISOFIT in Equation 5.2 was used to model magnetic data where D and E are the axial and rhombic zero-field splitting parameters, respectively, of each spin center, S is the local spin multiplicity of each spin center, B is the magnetic field vector and g is the isotropic average of the g value for each spin center.

$$\hat{H} = D\hat{S}_z^2 + E\left(\hat{S}_x^2 + \hat{S}_y^2\right) + g_{iso}\mu_B \mathbf{S} \cdot \mathbf{B} \tag{5.2}$$

The susceptibility for **5.1** is corrected using the mean field approximation using Equation 5.3, where z is the number of interacting nearest neighbors and J' is the intermolecular coupling constant.

$$\chi_{corr.} = \frac{\chi_{tri}}{1 - \chi_{tri}\dfrac{2zJ'}{Ng^2\beta^2}} \tag{5.3}$$

The full Hamiltonian used to fit the data for **5.1** with julX is in Equation 5.4 where J, D, E, g, S, and B have the same definitions as in Equations 5.1 and 5.2.

$$\hat{H} = -2\sum_{i=1}^{ns-1}\sum_{j=+1}^{ns} J_{ij}\left(\hat{\mathbf{S}}_i \cdot \hat{\mathbf{S}}_j\right) + \sum_{i=1}^{ns} D_i\left[S_{z,i}^2 - \frac{1}{3}S_i(S_i+1) + \frac{E_i}{D_i}\left(S_{x,i}^2 - S_{y,i}^2\right)\right] + \sum_{i=1}^{ns} g\mu_B\hat{\mathbf{S}}_i \cdot \hat{\mathbf{B}}_i \tag{5.4}$$

Magnetic Measurements of 5.2 and 5.3

Magnetic susceptibility data were collected with a Quantum Design MPMS-XL SQUID magnetometer. Unaltered crystalline samples of **5.2** were loaded into a gelatin capsule and inserted into a drinking straw prior to analysis. The small kink in the $\chi_M T$ values for **5.2** at ~260 K does not occur for powdered samples encased in eicosane. Compared to eicosane-encased powder samples, we found that $\chi_M T$ values for **5.3** are not reproducible when unaltered crystalline or ground crystalline (powdered) samples were used. Torquing of the particles results in higher values during sample warming compared to cooling; it also masks the low temperature downturn in $\chi_M T$ resulting from anisotropy in the sample. Therefore, all analyses of **5.3** were performed with eicosane-encased samples. Finely ground samples were suspended in eicosane, loaded into a gelatin capsule and inserted into a drinking straw prior to analysis. Diamagnetic corrections were applied by using Pascal's constants and by subtracting the diamagnetic susceptibility from a sample holder with or without eicosane, as appropriate.

Susceptibility data were fit with theoretical models using a relative error minimization routine (julX 1.41).[18] Zero-field splitting parameters obtained with julX are based on the spin Hamiltonian in Equation 5.5 where D, E, g, S, and B have the same definitions as in Equation 5.2.

$$\hat{H} = \sum D_i \left[S_{z,i}^2 - \tfrac{1}{3} S_i \left(S_i + 1 \right) + E_i \big/ D_i \left(S_{x,i}^2 - S_{y,i}^2 \right) \right] + \sum g \beta \vec{S}_i \cdot \vec{B} \tag{5.5}$$

Fits of the magnetization data obtained with the ANISOFIT program[19] are based on the spin Hamiltonian in Equation 5.2. Fits of the magnetization data obtained with the MagSaki program[20] are based on the Hamiltonian in Equation 5.6.

$$H = -\left(\tfrac{3}{2} \right) \kappa \lambda \mathbf{L} \cdot \mathbf{S} + \beta \left[\left(-\tfrac{3}{2} \right) \kappa \mathbf{L} + g_e \mathbf{S} \right] \tag{5.6}$$

The program uses three parameters to fit the susceptibility data for mononuclear complexes: a spin-orbit coupling parameter (λ), an orbital reduction factor (κ) related to percent

electron delocalization from metal to ligand, and an axial splitting parameter (Δ), which represents the energy between states that arise from tetragonal distortions of octahedral geometry.[20-22]

5.4 Results & Discussion

Synthesis

The trinuclear manganous compound [Mn_3Cl_6(bispicen)$_2$] (**5.1**) serendipitously self-assembles by prolonged heating of a 2:3 mixture of bispicen and $MnCl_2$ in acetonitrile. Compound **5.2** has been prepared as pale pink crystals under N_2 by reaction of [Co{N(SiMe$_3$)$_2$}$_2$] with two equivalents of H$_2$ddfp, followed by addition of two equivalents of KN(SiMe$_3$)$_2$ and recrystallization from DME and hexanes. Cobalt-containing **5.2** is stable in an inert atmosphere and in various organic solvents, but yields a brown oil upon prolonged exposure to air. Iron-containing **5.3** was prepared by an analogous method, as previously reported.[16]

Crystal structures

The trinuclear **5.1** has an unusual asymmetric structure with scant chemical precedence.[12-13] The metal-ligand bond distances[17] and the anion count are consistent with three Mn(II) ions in the structure.[23] The Mn(II) ions are arrayed with a single chloride anion linking each pair of adjacent metal ions. The asymmetry results from different coordination spheres around the terminal Mn(II) ions (Figure 5.2): one is hexacoordinate while the other is tetracoordinate.

Compounds **5.2** and **5.3** each crystallized with tetracoordinate environments: the M(II) atom is at the center of inversion and lies within the mean {O$_4$} plane. The trans O–Co–O angle in **5.2** is 180°, leading to a τ_4 value of 0, indicating a perfect square-planar geometry. The structure of **5.3** is isostructural to **5.2**, again with $\tau_4 = 0$. There are no intramolecular axial contacts in **5.2** or

5.3 shorter than 3.1 Å and no intermolecular contacts shorter than 5.2 Å, demonstrating the four-

coordinate nature of these species.
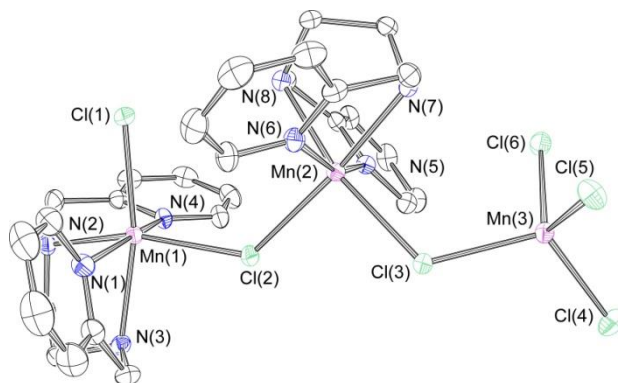
Figure 5.2. ORTEP representation of the crystal structure of **5.1**. All thermal ellipsoids are drawn at 50% probability. Hydrogen atoms are omitted for clarity. Reproduced from reference 17.

a)   b)
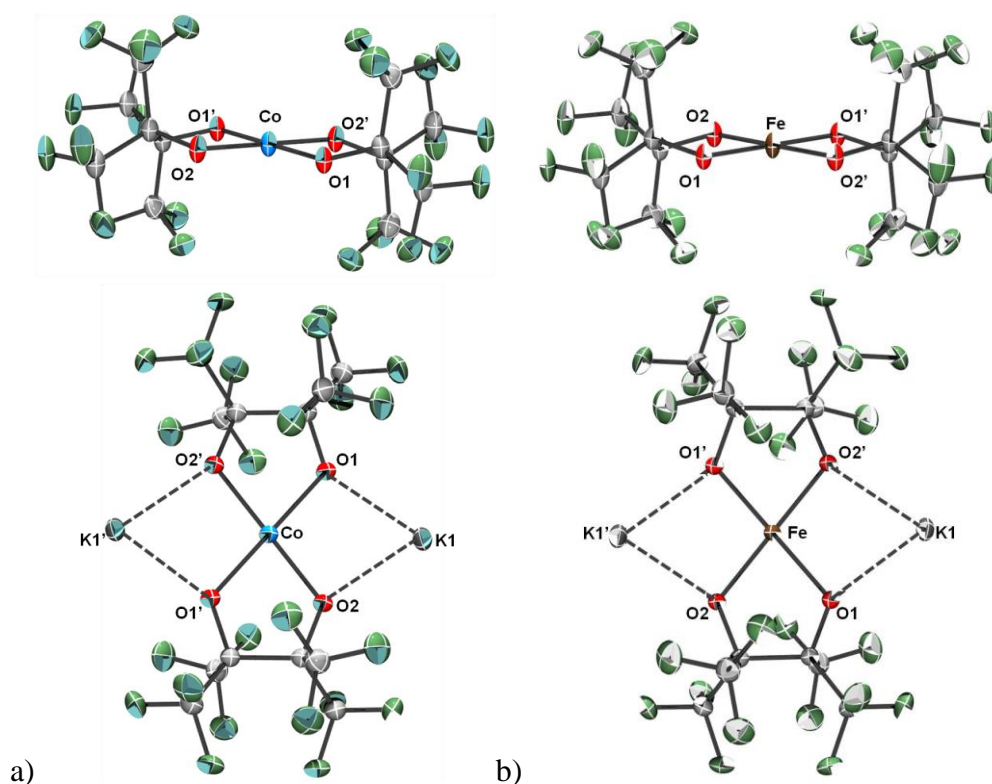
Figure 5.3. **a**) Top: ORTEP diagram of the anion of **5.2**. Bottom: ORTEP diagram of **5.2** showing K⋯O interactions. Solvent molecules removed for clarity. **b)** ORTEP diagram of the anion of **5.3**. Bottom: ORTEP diagram fo **5.3** showing K⋯O interactions. Ellipsoids for all atoms are shown at the 50% probability level. Reproduced from reference 16.

Magnetic Properties of 5.1

A plot of $1/\chi$ vs. T of **5.1** shows a linear relationship as predicted by the Curie-Weiss law with a negative Weiss constant (Figure 5.4a), which is consistent with net antiferromagnetic coupling in the compound. A fit of the data above 50 K gives a Weiss constant of $\Theta = -29.34$ K, and a Curie constant $C = 14.22$ emu·K·mol^{-1} ($R^2 = 0.99991$). Fitting the data above 100 K and 150 K gives similar values ($\Theta = -32.02$ K, $C = 14.37$ emu·K·mol^{-1} with $R^2 = 0.99996$ and $\Theta = -33.38$ K, $C = 14.45$ emu·K·mol^{-1} with $R^2 = 0.99996$, respectively). These values for the Curie constant are slightly larger than predicted by the Curie-Weiss law (13.125 emu·K·mol^{-1}).
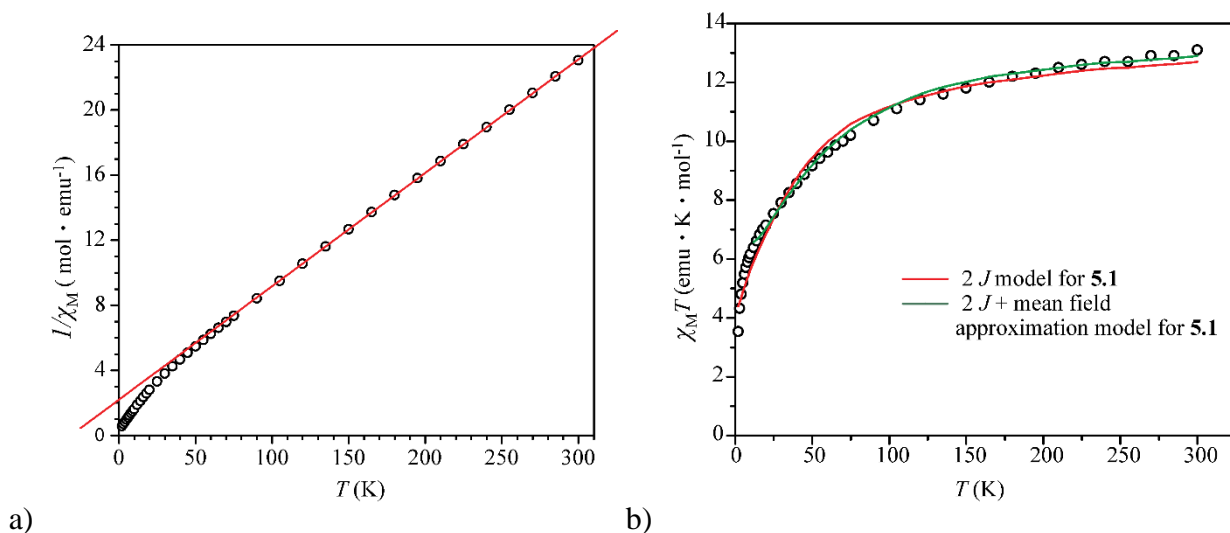
Figure 5.4. a) A plot of $1/\chi$ versus T for **5.1**. The red line is a linear fit of the data above 100 K. **b)** Magnetic behavior of **5.1** as measured at 1000 G. The solid lines represent calculated fits to the data; see text for details.

A plot of $\chi_M T$ vs. T for **5.1** is shown in Figure 5.4b. The $\chi_M T$ value at 300 K (13.03 emu·K·mol^{-1}) is close to, but slightly smaller than that predicted for three non-interacting high-spin Mn(II) ions (13.125 emu·K·mol^{-1}). As the temperature cools to 50 K, the value of $\chi_M T$ decreases gradually; further cooling causes $\chi_M T$ to decrease more rapidly to a minimum of 3.52 emu·K·mol^{-1} at 2 K. This value is smaller than that predicted for the $S = {}^5/_2$ ground state anticipated

for three antiferromagnetically coupled Mn(II) ions (4.375 emu·K·mol^{-1}), which may indicate either intermolecular interactions or perhaps the population of low-lying excited spin states.

Initial fits to the susceptibility data for **5.1** were attempted using julX and the Hamiltonian for a non-symmetrical trinuclear complex (Equation 5.1).[24] The most conservative fit (red trace, Figure 5.4) assumes that only intramolecular coupling between adjacent spin centers is operative, i.e. $J_{13} = 0$. Here, the best fit gives $J_{12} = -3.23$ cm^{-1} and $J_{23} = 0.63$ cm^{-1}, with all g values fixed at 2.00, and a fixed temperature-independent paramagnetism (TIP) value standard for three first-row transition metal ions (0.000600 emu·mol^{-1}). The associated f value (sum of the squared deviations) equals 0.3401. The fit can be improved moderately (reducing the f value) if TIP is allowed to increase from 0.000600 to ~0.004000 emu·mol^{-1} and approximately 10% paramagnetic impurities ($S = {}^{5}/_{2}$) are included in the refinement. While the latter is possible albeit unlikely, the former value is unreasonable for three high spin Mn(II) ions. Based on the J_{12} value, the interaction between Mn(1) and Mn(2) is predominantly antiferromagnetic; conversely, that between Mn(2) and Mn(3) is weakly ferromagnetic.
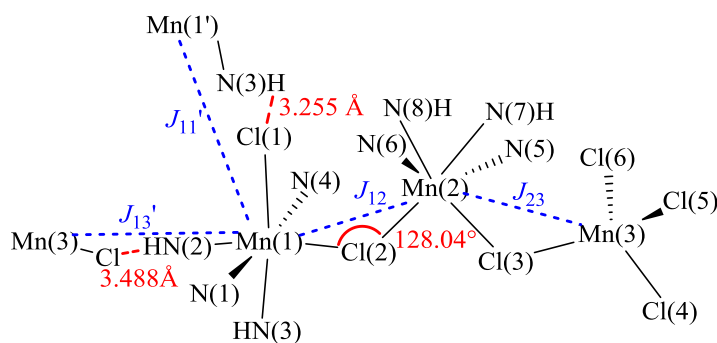
Figure 5.5. A schematic of potential coupling pathways are shown as blue dashed lines. Hydrogen bonds between the cluster and neighboring complexes are shown as red dashed lines.

Antiferromagnetic coupling between the octahedral Mn(II) ions (J_{12}, Figure 5.5) is expected based on the obtuse Mn-Cl-Mn bond angle of 128.04(2)°. This geometry allows significant orbital overlap between the Mn $3d$ orbitals and the Cl $3p$ orbitals, enabling an antiferromagnetic superexchange pathway.[25] The strength of the coupling is comparable to that observed in similar chloride-bridged Mn(II) complexes.[26-28] Conversely, the weaker ferromagnetic coupling between octahedral and tetrahedral Mn(II) ions (J_{23}) is consistent with orbital orthogonality arising from the different geometries of Mn(2) and Mn(3). The overlap between the tetrahedral Mn d orbitals and the Cl p orbitals is much weaker than for the octahedral Mn ion, therefore minimizing antiferromagnetic interactions. Meanwhile, the inverted orbital arrangement (see Figure 5.6) leads to a better energy match between the e and t_2 orbitals, which contributes to a ferromagnetic coupling.
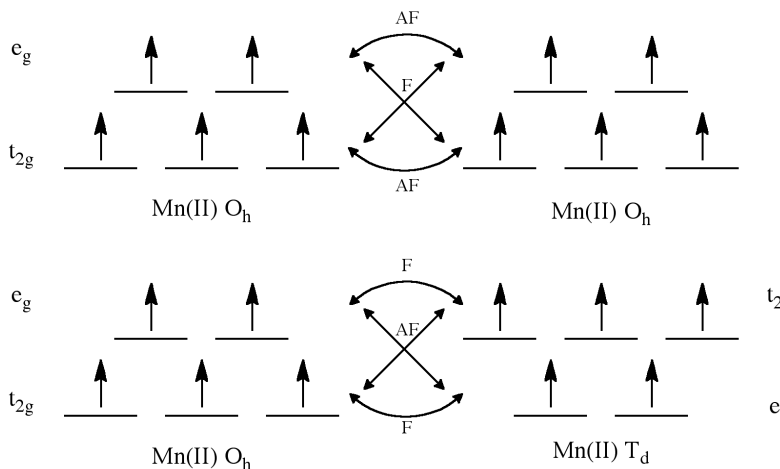
Figure 5.6. The ferromagnetic and antiferromagnetic coupling for Mn(II) ions based on orbital overlap between octahedral-octahedral (top) and octahedral-tetrahedral (bottom) energy levels.

The simple fit follows the gross features of the susceptibility data; however, visual inspection makes obvious the need for additional fitting parameters. We first consider *inter*molecular magnetic interactions. The trinuclear species has hydrogen bonding pathways in

two directions (Figure 5.5): an NH moiety on Mn(1) can interact with the Cl^- on a neighboring

Mn(3) to give chains of clusters and a potential intermolecular $J_{13'}$ coupling constant, while the Cl^-

on Mn(1) can interact with an NH moiety on a neighboring Mn(1) to give a 2D net of clusters and

a potential intermolecular $J_{11'}$ coupling constant. There is ample literature precedence for invoking

magnetic exchange via H-bonding interactions.[29-31]

The mean field approximation (Equation 5.3) was utilized to model intercluster

interactions.[32] With this correction, an improved fit ($f = 0.1277$, green trace in Figure 5.4b) is

obtained, which yields $J_{12} = -6.0$ cm^{-1}, $J_{23} = 3.5$ cm^{-1}, and $zJ' = 0.42$ cm^{-1}, with all g values fixed

at 2.00 and TIP set at $600{\times}10^{-6}$ emu·mol^{-1}. The positive value of zJ' suggests an overall

ferromagnetic interaction through the hydrogen bonds. The small magnitude of zJ' indicates that

either the intermolecular interactions are extremely weak, or that ferro- and antiferromagnetic

intercluster exchanges largely cancel each other. The fit is satisfactory down to 10 K. Below this

temperature, the small J values likely lead to a poorly isolated ground state and a potential for

magnetic anisotropy (D) that may be responsible for the more rapid downturn in $\chi_M T$.[33]

Magnetization measurements (Figure 5.7) argue for the presence of magnetic anisotropy

(D), as the magnetization values of isofield data are not superimposable, and do not fit the expected

Brillouin function for either of the possible ground states of $S = {}^5/_2$ or $S = {}^{15}/_2$. Although not

saturated even at 50 kG, the magnetization achieves a value of 7.94 μ_B at 2 K and 50 kG. This

indicates that even at high field and low temperature, the ground state is not well-isolated and a

low-lying excited state of differing spin is present. Not surprisingly, attempts to fit the data using

ANISOFIT and the Hamiltonian in Equation 5.2 provide extremely poor fits; the best fit yields D

$= 3.27$ cm^{-1} and $E = 0.00182$ cm^{-1}.

Nevertheless, this *D* value was used as a starting point for an alternative fit of the susceptibility data using julX and the Hamiltonian in Equation 5.4. The best fit for a "2*J* plus anisotropy model" (using three *D* parameters refined individually) gives $J_{12} = -5.828$ cm^{-1}, $J_{23} = 3.701$cm^{-1}, $g_1 = 2.021$, $g_2 = 2.051$, $g_3 = 1.998$, $D_1 = -9.794$ cm^{-1}, $D_2 = 3.088$ cm^{-1}, $D_3 = 17.197$ cm^{-1}, $E/D_1 = -0.062$, $E/D_2 = 0.243$, $E/D_3 = -0.123$ with no paramagnetic impurity present and TIP $= 741.4 \times 10^{-6}$ emu·mol^{-1} (shown as the red trace in Figure 5.5), with $f = 0.051$. Compared to the 2*J*-only fit, the magnetic coupling parameters are different in magnitude but still reasonable for Mn(II) ions bridged by chloride. Interestingly, the scalar average of the *D* values is 3.497 cm^{-1}, which is very similar to the values obtained from ANISOFIT for the magnetization data. The zero-field splitting values are probably not reliable owing to overparameterization, and the sign of *D* cannot be determined from fits to magnetization data. The overall quality of the fit suggests some validity in using an anisotropic model to fit the magnetic data. We note that all of the *D* values are much larger than would be expected for Mn(II) ions, where the high spin d^5 configuration leads to an isotropic A_1-type state both for tetrahedrally and octahedrally coordinated ions. We cannot rule out the possibility of molecular magnetic anisotropy arising from the anisotropic geometry of the complex. However, fits with the simpler 2*J*-only model are of comparable quality, so we conclude that the "2*J* + anisotropy" model is less reasonable.

We note that neither in-phase nor out-of-phase peaks are observed in an initial study of the variable temperature AC susceptibility, indicating that this complex does not exhibit slow relaxation of the magnetization, and therefore cannot be classified as a single-molecule magnet.
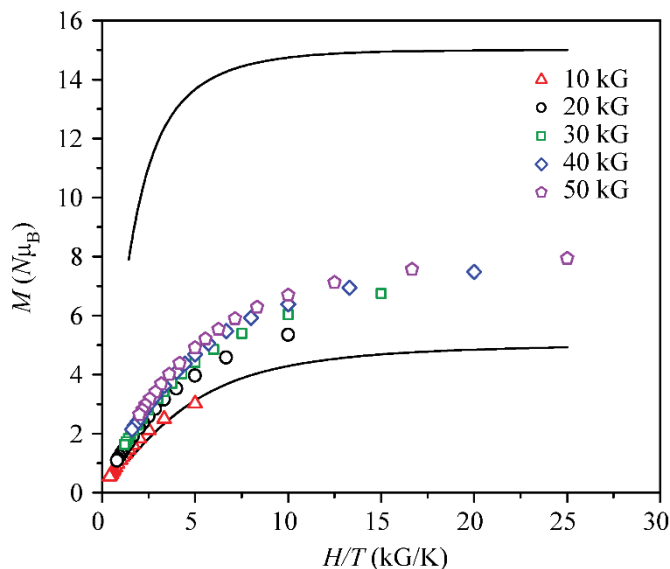
Figure 5.7. Temperature dependence of the magnetic susceptibility of **5.1**. The red line represents the "2*J* plus anisotropy" model fit. Inset: dependence of the complex's magnetization on reduced field, determined at measuring fields between 10 and 50 kG. Solid lines represent expected behavior for the $S = {}^5/_2$ and $S = {}^{15}/_2$ Brillouin functions.

*Magnetic Properties of **5.2** and **5.3***

The solution magnetic moments for **5.2** and **5.3** were determined via the Evans' method[34] to be 4.89 μ_B (2.99 emu·K·mol^{-1}) and 5.52 μ_B (3.81 emu·K·mol^{-1}), respectively, both larger than the spin-only values of 3.87 μ_B for $S = {}^3/_2$ (Co^{II}) and 4.89 μ_B for $S = 2$ (Fe^{II}). Both Co^{II} and Fe^{II} compounds are commonly observed to have orbital contributions to their magnetic susceptibilities.[35]

The temperature-dependent $\chi_M T$ data for zero-field cooled crystalline **5.2** are presented in Figure 5.8a. The room temperature value of 2.91 emu·K·mol^{-1} is larger than expected (1.875 emu·K·mol^{-1}) for the spin-only contributions of an $S = {}^3/_2$ complex with $g = 2.00$, but common for Co^{II}. The $\chi_M T$ value decreases gradually from 2.91 to 2.54 emu·K·mol^{-1} at 75 K, followed by a more rapid decrease to 1.76 emu·K·mol^{-1} at 5 K. Even at low temperature, the susceptibility values are not consistent with a low-spin $S = \frac{1}{2}$ ground state (expected 0.375 emu·K·mol^{-1}): others have

reported similar room temperature $\chi_M T$ values for tetrahedral $S = {}^3/_2$ complexes, but $\chi_M T \ll 1$ emu·K·mol^{-1} for $S = \frac{1}{2}$ complexes.[36] The decrease below 75 K is likely due to zero-field splitting and not a spin-state change.
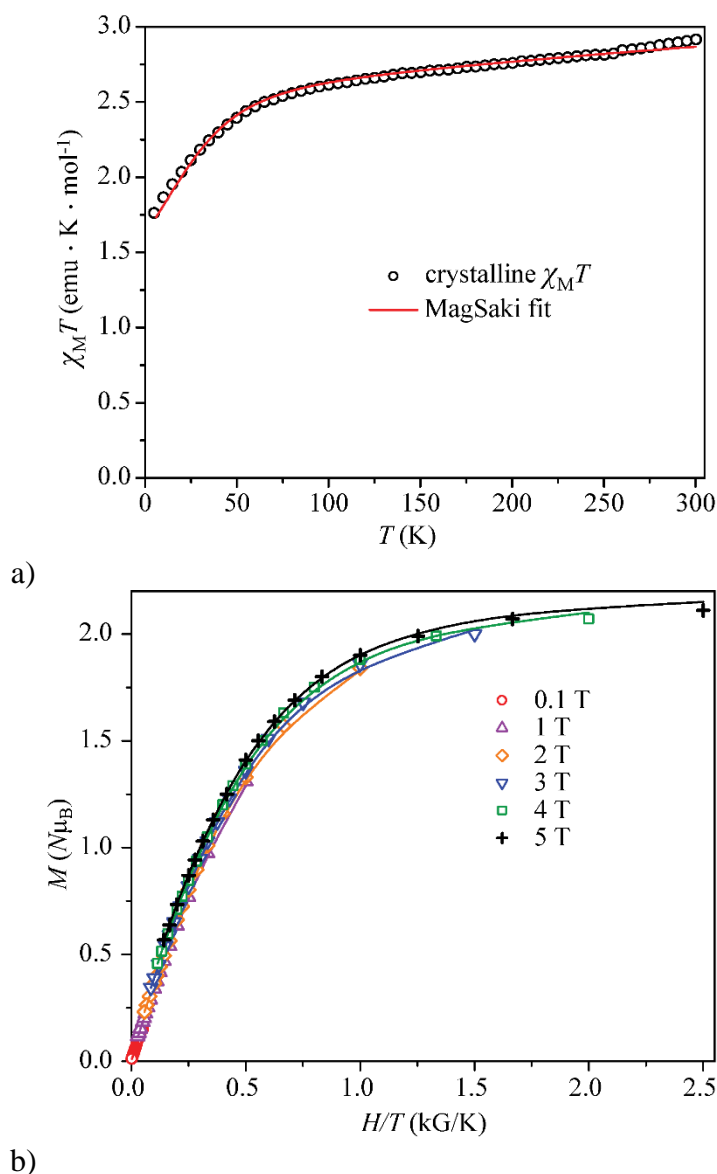
Figure 5.8. a) Temperature dependence of $\chi_M T$ for **5.2**, measured at 0.1 T. The best fit to the data obtained from MagSaki[20] is shown as a red line. Inset: reduced field dependence of the magnetization for **5.2** at three selected fields. Lines shown are guides for the eye. **b)** Reduced field dependence of the magnetization for **5.2** collected at six fields (0.1-5 T) and lines of best fit obtained from ANISOFIT.[19]

Low temperature magnetization data show near superposition of isofield lines (Figure 5.8b), and saturate at 2.1 Nμ_B. Since an unreasonably large average g value (>3.00) would be required to support an $S = \frac{1}{2}$ assignment, the magnetization saturation value is more consistent with assignment of an $S = \frac{3}{2}$ ground state.

Although orbital effects in Co(II) complexes complicate the determination of spin state from susceptibility data alone,[37] the data shown in Figure 5.8 are consistent with the maintenance of $S = \frac{3}{2}$ throughout the measured temperature range. The MagSaki[20] program was employed to fit the data for **5.2** to a high-spin, axially-distorted, Co(II) octahedral model, using the Hamiltonian in Equation 5.6.[21] Here, when $S = \frac{3}{2}$ and $g = 2.00$, a good fit ($R = 0.0004862$) is obtained for $\Delta = 850$ cm^{-1}, $\lambda = -127$ cm^{-1}, $\kappa = 0.93$ and TIP $= 411 \times 10^{-6}$ emu/mol (Figure 5.8a). For comparison, the free Co^{II} ion has $\Delta = 0$ cm^{-1}, $\lambda = -170$ cm^{-1}, and $\kappa = 1.00$. Compared to octahedral complexes with similar ligand field environments in the literature, **5.2** has a similar κ value, but a larger Δ value and a more positive λ value.

Interestingly, a large and positive Δ value is usually associated with tetragonally *compressed* octahedral Co^{II} complexes,[38] in which case the $^4A_{2g}$ ground term is well isolated from the ^4E_g excited state and zero-field splitting can be extracted from a straightforward spin Hamiltonian.[39] The curve shape of the $\chi_M T$ versus T plot are consistent with a positive Δ value, supporting the validity of a spin-only formalism.[38] Note that a comparable, albeit poorer, MagSaki fit to the susceptibility data uses a negative Δ value of ~ -550 cm^{-1}; in that case zero-field splitting parameters are not easily extracted from a spin-only Hamiltonian.[40]

Assuming $\Delta \gg 0$, fits to the susceptibility and magnetization data using $S = \frac{3}{2}$ models in the julX[18] and ANISOFIT[19] programs, respectively, give commensurate magnetic parameters with large |D| and |E| values, consistent with sizable axial and rhombic anisotropy. The julX[18] program

doesn't explicitly account for orbital contributions: the phenomenological parameters D, E and TIP (temperature independent paramagnetism) help fit the susceptibility curve but their physical meanings could be obscured. Meanwhile, it is important to note that parameters obtained from ANISOFIT[19] are most reliable when the ground state is well-isolated energetically, which may not be the case for **5.2**.

Magnetization data and fits are shown in Figure 5.8b. Assuming an $S = {}^3/_2$ ground state, ANISOFIT[19] gives fitted parameters $g = 2.40$, $D = 35.68$ cm^{-1} and $E = 14.81$ cm^{-1} ($f = 0.01055$). These were reported in our original report,[16] but an E/D ratio $> 1/3$ is physically meaningless (equivalent to redefining the axes). After redefining the axes, the fitted parameters are $g = 2.40$, $D = -40.06$ cm^{-1} and $E = 10.44$ cm^{-1} ($f = 0.01055$). The large E/D ratio observed corresponds to a significant rhombic zero-field splitting in addition to a substantial axial zero-field splitting indicated by large D. Holland and coworkers have observed similar behavior in low-coordinate, high-spin Fe(II) complexes, where the large E/D ratio manifests itself as nearly field-independent magnetization curves with saturation values significantly lower than expected given a $g \sim 2$.[41] Attempts to fit the data with an $S = \frac{1}{2}$ model result in unreasonably large g values.

Using the julX program[18] (Figure 5.9), fitting the data with $S = {}^3/_2$ and E/D constrained to 0.333 (for maximal rhombic zero-field splitting, as observed with ANISOFIT) produces a good fit ($f = 0.021$) with parameters $g = 2.34$, $D = 27.1$ cm^{-1}, and TIP $= 1064 \times 10^{-6}$ emu/mol. In contrast, an $S = \frac{1}{2}$ model affords poor agreement with the data. These values are in agreement with those obtained from ANISOFIT, including the unusually large D value (*vide supra*).
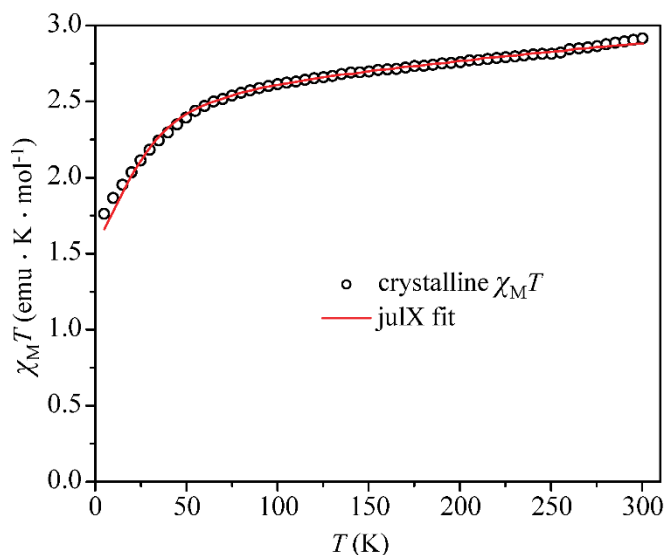
Figure 5.9. Plot of $\chi_M T$ versus T plot of for eicosane-encased powder sample of **5.2**, measured at 0.1 T. The best fit to the data obtained from julX is shown as a red line.

The large value for D illustrates a potential limitation of using a spin-only model for a Co(II) system. D (and to some extent, TIP) now encompasses the effect of orbital momentum and therefore is larger than expected for a similar system with no spin-orbit coupling.[24] Nevertheless, from the magnetic data, it is apparent that even at low temperature and high field, the spin state of the complex is **not** well described as $S = \frac{1}{2}$.

Temperature-dependent magnetic susceptibility data for powdered **5.3** encased in eicosane are presented in Figure 5.10a. Such sample treatment is required to avoid torquing of crystallites, even in fields as small as 0.1 T. The room temperature $\chi_M T$ value of 3.72 emu·K·mol^{-1} is larger than the spin-only value (3.00 emu·K·mol^{-1}) predicted for an $S = 2$ complex with $g = 2.00$. Like Co^{II}, spin-orbit coupling is common for Fe^{II}, so larger $\chi_M T$ values are frequently encountered. The $\chi_M T$ value decreases gradually from 3.72 to 3.46 emu·K·mol^{-1} at 55 K, followed by a downturn to 1.92 emu·K·mol^{-1} at 5 K, likely as a result of zero-field splitting.

a)

b)
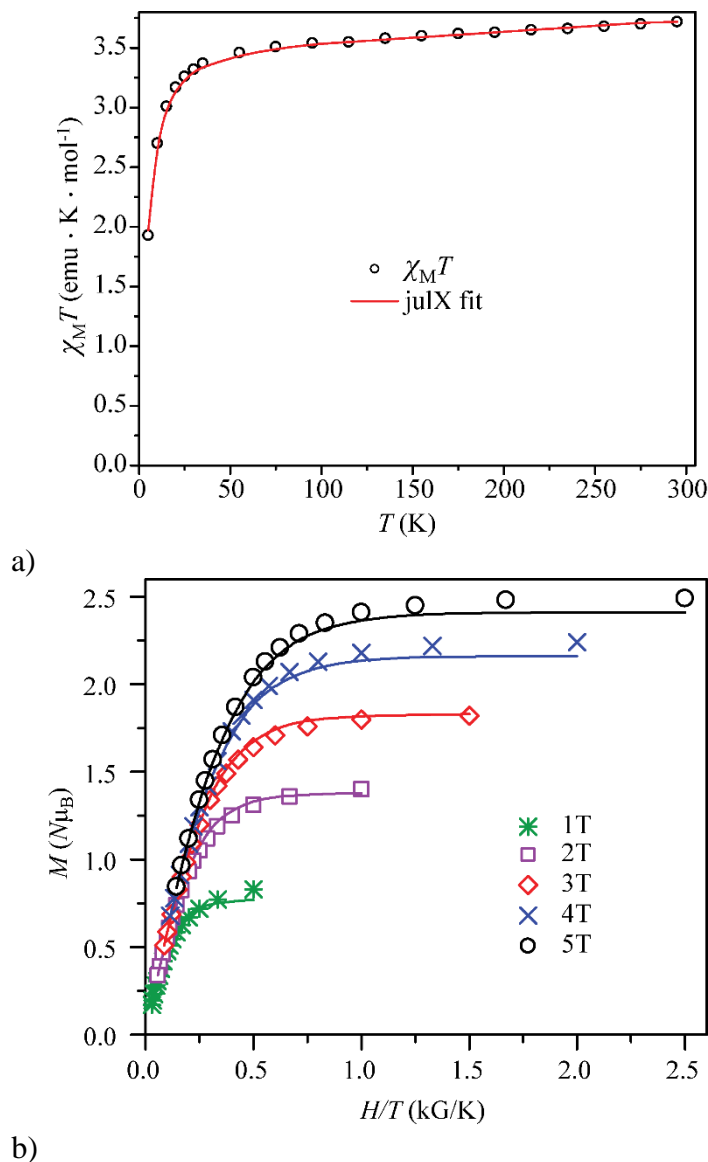
Figure 5.10. a) Temperature dependence of $\chi_M T$ for **5.3**, measured at 0.1 T. The best fit to the data is shown as a red line. **b)** Field dependence of the magnetization for **5.3**, measured at five fields. Best fits of the data are shown as solid lines. See text for details of the fitting procedures.

Magnetization data were also obtained for **5.3** at dc fields between 0.1 and 5 T (Figure 5.10b). The high-field magnetization saturates at 2.5 $N\mu_B$, lower than the 4 $N\mu_B$ expected for an isotropic system, but consistent with axial anisotropy. Using ANISOFIT,[19] fits with final parameters $g = 2.15$, $D = -11.93$ and $E = 1.47$ ($f = 0.023$) are obtained. Note that the best fits in ANISOFIT resulted from setting starting parameters such that $|E| < |D|$; when input parameters

123

have $|E| \approx |D|$, poor quality fits were obtained even after refinement to give fitted parameters such that $|E| < |D|$.

The anisotropy apparent in this complex is promising for possible single molecule magnet behavior. Therefore, we checked for frequency dependence in the out-of-phase susceptibility data (Figure 5.11). The out-of-phase susceptibility is weak for this complex, and shows no frequency dependence in the absence of an applied DC magnetic field. Typical DC magnetic field strengths for AC frequency dependence measurements are a few Oe; for **5.3**, even a 100 Oe DC field does not induce a frequency dependence. However, in the presence of a relatively large field, 1000 Oe, a frequency dependence is observed. The 200 Hz and 1400 Hz data at these temperatures show what appears to be the edge of a peak, likely centered at temperatures < 1.8 K. Therefore, it is possible that at an applied field and temperatures below 1.8 K, complex **5.3** could show the hysteresis characteristic of a single molecule magnet.
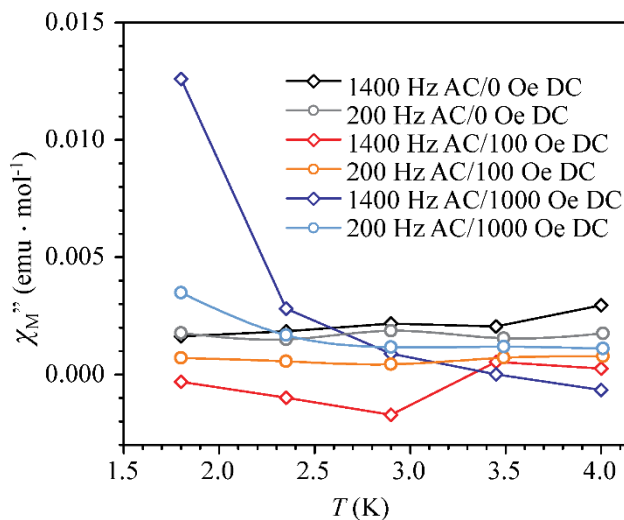
Figure 5.11. Frequency dependence of the out-of-phase susceptibility data for **5.3**. Each applied DC field, 0 Oe, 100 Oe, and 1000 Oe is shown at two switching frequencies: 200 Hz and 1400 Hz. Lines shown are guides to the eye.

5.5 Conclusion

The reported synthesis of **5.1**, while serendipitous, demonstrates that asymmetric trinuclear manganese complexes can assemble without the benefit of a complex ligand capable of bridging all three metal ions. The magnetic properties of **5.1** are consistent with an $S = 5/2$ system, suggesting that the interaction between the two octahedrally coordinated Mn(II) ions is antiferromagnetic; whereas, that between Mn(2) and the tetrahedrally coordinated Mn(3) is weakly ferromagnetic.

Attempts to optimize the fit are complicated by the presence of low-energy excited states and/or intermolecular interactions. Although a good fit to the susceptibility data can be obtained by considering intramolecular coupling between neighboring manganese atoms combined with single-ion anisotropy (D), the calculated anisotropy values are unreasonable and over-parameterization is likely. A modeling approach that disregards anisotropy but instead considers intermolecular interactions satisfactorily fits the data, but fails to provide a comprehensive model that fully accounts for the magnetization behavior. The weak nearest neighbor coupling proposed for **5.1** is common for Mn(II)-containing species and should facilitate the population of magnetic excited states.[7-8] The current model confirms the anticipated superexchange pathways, which endow **5.1** with an $S = {}^5\!/_2$ ground state.

In addition, we have reported novel examples of a square-planar high-spin $\{Co^{II}O_4\}$ and $\{Fe^{II}O_4\}$ coordination environments. The combination of high-spin electron configuration and square-planar geometry is confirmed by susceptibility and magnetization data. Preliminary studies suggest anisotropy may play a strong role in the magnetic properties of **5.2** and **5.3** with **5.3** showing some hallmarks of slow relaxation of magnetization.

5.6 Acknowledgements

CHAPTER 5 REFERENCES

1. Bhula, R.; Gainsford, G. J.; Weatherburn, D. C., *J. Am. Chem. Soc.* **1988**, *110*, 7550-7552.
2. Dimitrakopoulou, A.; Psycharis, V.; Raptopoulou, C. P.; Terzis, A.; Tangoulis, V.; Kessissoglou, D. P., *Inorg. Chem.* **2008**, *47*, 7608-7614.
3. Kessissoglou, D. P., *Coord. Chem. Rev.* **1999**, *185-6*, 837-858.
4. Lampropoulos, C.; Abboud, K. A.; Stamatatos, T. C.; Christou, G., *Inorg. Chem.* **2009**, *48*, 813-815.
5. Mukhopadhyay, S.; Mandal, S. K.; Bhaduri, S.; Armstrong, W. H., *Chem. Rev.* **2004**, *104*, 3981-4026.
6. Li, X. H.; Kessissoglou, D. P.; Kirk, M. L.; Bender, C. J.; Pecoraro, V. L., *Inorg. Chem.* **1988**, *27*, 1-3.
7. Kessissoglou, D. P.; Kirk, M. L.; Lah, M. S.; Li, X. H.; Raptopoulou, C.; Hatfield, W. E.; Pecoraro, V. L., *Inorg. Chem.* **1992**, *31*, 5424-5432.
8. Tangoulis, V.; Malamatari, D. A.; Spyroulias, G. A.; Raptopoulou, C. P.; Terzis, A.; Kessissoglou, D. P., *Inorg. Chem.* **2000**, *39*, 2621-2630.
9. Sobota, P.; Utko, J.; Szafert, S.; Janas, Z.; Glowiak, T., *J. Chem. Soc., Dalton Trans.* **1996**, 3469-3473.
10. Seela, J. L.; Knapp, M. J.; Kolack, K. S.; Chang, H. R.; Huffman, J. C.; Hendrickson, D. N.; Christou, G., *Inorg. Chem.* **1998**, *37*, 516-525.
11. Maspoch, D.; Gomez-Segura, J.; Domingo, N.; Ruiz-Molina, D.; Wurst, K.; Rovira, C.; Tejada, J.; Veciana, J., *Inorg. Chem.* **2005**, *44*, 6936-6938.
12. Aromi, G.; Gamez, P.; Krzystek, J.; Kooijman, H.; Spek, A. L.; MacLean, E. J.; Teat, S. J.; Nowell, H., *Inorg. Chem.* **2007**, *46*, 2519-2529.
13. Aromi, G.; Berzal, P. C.; Gamez, P.; Roubeau, O.; Kooijman, H.; Spek, A. L.; Driessen, W. L.; Reedijk, J., *Angew. Chem. Int. Ed.* **2001**, *40*, 3444-+.
14. Zheng, B.; Miranda, M. O.; DiPasquale, A. G.; Golen, J. A.; Rheingold, A. L.; Doerrer, L. H., *Inorg. Chem.* **2009**, *48*, 4274-4276.
15. Cantalupo, S. A.; Ferreira, H. E.; Bataineh, E.; King, A. J.; Petersen, M. V.; Wojtasiewicz, T.; DiPasquale, A. G.; Rheingold, A. L.; Doerrer, L. H., *Inorg. Chem.* **2011**, *50*, 6584-6596.
16. Cantalupo, S. A.; Fiedler, S. R.; Shores, M. P.; Rheingold, A. L.; Doerrer, L. H., *Angew. Chem. Int. Ed.* **2012**, *51*, 1000-1005.
17. Coates, C. M.; Fiedler, S. R.; McCullough, T. L.; Albrecht-Schmitt, T. E.; Shores, M. P.; Goldsmith, C. R., *Inorg. Chem.* **2010**, *49*, 1481-1486.
18. Bill, E. julX; Version 1.41; Max Planck Institute for Bioinorganic Chemistry, Mullheim an der Ruhr. http://ewww.mpi-muelheim.mpg.de/bac/logins/bill/julX_en.php; 2008.
19. Shores, M. P.; Sokol, J. J.; Long, J. R., *J. Am. Chem. Soc.* **2002**, *124*, 2279-2292.
20. Sakiyama, H. *MagSaki*, Sakiyama Laboratory: 2007.
21. Sakiyama, H., *J. Chem. Soft.* **2001**, *7*, 171-178.
22. Sakiyama, H.; Ito, R.; Kumagai, H.; Inoue, K.; Sakamoto, M.; Nishida, Y.; Yamasaki, M., *Eur. J. Inorg. Chem.* **2001**, 2027-2032.
23. Shannon, R. D., *Acta Crystallogr., Sect. A: Found. Crystallogr.* **1976**, *A32*, 751-767.
24. Kahn, O., *Molecular Magnetism*. VCH: New York, 1993.

25. Martin, J. D.; Hess, R. F.; Boyle, P. D., *Inorg. Chem.* **2004**, *43*, 3242-3247.
26. Boersma, F.; Tinus, A. M. C.; Kopinga, K.; Paduanfilho, A.; Carlin, R. L., *Physica B & C* **1982**, *114*, 231-237.
27. Kobayashi, H.; Tsujikawa, I.; Friedberg, S. A., *J. Low Temp. Phys.* **1973**, *10*, 621-633.
28. Simizu, S.; Chen, J. Y.; Friedberg, S. A., *J. Appl. Phys.* **1984**, *55*, 2398-2400.
29. Marvilliers, A.; Parsons, S.; Riviere, E.; Audiere, J. P.; Mallah, T., *Chem. Commun.* **1999**, 2217-2218.
30. Wu, J. Z.; Bouwman, E.; Mills, A. M.; Spek, A. L.; Reedijk, J., *Inorg. Chim. Acta* **2004**, *357*, 2694-2702.
31. Yan, B.; Wang, S. X.; Chen, Z. D., *Monatshefte fur Chemie* **2001**, *132*, 305-314.
32. Oconnor, C. J., *Prog. Inorg. Chem.* **1982**, *29*, 203-283.
33. Xu, J. X.; Ma, Y.; Liao, D. Z.; Xu, G. F.; Tang, J. K.; Wang, C.; Zhou, N.; Yan, S. P.; Cheng, P.; Li, L. C., *Inorg. Chem.* **2009**, *48*, 8890-8896.
34. Evans, D. F., *J. Chem. Soc.* **1959**, 2003-2005.
35. Miessler, G. L.; Tarr, D. A., *Inorganic Chemistry*. 3rd ed.; Pearson Prentice Hall: Upper Saddle River, NJ, 2004.
36. Carabineiro, S. A.; Silva, L. C.; Gomes, P. T.; Pereira, L. C. J.; Veiros, L. F.; Pascu, S. I.; Duarte, M. T.; Namorado, S.; Henriques, R. T., *Inorg. Chem.* **2007**, *46*, 6880-6890.
37. Krivokapic, I.; Zerara, M.; Daku, M. L.; Vargas, A.; Enachescu, C.; Ambrus, C.; Tregenna-Piggott, P.; Amstutz, N.; Krausz, E.; Hauser, A., *Coord. Chem. Rev.* **2007**, *251*, 364-378.
38. Titis, J.; Boca, R., *Inorg. Chem.* **2011**, *50*, 11838-11845.
39. Boca, R., Magnetic Functions Beyond the Spin-Hamiltonian. In *Magnetic Functions Beyond the Spin-Hamiltonian*, Mingos, D. M. P., Ed. 2006; Vol. 117, pp 1-264.
40. Boca, R., *Coord. Chem. Rev.* **2004**, *248*, 757-815.
41. Cowley, R. E.; DeYonker, N. J.; Eckert, N. A.; Cundari, T. R.; DeBeer, S.; Bill, E.; Ottenwaelder, X.; Flaschenriem, C.; Holland, P. L., *Inorg. Chem.* **2010**, *49*, 6172-6187.
42. Dahl, E. W.; Baddour, F. G.; Fiedler, S. R.; Hoffert, W. A.; Shores, M. P.; Yee, G. T.; Djukic, J. P.; Bacon, J. W.; Rheingold, A. L.; Doerrer, L. H., *Chem. Sci.* **2012**, *3*, 602-609.
43. Juhasz, G.; Matsuda, R.; Kanegawa, S.; Inoue, K.; Sato, O.; Yoshizawa, K., *J. Am. Chem. Soc.* **2009**, *131*, 4560-+.
44. Langley, S. K.; Stott, R. A.; Chilton, N. F.; Moubaraki, B.; Murray, K. S., *Chem. Commun.* **2011**, *47*, 6281-6283.

CHAPTER 6: EFFORTS TO CONTROL MAGNETIC COUPLING AND ANISOTROPY IN FE(III) MULTINUCLEAR COMPLEXES THROUGH LIGAND DESIGN

6.1 Introduction

Since the discovery of single molecule magnetic properties in the $Mn_{12}O_{12}$ complex,[1-2] reports of new complexes that display magnetic relaxation have been numerous. Many detail efforts to improve the operating temperature, through modification of either the total spin (*S*) or the anisotropy (*D*) of the complex. While the former is, in theory, straightforward to vary synthetically, the latter is more relevant, though quite difficult.[3] To this end, previous work in our group[4] investigated a series of mono-, di- and trinuclear Fe(III) ethynylbenzene-bridged complexes with geometrical constraints to tune the anisotropy and with binding sites reserved for building up the nuclearity. While the meta-bridged dinuclear Fe_2DEB (DEB = diethynylbenzene) and 1,3,5-bridged trinuclear Fe_3TEB (TEB = triethynylbenzene) complexes exhibit ferromagnetic coupling, poor metal–ligand overlap prevents the strong ferromagnetic coupling that we hypothesized. DFT studies suggest that orientation of the $Fe(dmpe)_2$ moiety reflects the orbital overlap: the dmpe ligands are oriented approximately perpendicular to the ethynyl-benzene plane, and thus the metal orbitals are not aligned in a way to allow for superexchange pathways through the ligand.

We predicted that the introduction of steric interactions would prevent the perpendicular orientation of the dmpe ligands and would encourage the dmpe ligands to orient parallel to the ethynyl benzene plane, corresponding to orbital overlap that allows for stronger magnetic coupling between Fe(III) centers. The steric bulk required to affect this change is not substantial: use of 1,3,5-trimethylbenzene (mesitylene) instead of benzene to synthesize a triethynylmesitylene (TEM) ligand should create enough steric interaction to alter the dmpe orientation (Figure 6.1).
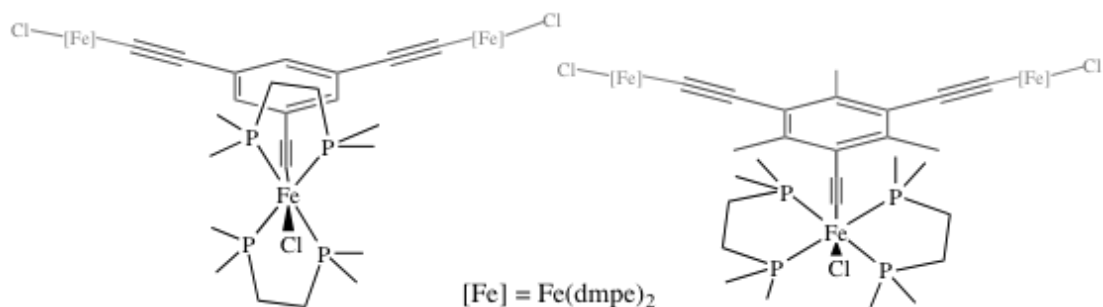
Figure 6.1. On the left, a perpendicular {Fe(dmpe)$_2$Cl} moiety arrangement, similar to that observed in the crystal structure of {Fe(dmpe)$_2$Cl}$_3$TEB(OTf)$_3$, and on the right, a parallel {Fe(dmpe)$_2$Cl} moiety arrangement, as is predicted for the crystal structure of {Fe(dmpe)$_2$Cl}$_3$TEM(OTf)$_3$.

Herein, we report the synthesis and characterization of a novel series of complexes using the ethynyl mesitylene ligand: [(dmpe)$_2$FeCl(MEM)] (**6.1**), [{(dmpe)$_2$FeCl}$_2$(DEM)] (**6.2**), [{(dmpe)$_2$FeCl}$_2$(μ_2-*m*-HTEM)] (**6.3**), [{(dmpe)$_2$FeCl}$_3$(μ_3-TEM)] (**6.4**), and the oxidized OTf – salt of each (**6.1·(OTf)**, **6.2·(OTf)$_2$**, **6.3·(OTf)$_2$**, and **6.4·(OTf)$_3$**). As predicted, the ethynyl mesitylene complexes orient the dmpe ligands in the plane with the mesitylene ligand core. As a result, stronger magnetic coupling is observed in the susceptibility data for the di- and tri-nuclear complexes. We further explored a subtraction method, which we use here to attempt to isolate the spin-only properties of these complexes that have spin and orbital contributions in the magnetic data.

6.2 Division of Labor

The H$_3$TEM and H$_2$DEM ligands were made by joint effort of Christina M. Klug and Stephanie R. Fiedler. Complexes **6.1** and **6.2** were synthesized and characterized by Christina M. Klug; synthesis and characterization, including crystal structure parameters, are presented here, with full details to be reported elsewhere.[5] Compound **6.3** was initially synthesized and characterized by Stephanie R. Fiedler, while Christina M. Klug attempted to optimize the reaction

conditions to purify the product. Compound **6.4** was initially synthesized and characterized by Stephanie R. Fiedler and reaction conditions optimized by Christina M. Klug and Andrew J. Stephan. Magnetic and structural characterizations presented here were performed by Stephanie R. Fiedler.

6.3 Experimental Section

Preparation of Compounds. Manipulations of iron complexes were performed inside a dinitrogen-filled glovebox (MBRAUN Labmaster 130) or on a Schlenk line using dinitrogen. All non-deuterated solvents were sparged with dinitrogen, passed over molecular sieves, and subjected to three freeze-pump-thaw cycles prior to use. The ligands 1,3,5-triethynylmesitylene (H$_3$TEM),[6] monoethynylmesitylene (HMEM),[7] and diethynylmesitylene (H$_2$DEM)[8] and the compound [Fe(dmpe)$_2$Cl$_2$][9] were synthesized according to the literature. Triethylamine (TEA) was distilled and stored in the glovebox. All other compounds and reagents were obtained commercially and used as received.

[(dmpe)$_2$FeCl(MEM)] **(6.1).** Monoethynylmesitylene (51 mg, 0.35 mmol) and [(dmpe)$_2$FeCl$_2$] (151 mg, 0.35 mmol) were dissolved in 15 mL of methanol, resulting in a forest green solution. Once all the reactants had dissolved, triethylamine (400 µL, 2.8 mmol) was added. The solution immediately became brown and after stirring for 5 minutes, an orange precipitate developed. The reaction was allowed to stir for one hour and then cooled to -40 °C for one hour to precipitate additional product. The precipitate was isolated by vacuum filtration and washed with pentane (3 × 3 mL). An orange solid was isolated (113 mg, 60% yield) and used without further purification. IR (KBr): $v_{C\equiv C}$ 2034 cm^{-1}. ESI-MS(+) (CH$_2$Cl$_2$): *m/z* 534.1 [(dmpe)$_2$FeCl(MEM)]$^+$, 499.2 [(dmpe)$_2$Fe(MEM)]$^+$. ^{1}H NMR (400 MHz, C$_6$D$_6$): δ 6.81 (s, 2 H, Ar-*H*), 2.42 (s, 6 H,

Ar–CH_3), 2.19 (s, 3 H, Ar–CH_3), 1.73 (m, 8 H, P–CH_2), 1.36 (m, 24 H, P–CH_3) ppm. ^{13}C NMR

was not obtained due to poor solubility. Elemental analysis was not determined for this compound;

it was used as-is based on MS and NMR data.

[(dmpe)$_2$FeCl(MEM)](OTf) (6.1·OTf). A solution of AgOTf (101 mg, 0.39 mmol) in 4

mL of acetonitrile was added to a suspension of [(dmpe)$_2$FeCl(MEM)] (113 mg, 0.21 mmol) in 12

mL of acetonitrile. The solution instantly turned green and was allowed to stir for one hour. The

reaction was filtered to remove silver metal, and the filtrate was concentrated to 2 mL. A green

solid was obtained by precipitation with diethyl ether (20 mL) and allowed to stir for one hour.

Green solid was isolated by vacuum filtration and recrystallized by diethyl ether diffusion into a

concentrated acetonitrile solution of the product (126 mg, 87 %). IR (KBr): $\nu_{C\equiv C}$ 2005 cm^{-1} ESI-

MS(+) (CH$_2$Cl$_2$): m/z 534.1 ([(dmpe)$_2$FeCl(MEM)])$^+$. ^{1}H NMR (400 MHz, CD$_2$Cl$_2$): δ 81.09,

51.57, 29.98, -19.17, -19.94, -21.64, -22.11 ppm. UV-vis(CH$_2$Cl$_2$) λ_{max}/nm (ε_M/M^{-1}·cm^{-1}) 298

(12800), 380 (4520), 427 (sh, 827), 598 (sh, 690), 690 (2700), 787 (11290). Anal Calcd for

C$_{24}$H$_{43}$ClF$_3$FeO$_3$P$_4$S$_1$: C, 42.15; H, 6.34. Found: C, 42.07; H, 6.35.

[(dmpe)$_4$Fe$_2$Cl$_2$(DEM)] (6.2). First, H$_2$DEM (28 mg, 0.17 mmol) and [(dmpe)$_2$FeCl$_2$] (148

mg, 0.35 mmol) were dissolved in 15 mL of methanol, resulting in a forest green solution. Once

all the reactants had dissolved, triethylamine (300 μL, 2.1 mmol) was added. The solution

immediately became brown and after stirring for 5 minutes, an orange precipitate developed. The

reaction was allowed to stir for 16 hours until a salmon precipitate formed. The precipitate was

isolated by vacuum filtration and washed with pentane (3 × 3 mL). A salmon colored solid was

isolated (128 mg, 81% yield) and used without further purification. IR (KBr): $\nu_{C\equiv C}$ 2023 cm^{-1}. ESI-

MS(+) (CH$_2$Cl$_2$): m/z 948.1 [(dmpe)$_2$FeCl(DEM)]$^+$. ^{1}H NMR (400 MHz, C$_6$D$_6$) δ ppm 6.81 (6.8s,

1 H, Ar-H), 2.70 (s, 3 H, Ar–CH_3), 2.39 (s, 6 H, Ar–CH_3), 1.75 (m, 16 H, P–CH_2), 1.39 (d, 48 H,

P–CH_3). ^{13}C NMR was not obtained due to poor solubility. Elemental analysis was not determined for this compound; it was used as-is based on MS and NMR data.

[(dmpe)₄Fe₂Cl₂(DEM)](OTf)₂ (6.2·(OTf)₂). A solution of AgOTf (101 mg, 0.39 mmol) in 5 mL of acetonitrile was added to a suspension of [(dmpe)₄Fe₂Cl₂(DEM)] (100 mg, 0.10 mmol) in 12 mL of acetonitrile. The solution instantly turned green and was allowed to stir for one hour. A green solid was obtained by precipitation with diethyl ether (20 mL) and allowed to stir for one hour. Green solid was isolated by vacuum filtration and recrystallized by diethyl ether diffusion into a concentrated methanolic solution of the product (112 mg, 85 %). IR (KBr): $\nu_{C\equiv C}$ 2000 cm^{-1} ESI-MS(+) (CH₂Cl₂): m/z 1097.1 ([(dmpe)₂FeCl(DEM)](OTf))$^+$. ^{1}H NMR (400 MHz, CD₂Cl₂): δ 123.6, 102.6, 53.1, -20.5, -23.1, -23.5 ppm. UV-vis(CH₂Cl₂) λ_{max}/nm (ε_M/M^{-1}·cm^{-1}) 302 (27780), 386 (7110), 433 (sh, 1900), 595 (sh, 1820), 688 (5500), 781 (19300). Anal Calcd for C₂₄H₄₃ClF₃FeO₃P₄S₁: C, 37.55; H, 5.98. Found: C, 37.26; H, 5.92.

[(dmpe)₄Fe₂Cl₂H(μ_2-m-HTEM)] (6.3). Freshly sublimed H₃TEM (35.87 mg, 0.187 mmol) and [(dmpe)₂FeCl₂] (164 mg, 0.39 mmol) were dissolved in methanol (24 mL). Once all the reactants had dissolved, triethylamine (420 μL, 3.0 mmol) was added. A precipitate formed immediately, and the reaction was allowed to stir for one hour. The reaction was vacuum filtered and the solid was washed with 12 mL of methanol and 8 mL of pentane. A tan solid was isolated (90 mg, 49% yield). The complex was used without further purification. IR (KBr): $\nu_{C\equiv C-H}$ 3305 cm^{-1} $\nu_{C\equiv C}$ 2029 cm^{-1}. ESI-MS(+) (CH₂Cl₂): m/z 972.0 ([(dmpe)₄Fe₂Cl₂(μ_2-m-HTEM)])$^+$, 582.1 ([(dmpe)₂FeCl(μ_2-m-HTEM)])$^+$ ^{1}H NMR (400 MHz, C₆D₆) d 3.10 (s, 1 H, –C≡C–H), 2.79 (s, 3 H, Ar–CH_3), 2.70 (s, 6 H, Ar–CH_3), 1.68 (m, 16 H, P–CH_2), 1.34 (s, P–CH_3), 1.27 (s, P–CH_3) ppm. ^{13}C NMR was not obtained due to poor solubility.

[(dmpe)₄Fe₂Cl₂H(*μ₂*-*m*-HTEM)](OTf)₂. (6.3·(OTf)₂) A solution of AgOTf (61 mg, 0.24 mmol) in 9 mL of acetonitrile was added to solid [(dmpe)₄Fe₂Cl₂(*μ₂*-*m*-HTEM)] (87 mg, 0.089 mmol). The solution instantly turned green and was allowed to stir for one hour. The reaction was filtered to remove silver metal, and the solvent was removed from the filtrate in vacuo. The resulting solid was triturated with diethyl ether (20 mL) for one hour. Green solid was isolated by vacuum filtration and recrystallized by diethyl ether diffusion into concentrated acetonitrile solution of the product. Despite attempts to control the product distribution by varying reaction time, solvent, or crystallization methods, NMR and ESI-MS of this product indicated a mixture of mononuclear and dinuclear products present. Results are presented here only to archive the data. IR (KBr): $\nu_{C≡C-H}$ 3250 cm^{-1} $\nu_{C≡C}$ 2010 cm^{-1} ESI-MS(+) (CH₂Cl₂): m/z 1120.9 ([(dmpe)₄Fe₂Cl₂(*μ₂*-*m*-HTEM)](OTf))$^+$, 582.1 ([(dmpe)₂FeCl(*μ₂*-*m*-HTEM)])$^+$ 487.0 ([(dmpe)₄Fe₂Cl₂(*μ₂*-m-TEM)])$^{2+}$. ¹H NMR (400 MHz, CD₂Cl₂): d 117.51, 97.45, 20.69, -20.57, -20.81, -23.36, -23.85. ppm. UV-vis(CH₂Cl₂) λ_{max}/nm (ε_M/M^{-1}·cm^{-1}) 299(22520), 398 (6080), 440 (sh, 1720), 598 (sh, 1750), 670 (5140), 764 (17750).

[(dmpe)₆Fe₃Cl₃(*μ₃*-TEM)] (6.4). A solution of H₃TEM (35.7 mg, 0.186 mmol) in 7 mL of ethanol was combined with a solution of [(Fe(dmpe)₂Cl₂] (260 mg, 0.61 mmol) in 15 mL of ethanol. After the addition of triethylamine (0.414 mL, 2.97 mmol) the orange-brown reaction turned green. The reaction slowly returned to a brown color and was refluxed overnight. A tan solid was removed and washed with ethanol. Evaporation of the mother liquor yielded an orange-brown solid, from which the product was extracted by stirring in tetrahydrofuran for one hour. After filtering and evaporating the solvent in vacuo, 140 mg (55%) of a salmon-colored solid was isolated. The ¹H NMR spectrum of this solid obtained in C₆D₆ indicated the presence of unreacted [Fe(dmpe)₂Cl₂]. The compound was used as-is without extensive characterization and purified in

the subsequent oxidation step. IR (KBr): $\nu_{C\equiv C}$ 2023 cm^{-1}. ESI-MS (C$_6$H$_6$/CH$_3$OH): 1361.7 [Fe$_3$(dmpe)$_6$Cl$_3$(μ_3-TEM)]$^+$, 1326.8 [Fe$_3$(dmpe)$_6$Cl$_2$(μ_3-TEM)]$^+$. ^{1}H NMR (400 MHz, C$_6$D$_6$) $d =$ 2.627 (s, 9H, Ar-CH_3), 1.749 (m, 24H, P-CH_2), 1.368 (s, 72H, P-CH_3) ppm. ^{13}C NMR (400 MHz, C$_6$D$_6$) 133.08 (C_{Ar}–CH$_3$), 126.99 (C_{Ar}–CC), 120.75 (C$_{Ar}$–CC–Fe), 31.03 (P–CH$_2$), 16.44 (P–CH$_3$), 13.87 (P–CH$_3$) ppm; not visible due to low solubility: (C$_{Ar}$–CC–Fe).

[(dmpe)$_6$Fe$_3$Cl$_3$(μ_3-TEM)](OTf)$_3$ (6.4·(OTf)$_3$). A solution of AgOTf (92 mg, 0.360 mmol) in 15 mL of acetonitrile was added to a solution of [(dmpe)$_6$Fe$_3$Cl$_3$(μ_3-TEM)] (140 mg, 0.103 mmol) in 45 mL of acetonitrile. The solution instantly changed color from orange to dark green and was stirred for one hour. The mixture was filtered to remove silver metal and the solvent was removed in vacuo. The resulting solid was tritured in tetrahydrofuran (~20 mL) for at least one hour. The solid was washed with diethyl ether and crystallized by ether diffusion into acetonitrile. Occasionally, large yellow crystals of [Fe(dmpe)$_2$(CH$_3$CN)Cl](OTf) (the solvate product formed from the unremoved Fe(dmpe)$_2$Cl$_2$ remaining, *vide supra*) formed and were removed manually. The crystal structure of these yellow crystals is presented in Appendix 2. Recrystallization of the remaining green solid from an ether diffusion into acetonitrile yielded pure green crystals. IR (KBr): $\nu_{C\equiv C}$ 1997 (cm^{-1}). ESI-MS (CH$_3$CN): 1659.5 [Fe$_3$(dmpe)$_6$Cl$_3$(μ_3-TEM)](OTf)$_2$$^+$, 1510.7 [Fe$_3$(dmpe)$_6Cl_3$($\mu_3$-TEM)](OTf)$^+$, 1362.6 [Fe$_3$(dmpe)$_6Cl_3$($\mu_3$-TEM)]·CH$_3CN^+$, 755.5 [Fe$_3$(dmpe)$_6Cl_3$($\mu_3$-TEM)](OTf)·CH$_3$CN^{2+}, 738.1 [Fe$_3$(dmpe)$_6Cl_2$($\mu_3$-TEM)](OTf)·CH$_3$CN^{2+}, 663.1 [Fe$_3$(dmpe)$_6Cl_2$($\mu_3$-TEM)]·CH$_3$CN^{2+}. ^{1}H NMR (400 MHz, CD$_2$Cl$_2$) d = 128.49, 111.41, 56.291, –20.84, –21.57, –23.16, –24.36 ppm. UV-vis (CH$_2$Cl$_2$) λ_{max}/nm (ε_M/M^{-1} cm^{-1}) 775 (15590). Anal. Calcd for C$_{54}$H$_{105}$Cl$_3$F$_9$Fe$_3$O$_9$P$_{12}$S$_3$: C, 35.81; H, 5.84. Found: C, 35.59; H, 5.89.

X-Ray Structure Determinations. Structures were determined for the compounds listed in Table 6.1. All single crystals were coated in Paratone oil prior to removal from the glovebox. The crystals were supported on Cryoloops before being mounted on a Bruker Kappa Apex 2 CCD diffractometer under a stream of cold dinitrogen. Data were collected with Mo Kα radiation and a graphite monochromator. Initial lattice parameters were determined from reflections harvested from 36 frames, and data sets were collected targeting complete coverage and 4-fold redundancy. Data were integrated and corrected for absorption effects with the Apex 2 software package.[10] Structures were solved by direct methods and refined with the SHELXTL software package.[11] Unless otherwise noted, thermal parameters for all fully occupied, non-hydrogen atoms were refined anisotropically. Hydrogen atoms were added at the ideal positions and were refined using a riding model where the thermal parameters were set at 1.2 times those of the attached carbon atom (1.5 times that for methyl protons). The structure of **6.4·(OTf)₃** contains two disordered molecules of acetonitrile, but the cationic complex and triflate anions are well-ordered. Structural parameters for **6.3·(OTf)₂** and [Fe(dmpe)₂(CH₃CN)Cl](OTf) are presented in Appendix 2.

Magnetic Susceptibility Measurements. All samples were prepared under a dinitrogen atmosphere. Finely ground samples were loaded into gelatin capsules and inserted into straws, which were sealed in a Schlenk tube prior to removal from the glovebox. Samples were quickly loaded to minimize exposure to air into a Quantum Design MPMS-XL SQUID magnetometer. Data were corrected for the magnetization of the sample holder by subtracting the susceptibility of an empty gelcap and for diamagnetic contributions of the sample by using Pascal's constants.[12] The absence of ferromagnetic impurities was confirmed by observing the linearity of a plot of magnetization vs. field at 125 K.

Other Physical Measurements. Infrared spectra were measured with a Nicolet 380 FT–IR using KBr pellets. Electronic absorption spectra were obtained in air-free cuvettes with a Hewlett-Packard 8453 spectrophotometer. 1H NMR spectra were recorded on a Varian instrument operating at 400 MHz. Cyclic voltammetry experiments were done in 0.1 M solutions of $(Bu_4N)PF_6$ in CH_2Cl_2 solvent. Cyclic voltammograms (CVs) were recorded with a CH Instruments potentiostat (model 1230A or 660C) using a Pt microelectrode working electrode, Ag/Ag$^+$ reference electrode, and Pt wire auxiliary electrode at a scan rate of 0.1 V/s. Reported potentials are referenced to the $[Cp_2Fe]^+/[Cp_2Fe]$ (Fc$^+$/Fc) redox couple and were determined by adding ferrocene as an internal standard at the conclusion of each electrochemical experiment. Elemental analyses were performed by Robertson Microlit Laboratories Inc. in Madison, NJ. Mass spectroscopy were measured with a Finnigan LCQ Duo mass spectrometer equipped with an electrospray ion source and a quadrupole ion trap mass analyzer. Electron paramagnetic resonance (EPR) spectra were measured using a continuous-wave X-band Bruker EMX 200U instrument equipped with a liquid nitrogen cryostat. To achieve a glass at low temperatures, the sample was dissolved in a 1:1 mixture of 1,2-dichloroethane: dichloromethane.

6.4 Results

Synthesis and characterization

Ferrous compounds **6.1**–**6.4** were synthesized in a manner analogous to that used for TEB complexes, with the only differences due to the solubility of the trinuclear ethynylmesitylene-containing complex. Mono- and dinuclear compounds **6.1** and **6.2** precipitated after stirring in methanol, however, dinuclear compound **6.3** precipitated instead of **6.4** regardless of concentration or how much [Fe(dmpe)$_2$Cl$_2$] starting material was used. In order to improve the solubility of **6.3**

in the reaction mixture and add the third Fe(II) center, it was necessary to either stir for ~45 days in methanol or to reflux the reaction in ethanol overnight. Even then, some solid, presumably mono- and dinuclear TEM complexes, was removed before isolating the product from solution. Furthermore, [Fe(dmpe)$_2$Cl$_2$] starting material is contained in the reaction solution based on ^{1}H NMR peaks; in this case the oxidation functions as a purification step as described below.

Table 6.1. Crystallographic data^a for compound **6.4·(OTf)$_3$**.

	6.4·(OTf)$_3$
formula	$C_{62}H_{111}Cl_3F_9Fe_3N_3O_{9.50}P_{12}S_3$
fw	1963.26
color, habit	green plates
T, K	120(K)
space group	P $\bar{1}$
Z	2.0
a, Å	17.5664(12)
b, Å	17.7695(13)
c, Å	17.8248(12)
α, deg	71.593(2)
β, deg	88.531(2)
γ, deg	61.115(2)
V, Å^3	4568.3(6)
d_{calc}, g/cm^3	1.427
GooF	1.039
$R_1(wR_2)^b$, %	4.73 (11.38)

^{a} Obtained with graphite-monochromated Mo Kα (λ = 0.71073 Å) radiation.
^{b} $R_1 = \Sigma||F_o| - |F_c||/\Sigma|F_o|$,
$wR_2 = \{\Sigma[w(F_o^2 - F_c^2)^2]/\Sigma[w(F_o^2)^2]\}^{1/2}$ for $F_o > 4\sigma(F_o)$.
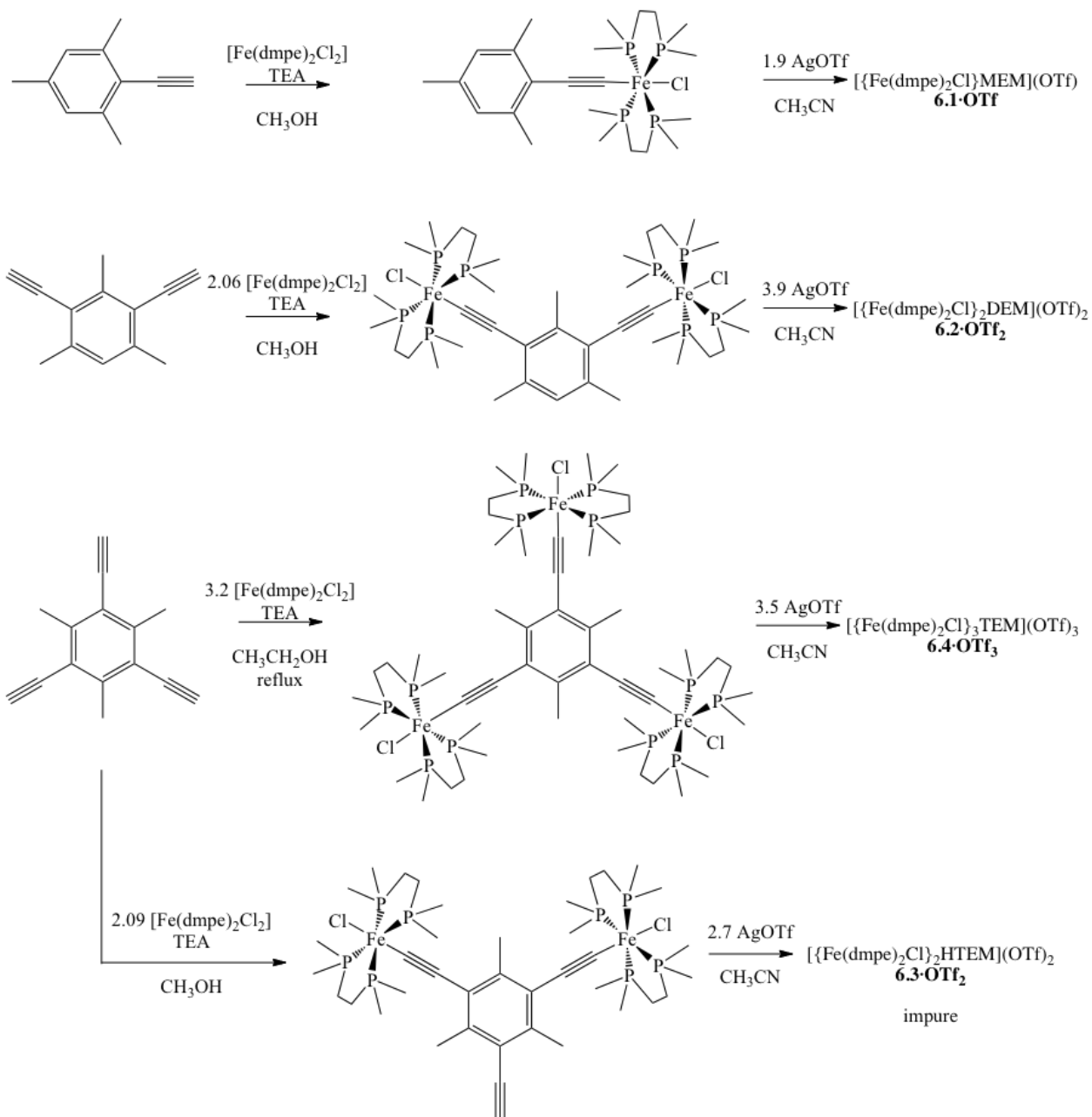
Figure 6.2. Syntheses of **6.1**, **6.2**, **6.4** and OTf⁻ salts of each.

The oxidation of each compound proceeded cleanly by use of silver triflate (AgOTf) in acetonitrile. Crystals of **6.1·(OTf)** and **6.4·(OTf)₃** were obtained by slow diffusion of ether into acetonitrile while crystals of **6.2·(OTf)₂** were obtained by slow diffusion of ether into methanol. Attempts to crystallize **6.3·(OTf)₂** yielded crystals of the dinuclear complex, but mass

spectroscopy and elemental analysis indicated mononuclear product still contaminated the bulk sample. Crystals of **6.4·(OTf)₃**, **6.2·(OTf)₂** and **6.1·OTf**, however, suggest that in each of these cases, a single product was formed. The focus of results presented here will be on **6.4·(OTf)₃** and comparisons to the trinuclear ferric TEB complex;[4] magnetic properties of compounds prepared by C. M. Klug will be presented elsewhere.[5]

a)

b)
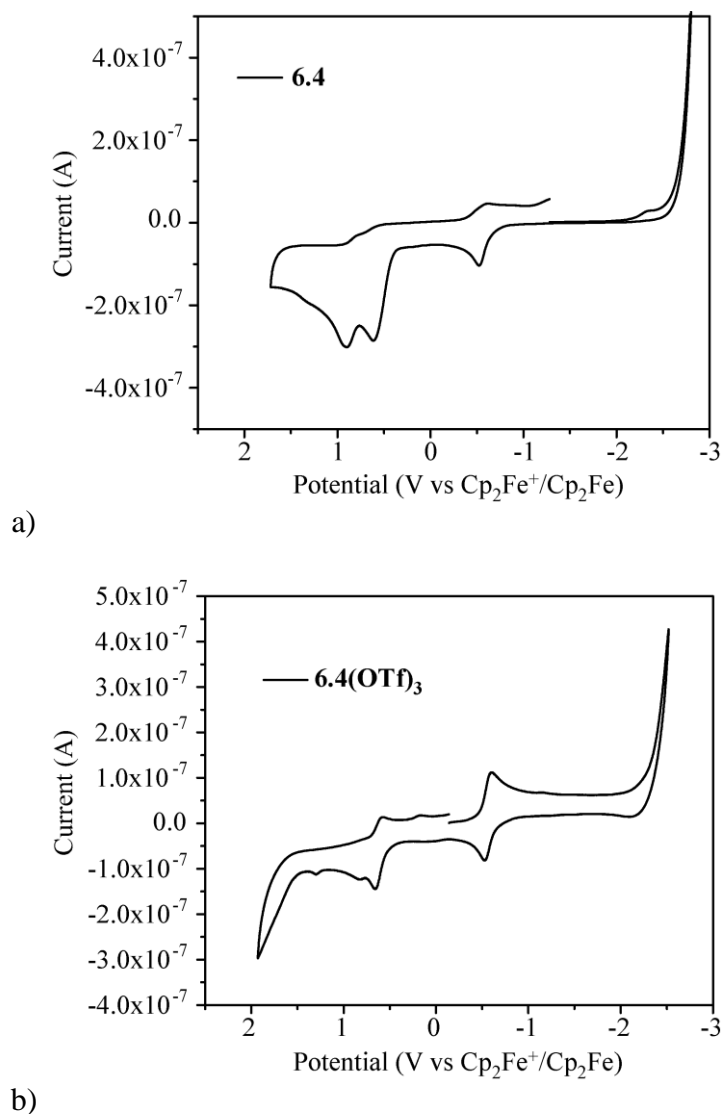
**Figure 6.3.** Cyclic voltammetry collected of compounds **6.4** and **6.4·(OTf)₃**.

Cyclic voltammetry performed on **6.4** and **6.4·(OTf)₃** (Figure 6.3) are consistent with those previously observed for acetylide-bridged Fe(II) and Fe(III) complexes.[13-16] The reversible one-electron wave observed at –0.56 eV corresponds to the Fe(III)/Fe(II) redox couple and the non-reversible wave observed at 0.632 eV corresponds to a Fe(IV)/Fe(III) couple. Though there are peaks due to contaminants in each sample, these waves are consistent, and the open-circuit potential reflects the change in oxidation state from **6.4** to **6.4·(OTf)₃**. The waves are observed as broad peaks with small shoulders indicating weak coupling, which are reminiscent of multinuclear TEB-containing complexes.[4] In our case, the CV of **6.4** shows some additional peaks, likely due to the impure nature of the product. The CV of **6.4·(OTf)₃** shows similar redox waves with a different open circuit potential, reflecting the oxidation from Fe(II) to Fe(III).

Crystal structures

The crystal structures of **6.3·(OTf)₂** and **6.4·(OTf)₃** reported here show iron in a distorted octahedral environment made up of bidentate dmpe ligands in equatorial positions and an acetylide or chloride in the axial positions. The acetylide bonds in **6.3·(OTf)₂** and **6.4·(OTf)₃** are slightly bent away from linearity. As a result, the molecules in **6.4·(OTf)₃** deviate from a perfect planar geometry to have a slight bowl-shape for each. The packing of this molecule is arranged with two molecules rotated 180° from another and offset such that the Fe(dmpe)₂Cl group of one molecule fits into the "bowl" of the other (Figure 6.4).

The orientation of the dmpe ligands is indicated by φ, which is the torsion angle defined by the dmpe centroid—Fe—$C_{mesityl}$—α-$C_{mesityl}$, as described previously (Figure 6.6).[4] A φ angle of 90° corresponds to dmpe ligands perpendicular to the plane of the aromatic ring and a φ angle of 0° corresponds arrangement of the dmpe ligands in the plane of the aromatic ring. Comparisons of

the trinuclear TEM complex with the trinuclear TEB complex are found in Table 6.2 and indicate

a similar structure with very slightly longer Fe–C bonds, slightly longer Fe···Fe distances, and a

Fe(dmpe)₂ moiety rotated by ~90° in **6.4·(OTf)₃**.
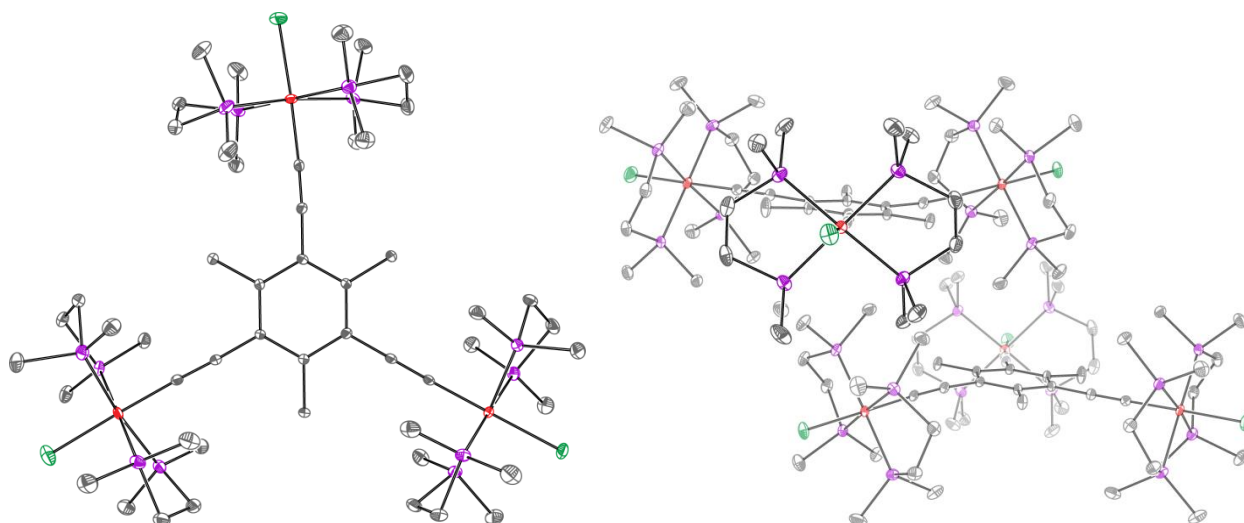
Figure 6.4. The crystal structure of **6.4·(OTf)₃**: on left, illustrating the trinuclear spacing and on right a partial packing plot to illustrate the intermolecular stacking and {Fe(dmpe)₂} orientation in **6.4·(OTf)₃**. Carbon, chlorine, iron and phosphorus are rendered as grey, green, red and purple ellipsoids, respectively. Hydrogen atoms are omitted for clarity. Ellipsoids are drawn at the 40% probability level.
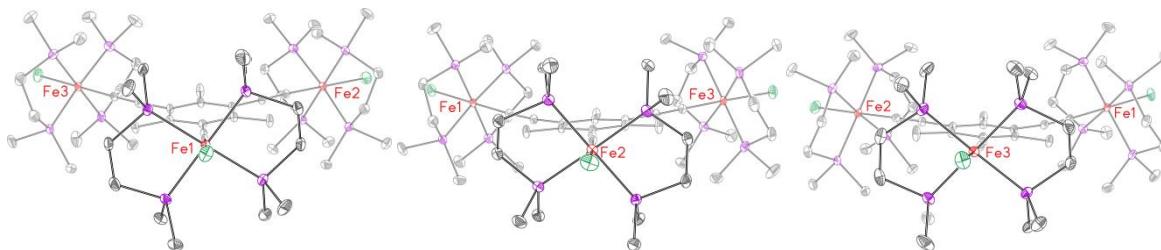
Figure 6.5. Orientation of the dmpe ligands at each Fe(II) center in **6.4·(OTf)₃**. Carbon, chlorine, iron and phosphorus are rendered as grey, green, red and purple ellipsoids, respectively. Hydrogen atoms are omitted for clarity. Ellipsoids are drawn at the 40% probability level.

Table 6.2. Comparisons of structural parameters between [{(dmpe)$_2$FeCl}$_3$TEB](OTf)$_3$ and [{(dmpe)$_2$FeCl}$_3$TEM](OTf)$_3$ (**6.4·(OTf)₃**).

	[{(dmpe)$_2$FeCl}$_3$TEB](OTf)$_3$	[{(dmpe)$_2$FeCl}$_3$TEM](OTf)$_3$ (**6.4·(OTf)₃**)
Fe–C$_{avg}$	1.876(6) Å	1.888(3) Å
φ Fe$_1$	36.9°	4.1°
φ Fe$_2$	82.2°	9.4°
φ Fe$_3$ (Fe$_{2a}$)[a]	82.2°	5.2°
Fe$_1$···Fe$_2$	10.184(1) Å	10.353(1) Å
Fe$_1$···Fe$_3$ (Fe$_{2a}$)[a]	10.184(1) Å	10.3820(8) Å
Fe$_2$···Fe$_3$ (Fe$_{2a}$)[a]	10.389(1) Å	10.0856(7) Å

[a]Due to crystallographic symmetry, the TEB complex only contains two unique iron centers: Fe$_2$ and Fe$_{2a}$. Fe$_3$TEM, on the other hand contains three crystallographically unique iron centers.
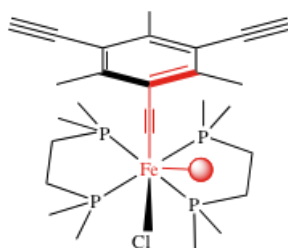
**Figure 6.6.** The torsion angle used to define φ, outlined in red.

Magnetic Properties

Several attempts to collect $\chi_M T$ vs T data for **6.4·(OTf)₃** are shown in Figure 6.7. Though these data show the same general trend, a decrease in $\chi_M T$ from ~300–100 K followed by a slight gradual increase and then a small downturn due to magnetic anisotropy, the quantitative values are only similar below 100 K. At low temperature, the deviations are likely due to differences in solvation of the samples. Because two acetonitrile co-crystallize, crystalline samples that are exposed to the dry glove box atmosphere could desolvate. On the other hand, crystals that are not dried thoroughly could have excess solvent trapped in them, especially in the eicosane-encased samples, which will make desolvation more difficult.

Above 100 K, several factors could affect the different data trends observed. Firstly, a ferromagnetic impurity could account for a $\chi_M T$ value that increases dramatically to values much higher than expected. We were able to rule this out for our samples by confirming that a plot of M vs H is linear for all samples; therefore, the samples only contain paramagnetic contributions. Secondly, values larger than the spin-only value are often observed for complexes that have orbital contributions, as octahedral, low-spin Fe(III) does. The increase above 100 K could be attributed to that, though it does not explain why there would be such dramatic differences from one sample to another. Thirdly, the experimental technique used to collect these data made use of rapid temperature changes with little equilibration time; though the SQUID reached a stable temperature, the thermal equilibrium within the sample may vary from one run to the next. As a result, the $\chi_M T$ values at higher temperatures, where the temperature step size is largest, show the largest variations. Lastly, the orientation of the particles in the sample are likely affecting the $\chi_M T$ values. Any preferential, even accidental, orientation of the particles, crystalline or other wise, with the magnetic field would result in a $\chi_M T$ value higher than expected. This would explain why different samples prepared in different ways give different results.

The raw data used for further analyses is the powder sample shown by blue crosshairs in Figure 6.7. This sample was ground, which removes possible alignment of the molecular species due to crystal packing. Encasing the same sample in eicosane does introduce another factor that could affect the orientation of the particles, but it lessens the possibility of particle torquing at low temperatures allowing us to better compare $\chi_M T$ values in that region. The data is qualitatively reproducible compared to other samples, especially at low temperature, which is where magnetic coupling can predominate over thermal fluctuations, and thermal equilibrium is more consistent (*vide supra*).
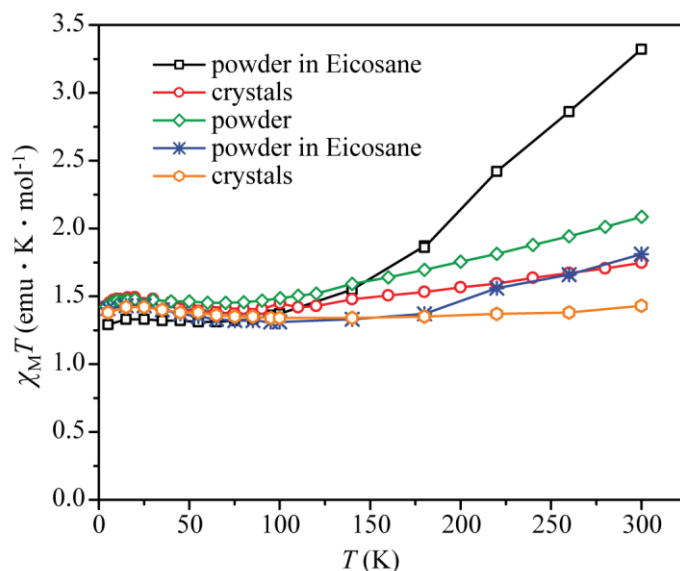
Figure 6.7. $\chi_M T$ vs T data for several preparations of **6.4·(OTf)$_3$**.

The $\chi_M T$ vs T data of the ground sample of **6.4·(OTf)$_3$** is shown again in Figure 6.8. The $\chi_M T$ shows a room temperature value of 1.81 emu·K·mol^{-1}, which decreases rather sharply to a minimum at 1.31 emu·K·mol^{-1} near 90 K and then exhibits a rounded maximum of 1.43 emu·K·mol^{-1} near 20 K before decreasing slightly at 5 K. In an attempt to consider the spin-only portion of the susceptibility data, we performed a correction on the obtained susceptibility data. From the $\chi_M T$ data of **6.4·(OTf)3**, we subtracted the $\chi_M T$ of **6.1·(OTf)** (blue crosshairs in Figure 6.8) and two times the susceptibility of [Fe(dmpe)$_2$(CCSi(CH$_3$)$_3$)Cl](PF$_6$) in order to remove the orbital contributions coming from the ligand (included in **6.1·(OTf)**) as well as three Fe(III)(dmpe)$_2$Cl groups. Then, three times the spin-only value of $\chi_M T$ for an $S = \frac{1}{2}$ system ($g =$ 2.15 based on EPR for the TEB analogue,[4] 0.433 emu·K·mol^{-1}) was added. The resulting corrected data is shown as red diamonds in Figure 6.8.

Attempts to fit this data were unsuccessful; after correction, the room temperature value of 0.59 emu·K·mol^{-1} is lower than the spin-only value for three $S = \frac{1}{2}$ centers so julX[17] is unable to provide an adequate fit to the data. However, we can qualitatively compare the data to the previous

145

TEB-containing complex, which was corrected in a similar way. Though the values for the two $\chi_M T$ plots are different, the trends are the same: as temperature decreases, $\chi_M T$ increases, indicating ferromagnetic coupling. Interestingly, the amount of increase for the two complexes is similar: $[\{Fe(dmpe)_2Cl\}_3TEB](OTf)_3$ increases from 0.99 emu·K·mol^{-1} to 1.91 emu·K·mol^{-1} while **6.4·(OTf)₃** increases from 0.59 emu·K·mol^{-1} to 1.45 emu·K·mol^{-1}.
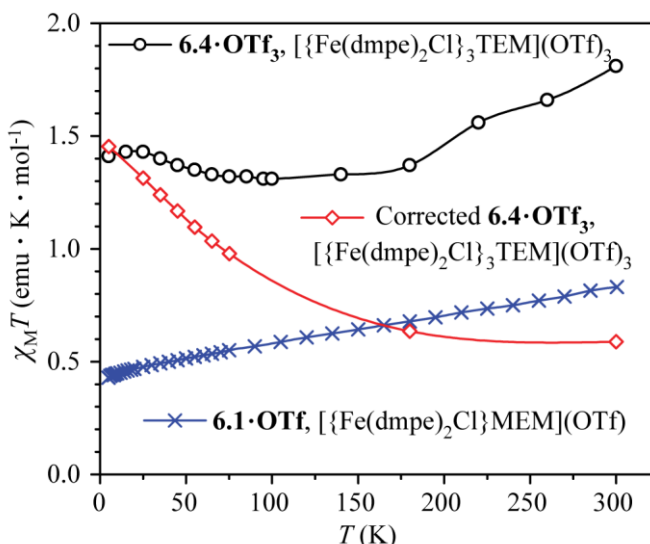
Figure 6.8. The raw $\chi_M T$ vs T data for **6.4·(OTf)₃** (black circles) and corrected $\chi_M T$ vs T data for **6.4·(OTf)₃** (red diamonds). Blue crosshairs represent the data for **6.1·(OTf)**, which were subtracted. Lines are guides to the eye.

Based on the variation observed in data in Figure 6.7, the low temperature data here is most reliable for comparisons to the $[\{Fe(dmpe)_2Cl\}_3TEB](OTf)_3$ complex. Below 100 K, the data for each begins to increase more rapidly as temperature is decreased. The increase is slightly more gradual for $[\{Fe(dmpe)_2Cl\}_3TEB](OTf)_3$ than for **6.4·(OTf)₃** (Figure 6.9), which suggests slightly weaker coupling at low temperatures for $[\{Fe(dmpe)_2Cl\}_3TEB](OTf)_3$ than **6.4·(OTf)₃**

.
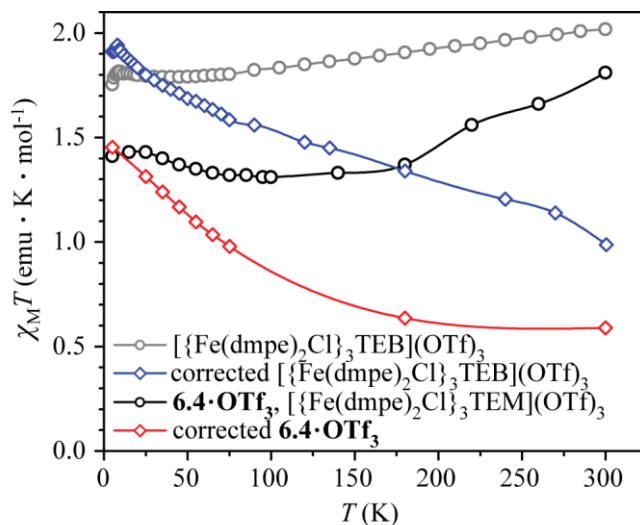
Figure 6.9. A comparison of the $\chi_M T$ vs T data for the previous [{Fe(dmpe)$_2$Cl}$_3$TEB](OTf)$_3$ complex (blue diamonds), the corrected data of [{Fe(dmpe)$_2$Cl}$_3$TEB](OTf)$_3$ (grey circles) with the current $\chi_M T$ vs T data for **6.4·(OTf)$_3$** (red diamonds) and the corrected data of **6.4·(OTf)$_3$** (black circles). Lines shown are guides to the eye.

6.5 Conclusions

Herein, we have reported a structural modification of a previous complex with the hopes of using ligand geometry to tune magnetic properties. The triethynyl mesitylene ligand introduces steric interactions that result in an {Fe(dmpe)$_2$} orientation that has previously been suggested to result in strong magnetic coupling through optimized orbital overlap. Our analysis of the magnetic parameters has been complicated by difficulty in obtaining reproducible data, however, the qualitative trend we observe suggests stronger coupling is present in the new compound **6.4·(OTf)$_3$** relative to [{Fe(dmpe)$_2$Cl}$_3$TEB](OTf)$_3$.

6.6 Acknowledgements

CHAPTER 6 REFERENCES

1. Lis, T., *Acta Crystallogr., Sect. B: Struct. Sci* **1980**, *36*, 2042-2046.
2. Sessoli, R.; Gatteschi, D.; Caneschi, A.; Novak, M. A., *Nature* **1993**, *365*, 141-143.
3. Neese, F.; Pantazis, D. A., *Faraday Discuss.* **2011**, *148*, 229-238.
4. Hoffert, W. A.; Rappe, A. K.; Shores, M. P., *J. Am. Chem. Soc.* **2011**, *133*, 20823-20836.
5. Fiedler, S. R.; Klug, C. M.; Shores, M. P., *In Preparation* **2013**.
6. Ohshiro, N.; Takei, F.; Onitsuka, K.; Takahashi, S., *J. Organomet. Chem.* **1998**, *569*, 195-202.
7. Ishihara, K.; Kobayashi, J.; Nakano, K.; Ishibashi, H.; Yamamoto, H., *Chirality* **2003**, *15*, 135-138.
8. Vicente, J.; Chicote, M. a. T.; Alvarez-Falcón, M. M.; Abrisqueta, M. a.-D.; Hernández, F. J.; Jones, P. G., *Inorg. Chim. Acta* **2003**, *347*, 67-74.
9. Girolami, G. S.; Wilkinson, G.; Galas, A. M. R.; Thorntonpett, M.; Hursthouse, M. B., *J. Chem. Soc., Dalton Trans.* **1985**, 1339-1348.
10. *APEX 2*. Bruker Analytical X-Ray Systems, Inc: Madison, WI, 2008.
11. Sheldrick, G., *Acta Crystallographica Section A* **2008**, *64*, 112-122.
12. Kahn, O., *Molecular Magnetism*. VCH: New York, 1993.
13. Field, L. D.; George, A. V.; Hambley, T. W., *Inorg. Chem.* **1990**, *29*, 4565-4569.
14. Field, L. D.; George, A. V.; Laschi, F.; Malouf, E. Y.; Zanello, P., *J. Organomet. Chem.* **1992**, *435*, 347-356.
15. Field, L. D.; George, A. V.; Malouf, E. Y.; Slip, I. H. M.; Hambley, T. W., *Organometallics* **1991**, *10*, 3842-3848.
16. Field, L. D.; Turnbull, A. J.; Turner, P., *J. Am. Chem. Soc.* **2002**, *124*, 3692-3702.
17. Bill, E. julX; Version 1.41; Max Planck Institute for Bioinorganic Chemistry, Mullheim an der Ruhr. http://ewww.mpi-muelheim.mpg.de/bac/logins/bill/julX_en.php; 2008.

APPENDIX 1: SUPPORTING INFORMATION FOR ANCILLARY-LIGAND HYDROGEN-BONDING EFFECTS ON ANION-DEPENDENT SPIN-STATE SWITCHING IN HETEROLEPTIC FE(II) COMPLEXES

A1.1 pimH and pimMe details

Synthesis

[(H₂bip)₂Fe(pimH)]Br₂ (A2.I·Br). 121 mg of 2-(2′-pyridinyl)imidazole (pimH, 0.83 mmol) was combined with 457 mg of [Fe(H₂bip)₂Br₂], affording 543 mg of product (94 %). IR (KBr): ν_{N-H} 3237, 3125 cm⁻¹. ¹H NMR (CD₂Cl₂) δ 74.0 (aryl), 66.7 (NH), 56.0 (NH), 48.1, 45.1, 40.1, 36.3 (aryl), 30.0 (aryl), 26.4 (aryl), 25.4, 22.7, 18.0, 15.8 (aryl), 14.4, 7.2, −10.8 ppm. Absorption spectrum (CH₂Cl₂): λ_{max} (ε_M) 501 nm (3050 L·mol⁻¹·cm⁻¹). μ_{eff} (300 K): 3.87 μ_B. Anal. Calcd for C₂₄H₃₅N₁₁Br₂Fe: C, 41.58; H, 5.09; N, 22.22. Found: C, 41.27; H, 4.83; N, 21.93.

**[(H₂bip)₂Fe(pimH)](BPh₄)₂ (A2.I·BPh₄)**. 239 mg of **A2I·Br** (0.34 mmol) was combined with 472 mg of NaBPh₄, affording 270 mg of product (67 %). IR (KBr): ν_{N-H} 3398, 3331 cm⁻¹. ¹H NMR (CD₂Cl₂) δ 117.4 (aryl), 85.3 (NH), 81.5 (NH) 50.7 (aryl), 42.2 (aryl), 32.3 (aryl), 23.7, 22.5, 19.3 (aryl), 18.2, 12.9, 9.5 (BPh₄), 8.5 (BPh₄), 8.0 ppm (BPh₄). Absorption spectrum (CH₂Cl₂): λ_{max} (ε_M) 498 nm (2110 L·mol⁻¹·cm⁻¹). μ_{eff} (300 K): 5.28 μ_B. Anal. Calcd for C₇₂H₇₅N₁₁B₂Fe: C, 73.79; H, 6.45; N, 13.15. Found: C, 73.52; H, 6.19; N, 13.31. Crystals of [Fe(H₂bip)₂.₄(pimH)₀.₆](BPh₄)₄·~0.35CH₂Cl₂ (**A2.I+more**) were grown by slow diffusion (over 10 days) of diethyl ether into a dichloromethane solution of **A2I·BPh₄**.

A1.2 Solution Stability Details of 2.1·X and 2.2·X

An ether diffusion into a solution of **2.1·BPh₄** in dichloromethane yielded no initial solid product. After standing for more than two weeks, 2-3 crystals were observed. The crystal structure revealed Fe(H₂bip)₃(BPh₄)₂ as a result of ligand scrambling in solution. Moreover, a study of pimH complexes yielded crystals with the formula [Fe(H₂bip)$_{2.7}$(pimH)$_{0.3}$](BPh₄)₂.
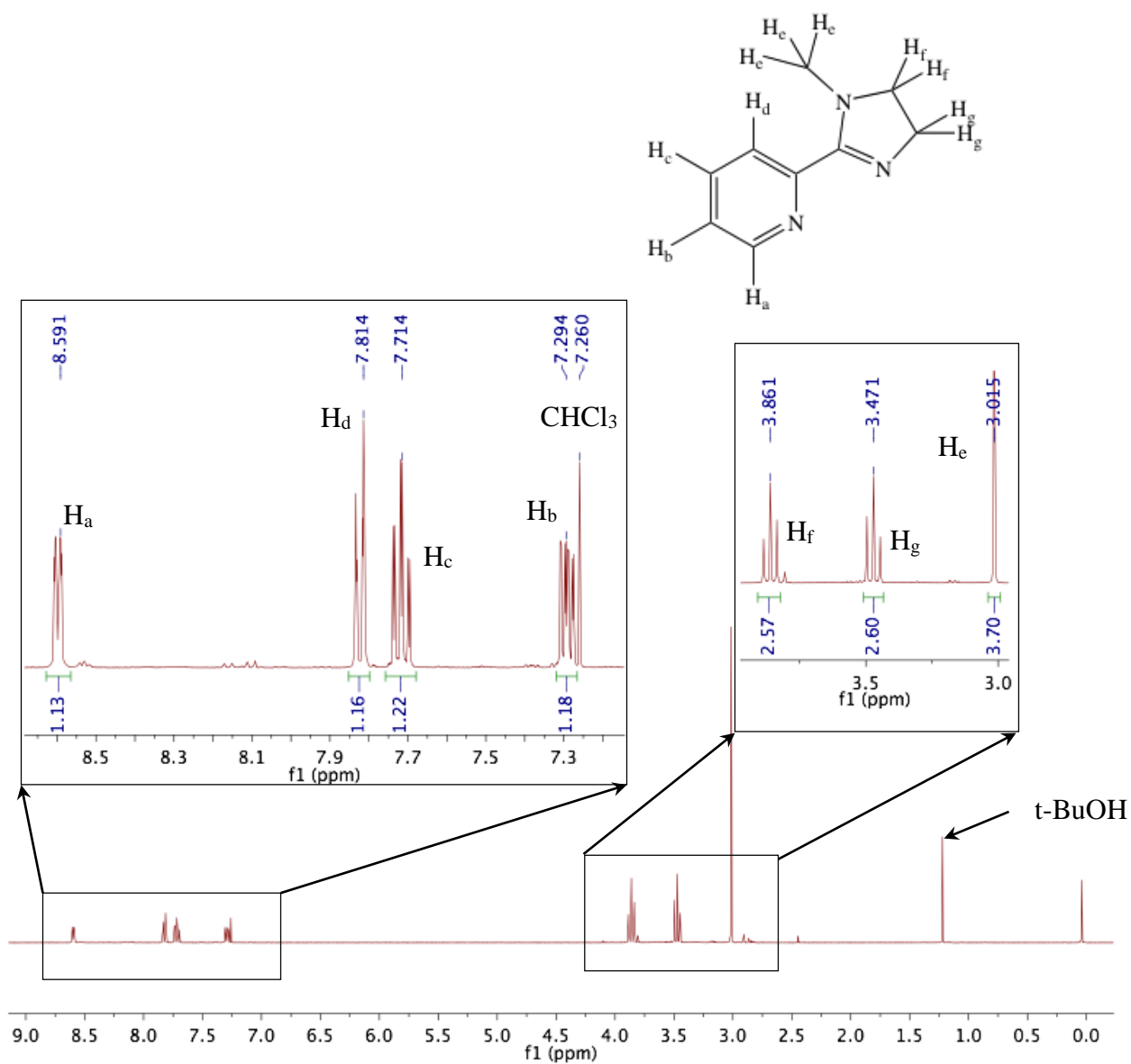
Figure A1.1. ¹H NMR spectrum of pizMe in CDCl₃.
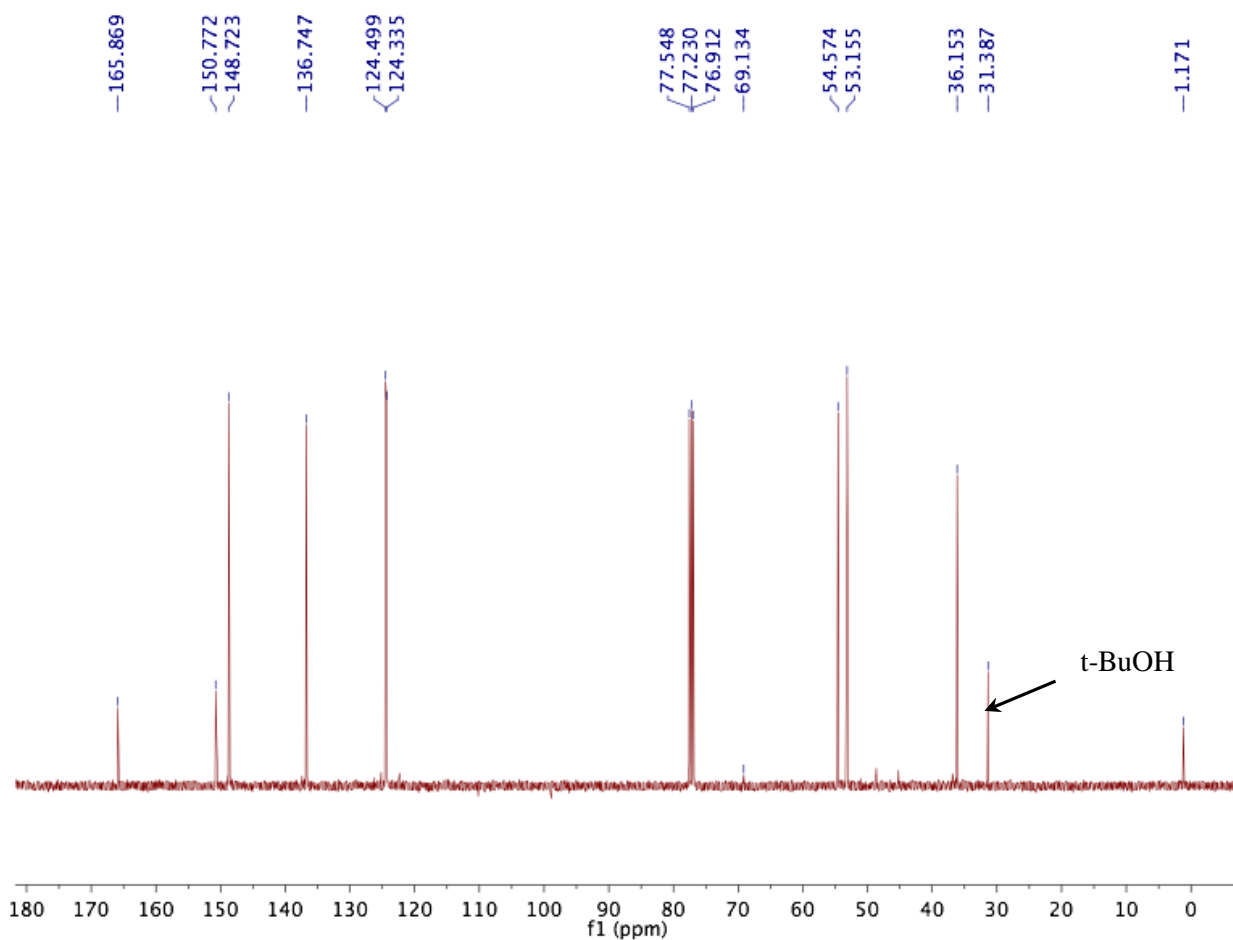
Figure A1.2. ^{13}C NMR spectrum of pizMe in CDCl$_3$.

APPENDIX 2: SUPPORTING INFORMATION FOR CHAPTER 6: EFFORTS TO CONTROL

MAGNETIC COUPLING AND ANISOTROPY IN FE(III) MULTINUCLEAR COMPLEXES

THROUGH LIGAND DESIGN

**A2.1 Additional {Fe(dmpe)$_2$}-containing complexes**

When attempting to crystallize **6.4·(OTf)$_3$**, [Fe(dmpe)$_2$(CH$_3$CN)Cl](OTf) was obtained as yellow needles. When attempting to obtain [Fe(dmpe)$_2$(Cl)(CCSi(CH$_3$)$_3$)]PF$_6$ for subtraction methods, [Fe(dmpe)$_2$(CCH)Cl](PF$_6$)$_2$ was obtained. The structure is of low quality and is not reported, however the unit cell is included in Table A2.1 for future comparison. The deprotected acetylide complex may also be interesting for subtraction methods, however it could not be prepared consistently. It appears to be a random product of ligand dissociation in solution, whereas the solvate complex, Fe(dmpe)$_2$(CH$_3$CN)Cl](OTf), is obtained from impurities that remain from the synthesis of **6.4**. Green crystals of **6.4·(OTf)$_3$** that are re-crystallized from a diffusion of ether into acetonitrile do not show this impurity and therefore appear to be relatively stable in solution.

X-Ray Structure Determinations. Structures were determined for the compounds listed in Table 6.1. All single crystals were coated in Paratone oil prior to removal from the glovebox. The crystals were supported on Cryoloops before being mounted on a Bruker Kappa Apex 2 CCD diffractometer under a stream of cold dinitrogen. Data were collected with Mo Kα radiation and a graphite monochromator. Initial lattice parameters were determined from reflections harvested from 36 frames, and data sets were collected targeting complete coverage and 4-fold redundancy. Data were integrated and corrected for absorption effects with the Apex 2 software package.[10] Structures were solved by direct methods and refined with the SHELXTL software package.[11] Unless otherwise noted, thermal parameters for all fully occupied, non-hydrogen atoms were refined anisotropically. Hydrogen atoms were added at the ideal positions and were refined using

a riding model where the thermal parameters were set at 1.2 times those of the attached carbon atom (1.5 times that for methyl protons).

The structure of **6.3·(OTf)₂** shows one triflate with significant disorder. Attempts to model the disorder suggest two positions for the anion in a partially overlapped end-to-end arrangement. Residual electron density indicates the SO_3 and CF_3 groups on each likely have rotational disorder as well. Attempts to model disordered components of the partial occupancy atoms were not performed. As a result, the anion is not modeled well, and atoms have unrealistic thermal parameters.
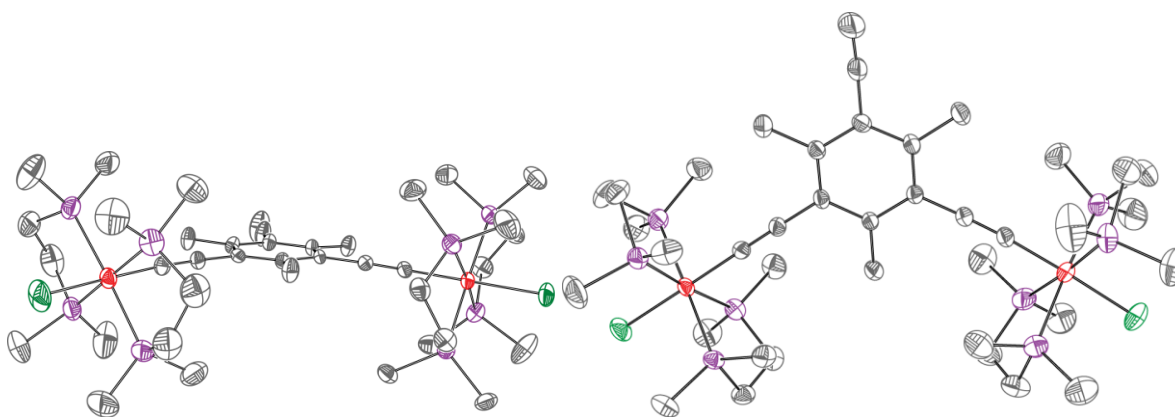
Figure A2.1. Left, the side-on view of the crystal structure of **6.3·(OTf)₂** illustrating the {Fe(dmpe)₂} moiety orientation and right, the dinuclear arrangement of **6.3·(OTf)₂**. Carbon, chlorine, iron and phosphorus are rendered as grey, green, red and purple ellipsoids, respectively. Hydrogen atoms are omitted for clarity. Ellipsoids are drawn at the 40% probability level.
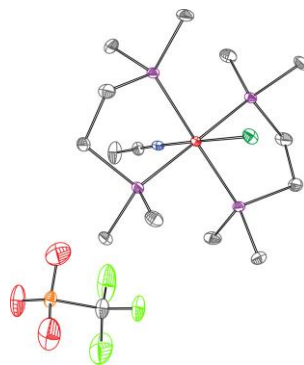
Figure A2.2. Crystal structure of [Fe(dmpe)$_2$(CH$_3$CN)Cl](OTf). Carbon, chlorine, iron, phosphorus, nitrogen, fluorine, sulfur, and oxygen are rendered as grey, green, red, purple, blue, light green, organge, and red ellipsoids, respectively. Hydrogen atoms are omitted for clarity. Ellipsoids are drawn at the 40% probability level.

Table A2.1. Crystallographic data[a] for [Fe(dmpe)$_2$(Cl)(CCSi(CH$_3$)$_3$)](PF$_6$), [Fe(dmpe)$_2$(CH$_3$CN)Cl](OTf) and **6.3·(OTf)$_2$**.

	[Fe(dmpe)$_2$(Cl)-(CCSi(CH$_3$)$_3$)](PF$_6$)	[Fe(dmpe)$_2$(CH$_3$CN)Cl] (OTf)	**6.3·(OTf)$_2$**
formula	C$_{14}$H$_{33}$ClF$_6$FeP$_5$	C$_{15}$H$_{35}$ClF$_3$FeNO$_3$P$_4$S	C$_{41}$H$_{74}$Cl$_2$F$_6$Fe$_2$O$_6$P$_8$S$_2$
fw		581.68	1271.48
color, habit	yellow needles	yellow needles	green plates
T, K	120(2) K	120(2) (K)	120(2) K
space group	$C2/c$	$P2_1/c$	Pbcn
Z	8.0	4.0	8.0
a, Å	22.6846(11)	9.0194(6)	31.345(5)
b, Å	18.3058(10)	16.9688(11)	14.201(2)
c, Å	15.8261(9)	16.3785(9)	26.815(4)
α, deg	90.0000	90.0000	90.000
β, deg	134.081(4)	90.893(3)	90.000
γ, deg	90.0000	90.0000	90.000
V, Å^3	4721.0(5)	2506.4(3)	11937(3)
d_{calc}, g/cm^3		1.541	1.415
GooF		1.057	1.022
$R_1(wR_2)^b$, %		4.04 (9.01)	5.05 (13.20)

[a] Obtained with graphite-monochromated Mo Kα (λ = 0.71073 Å) radiation.
[b] $R_1 = \text{å}||F_o| - |F_c||/\text{å}|F_o|$, w$R_2 = \{\text{å}[w(F_o{}^2 - F_c{}^2)^2]/\text{å}[w(F_o{}^2)^2]\}^{1/2}$ for $F_o > 4\sigma(F_o)$.